UNIVERSITY OF ÇUKUROVA
INSTITUTE OF NATURAL AND APPLIED SCIENCE

MSc THESIS

Mehmet Melih TATLISÖZ

INVESTIGATION OF THE PERFORMANCE OF A PULSATILE FLOW MICROMIXER COUPLED WITH ICEO

DEPARTMENT OF BIOMEDICAL ENGINEERING

ADANA-2018

ÇUKUROVA UNIVERSITY
INSTITUTE OF NATURAL AND APPLIED SCIENCES

INVESTIGATION OF THE PERFORMANCE OF A PULSATILE FLOW MICROMIXER COUPLED WITH ICEO

Mehmet Melih TATLISÖZ

MSc THESIS

DEPARTMENT OF BIOMEDICAL ENGINEERING

We certify that the thesis titled above was reviewed and approved for the award of degree of the Master of Science by the board of jury on 27/08/2018.

…….....	……	…….....
Asst. Prof. Dr. Çetin CANPOLAT	Asst. Prof. Dr. Ahmet AYDIN	Asst. Prof. Dr. İlyas KARASU
SUPERVISOR	MEMBER	MEMBER

This MSc Thesis is performed in Department of Biomedical Engineering of Institute of Natural and Applied Sciences of Çukurova University.
Registration Number:

Prof. Dr. Mustafa GÖK
Director
Institute of Natural and Applied Sciences

ABSTRACT

MSc THESIS

INVESTIGATION OF THE PERFORMANCE OF A PULSATILE FLOW MICROMIXER COUPLED WITH ICEO

Mehmet Melih TATLISÖZ

ÇUKUROVA UNIVERSITY
INSTITUTE OF NATURAL AND APPLIED SCIENCES
DEPARTMENT OF BIOMEDICAL ENGINEERING

Supervisor : Asst. Prof. Dr. Çetin CANPOLAT
Year: 2018, Pages: 105
Jury : Asst. Prof. Dr. Çetin CANPOLAT
: Asst. Prof. Dr. Ahmet AYDIN
: Asst. Prof. Dr. İlyas KARASU

In this study, the characteristics of two miscible liquids are investigated under pulsatile flow conditions along a microchannel with certain obstruction width numerically. The types of fluid are defined as Newtonian, power-law, and Carreau. Although micromixing capability can be enhanced using pulsation and obstruction, induced-charge electro-osmosis (ICEO) is needed for acceptable mixing efficiencies at desired time and length. The ICEO electrode is defined on the top side of obstructtion. Mixing indexes are plotted concerning the magnitude of external potential difference, width and length of the obstruction and frequency of pulsatile flow. Streamlines and concentration maps are presented for various magnitude of external potentials. Mixing performances during the last period of pulsatile flow are plotted according to the width and length of ICEO electrode for each external potential difference, as well. The effects of pulsation frequency on average mixing indexes are demonstrated for various obstruction widths. It is observed that mixing performance is increased with the external potential difference due to strong ICEO vortices. However, this situation is not evident, when an obstruction is present. The extended length of ICEO electrode significantly diminishes time-dependent variations in mixing indexes. Mixing index is increased using pulsation frequency until the frequency of f=1Hz and then decreased. When the obstruction width increases, higher mixing indexes are obtained for smaller frequency values compared to f=1Hz. As a result, mixing indexes of 99% and 94% are successfully obtained using correct parameter combinations for Newtonian and non-Newtonian fluids, respectively.

Keywords: Micromixing**,** pulsatile flow, induce-charge electro-osmosis, microobstruction

ÖZ

YÜKSEK LİSANS TEZİ

ICEO İLE BİRLEŞTİRİLMİŞ SALINIM AKIŞLI BİR MİKROMİKSERİN PERFORMANSININ İNCELENMESİ

Mehmet Melih TATLISÖZ

ÇUKUROVA ÜNİVERSİTESİ
FEN BİLİMLERİ ENSTİTÜSÜ
BİYOMEDİKAL MÜHENDİSLİĞİ ANABİLİM DALI

Danışman : Dr. Öğr. Üyesi Çetin CANPOLAT
Yıl: 2018, Sayfa: 105
Jüri : Dr. Öğr. Üyesi Çetin CANPOLAT
: Dr. Öğr. Üyesi Ahmet AYDIN
: Dr. Öğr. Üyesi İlyas KARASU

Bu çalışmada, iki karıştırılabilen sıvı engelli mikrokanal boyunca salınımlı akış koşulları altında nümerik olarak incelenmiştir. Akışkan tipleri Newton tipi, power-law ve Carreau olarak tanımlanmıştır. Salınımlı akış ve mikroengeller ile karıştırma performansı arttırılabilmesine rağmen, istenilen uzunluk ve zamanda kabul edilebilir bir karışma verimi için indüklenmiş yük elektroosmosuna (Induced-Charge Electroosmosis – ICEO) ihtiyaç duyulmuştur. ICEO elektrotu, dikdörtgen kesitli mikroengelin üst yüzeyine tanımlanmıştır. Karışma indeksleri harici potansiyel fark büyüklüğü, mikroengel genişliği ve yüksekliği ile salınımlı akış frekansına bağlı olarak incelenmiştir. Akış çizgileri, çözünen türlerin dağılımı potansiyel farklara göre çizdirilmiştir. Son periyotta karışma performansları her potansiyel fark için ICEO elektrotunun genişliği ve yüksekliğine göre incelenmiştir. Salınım frekansı birkaç mikroengel genişliğinde ortalama karışma indeksi için gösterilmiştir. Kuvvetli ICEO girdaplarından ötürü harici potansiyel fark ile karışma veriminin arttığı gözlemlenmiştir. Fakat bu durum mikroengellerin varlığı ile geçerli değildir. Karışma indekslerinde dalga-lanmalar uzun ICEO elektrotu ile önemli ölçüde azaltılmıştır. Karışma indeksi 1Hz değerine dek artmış, sonrasında azalmıştır. Fakat mikroengel varlığında f=1Hz'e göre düşük frekans değerlerinde daha yüksek karışma indeksi elde edilmiştir. Sonuç olarak, doğru parametrelerin kullanımı ile Newton tipi ve Newton tipi olmayan akışkanlar için sırasıyla %99 ve %94 karışma indeksi başarı ile elde edilmiştir.

Anahtar Kelimeler: Mikrokarıştırma**,** salınımlı akış, indüklenmiş yük elektroosmosu, mikroengel

GENİŞLETİLMİŞ ÖZET

Bu çalışmada, iki farklı akışkan mikrokanallar içerisinde karıştırılmıştır. Karışma öncelikle yalnızca salınımlı akış altında gerçekleştirilmiştir. Doğası gereği sürekli hız büyüklüğü ve yön değişimi barındırmasından dolayı, salınımlı akış, karışma verimini arttırabilmektedir. Fakat tek başına salınımlı akış ile kabul edilebilir seviyenin çok altında bir karışma verimi elde edilebilmiştir. Bundan dolayı, mikrokanal içine bir adet mikroengel yerleştirilmiştir. Mikroengel kanal genişliğini azaltarak karışmaya katkı sağlayabilmektedir. Yine de yalnızca salınımlı akış ile elde edilen karışma verimi çok düşük bir miktarda arttırılabilmiştir. Sonuçta, tasarım için akım çizgileri arasında ileri seviyede düzensizlik yaratacak ayrı bir bileşene ihtiyaç duyulmuştur. Bu da spesifik bir elektrokinetik olay ile, yani indüklenmiş yük elektroosmozu (ICEO – Induced Charge Electroosmosis) ile sağlanmıştır. ICEO olayının klasik elektroosmozdan (EO) farkı ilgili kutuplanabilir malzeme üzerinde yükün harici bir elektriksel alan ile *indüklenmesidir*. Buna göre, bir elektrolit çözeltisine daldırılmış ve dış elektrik akımına maruz bırakılmış iletken malzemenin bir yarısında pozitif yükler indüklenirken diğer yarısında negatif yükler indüklenir. Sonuçta, ICEO akım çizgisi boyunca eş girdaplar üretilir ve yüksek bir karışma veriminin önü açılır. Akışkan akışına, ayrıca, harici elektriksel alan da elektroosmozun oluşumu ile katkı sağlar. Sonuçta, kanal boyunca akış hızı salınımlı hız, basınç farkı ile oluşan hız ve elektroosmotik hızın süperpozisyonu ile elde edilir.

Bu çalışmanın amacı, ICEO ile birleştirilmiş salınımlı akış koşulları altında mikrokarıştırıcı verimlerini sistematik olarak incelemektir. Optimum mikro-karıştırıcı parametreleri, karışma verimi akışkanlar içinde çözünen kimyasal türlerin kanal çıkışındaki konsantrasyon değerleri temel alınarak belirlenmiştir. Tasarlanan mikrokanal L=1mm uzunluğunda ve sol sınırı giriş, sağ sınırı çıkış olarak belirlenmiştir. Akış, Navier – Stokes ve süreklilik denklemleri ile modellenmiştir. Akışkanın doğası Newton tipi ve sıkıştırılamaz olarak belirlendiği

için bu denklemler üzerinde gerekli sadeleştirmeler yapılmıştır. Çözünen türlerin taşınımı, Nernst – Planck denklemi ile modellenmiştir. Nernst – Planck denklemi türlerin konveksiyon ve difüzyon akılarını barındırırken, kimyasal reaksiyon terimi ihmal edilmiştir. Öte yandan, sadece salınımlı akış ile çıkışa yeterli miktarda çözünmüş türün taşınamadığı da saptanmıştır. Bunun için salınımlı akışın dalgalı hız değerlerine kararlı bir hız değeri eklenmiştir.

Harici potansiyel fark değerlerini belirlemek için mikrokanal boyunca çeşitli gerilimler, V=10V – 20V – 30V – 35V – 40V – 45V – 50V, denenmiştir. Maksimum salınımlı hız değeri ve Poiseuille akışı ile elektroosmotik akışın toplamından oluşan daimi hız değeri arasındaki oran dikkate alınarak seçim yapılmıştır. Bu oranın düşük seçilmesi çözünmüş tür taşınımını engellerken, yüksek seçilmesi salınımlı akışı baskılamaktadır. Buna göre V=20V, 30V ve 40V simülasyonlar için harici potansiyel fark değerleri olarak seçilmiştir.

En yüksek karışma indeksine ulaşmak adına harici elektriksel potansiyel fark değerinin büyüklüğü, mikroengelin, dolayısıyla ICEO elektrotunun, genişliği ve yüksekliği ile salınımlı akışın frekansı sistematik olarak değiştirilmiştir.

Düz kanalda artan harici potansiyel fark ile karışma indeksinin de arttığı gözlemlenmiştir. Bu durum daha yüksek ICEO hızı, dolayısıyla da daha yüksek vortisite ile açıklanabilir. Ayrıca, en yüksek harici potansiyel fark için periyot boyunca karışma indeksinin değişimi belirgin ölçüde daha kararlıdır. Mikrokanala mikroengel eklendiğinde ise harici potansiyel fark ve karışma indeksinin artık doğru orantılı olmadığı tespit edilmiştir. Mikroengellerin genişliği ardışık simülasyonlar için W_c=0.01mm olarak arttırılmıştır. En düşük mikroengel genişliği için (W_c=0.01mm), karışma indeksi yükselse de takip eden genişlik değerleri (W_c=0.02mm ve 0.03mm) için azalmıştır. Bu geometrik konfigürasyonlar için düşük harici potansiyel farklarda yüksek karışma indeksi elde edilmiştir. Kanal boyunca artan blokaj, çözünen türlerin taşınmasını önleyerek, karışma indeksinin düşmesine sebep olmuştur. Kanal boyunca artan basınç düşümü türlerin taşınımını kolaylaştırmıştır. mikroengel genişliği W_c=0.05mm için karışma indeksi

W_c=0.04mm değerine göre daha düşüktür. Bu da kanal blokajının aşırı artması ile açıklanabilir.

Bir periyot süresince karışma indeksinin değerindeki değişimlerin miktarı, akış hızına önemli ölçüde bağlıdır. Aynı mikrokanal geometrisi yüksek harici potansiyel fark değerlerinde daha stabil karışma indeksleri gözlemlenmiştir. Bununla birlikte, daha yüksek ICEO hızına sebebiyet veren uzun elektrot ile de periyot süresince stabil karışma indeksleri hesaplanmıştır. Uzun elektrotun kısa elektrota göre bir diğer farklılığı ise düşük potansiyel farklar için daha yüksek bir karışma indeksinin elde edilmesidir. Bununla birlikte, uzun elektrot ile artan potansiyel fark değerlerine göre karışma indeksinin düştüğü kritik gerilim V=35V olarak tespit edilirken, kısa elektrot için bu durum V=30V değerine karşılık gelmektedir.

Vortisite değeri yukarıda ifade edildiği gibi harici potansiyel fark ile arttırılabilmektedir. Bununla birlikte, ICEO elektrotu üzerinde indüklenen yük miktarı da elektrotun boyutu ile doğru orantılıdır. Dolayısıyla, büyük boyutlu elektrotlar ile daha yüksek vortisite değerlerine ulaşılmıştır.

Karışma indeksinin Strouhal sayısına önemli ölçüde bağlı olduğu simülasyonlar esnasında açıkça gözlemlenmiştir. Bu bağlılığın birincil sebebi çözünen türlerin çıkışa taşınma miktarıdır. Simülasyonların tamamı başlangıçta f=1Hz ile yürütülmüş, devamında f=0.5Hz, 1.5Hz ve 2Hz ile salınımlı akışın uygulanma süresi sabit tutularak çözümlemeler yapılmıştır. Düz kanal için karışma indeksi f=1Hz'lik frekans değerine kadar artan bir eğri çizmiştir. Takip eden frekans değerleri boyunca da sürekli azalmıştır. Yüksek frekanslarda çözünen türlerin taşınımı için sahip olunan süre daha az olduğu görülmüş ve çıkış sınırındaki konsantrasyon değerleri önemli ölçüde azalmıştır. Bu azalma, f=2Hz değerinde kabul edilebilir seviyenin de altına indiği için daha yüksek frekanslarda simülasyon yapılmamıştır. Mikrokanala mikroengel eklendiğinde ise düz kanala göre biraz farklı bir sonuç alınmıştır. Karışma indeksi, f=1Hz değerinin ardından

benzer biçimde azalırken, f=0.5Hz için daha yüksek bir karışma indeksi elde edilmiştir.

Sonuçta, Newton tipi akışkan için, L_c=0.1mm mikroengel uzunluğu, W_c=0.01mm mikroengel yüksekliği, V=40V harici potansiyel fark ve f=1Hz salınımlı akış frekansı mikrokarıştırıcı için optimum parametreler olarak belirlenmiştir. Bu parametreler ile %99 oranında karışma indeksine ulaşılabilmiştir.

Newton tipi akışkan ile simülasyonlar sona erdikten sonra Newton tipi olmayan akışkanlar ile analizlere devam edilmiştir. Aynı parametreler, aynı akış ve kanal geometrisi koşulları altında incelenmiş ve sonuçlar Newton tipi akışkan sonuçları ile karşılaştırılmıştır. Simülasyonlara V=40V harici potansiyel fark ve f=1Hz salınımlı akış frekansı ile başlanmıştır. Power-law ve Carreau modelleri ile akışkanlar sisteme tanıtılmıştır. Model parametreleri, literatürdeki referanslara dayanarak, kan olarak belirlenmiştir. Power-law ve Carreau modellerinden alınan sonuçlar arasındaki farkın çok az olmasından dolayı, bu çalışmada verilen parametreler ile kan akışının her iki modelle de çözümlenebileceği ispatlanmıştır. Çünkü bu akışkan modellerindeki parametreler kan akışı için literatürden özel olarak seçilmiştir.

Newton tipi olmayan akışkanlar ile elde edilen girdaplar, Newton tipi akışkan ile elde edilenlere göre her mikroengel yüksekliği için daha zayıftır. Bundan dolayı düz kanalda Newton tipi akışkan ile elde edilen karışma indeksi Newton tipi olmayana nazaran daha yüksektir. Fakat mikroengel genişliği 0.03mm değerine yükseltildiğinde Newton tipi olmayan akışkanlar için de mikrokanal çıkışında üniform bir konsantrasyon profili elde edilmiştir. Newton tipi akışkan için ise çıkıştaki konsantrasyon ortalama değerin altına inmiştir.

Newton tipi akışkanda elde edilen girdapların daha kuvvetli olmasından dolayı düz kanalda ve mikroengel genişliği W_c=0.01mm durumunda Newton tipi akışkan ile son periyot boyunca elde edilen karışma indeksi Newton tipi olmayan akışkanlara göre daha yüksektir. Fakat mikroengel genişliği W_c=0.02mm değerine arttırıldığında Newton tipi akışkan için karışma indeksi düşerken, Newton tipi

olmayan akışkanlar için yükselmiştir ve sonuçta Newton tipi olmayan akışkanlar için daha yüksek karışma indeksi elde edilmiştir. Bu eğilim, mikroengel genişliği W_c=0.03mm değerine yükseldiğinde de sürdürülmüştür. Bu durum, kuvvetli girdapların çözünen türlerin taşınımına engel olması ile açıklanabilir.

Değişik harici potansiyel fark değerleri de (V=20V ve 30V) sisteme uygulanmıştır. Elde edilen sonuçlar bir periyot boyunca ortalama karışma indeksi olarak farklı mikroengel değerlerine karşılık ayrı ayrı değerlendirilmiştir. Düz kanalda V=20V için, Newton tipi akışkan ile Newton tipi olmayan akışkanlardan elde edilen ortalama karışma indeksi değerleri arasındaki fark çok yüksekken, artan mikroengel değerleri ile bu fark azalmıştır. Hatta en yüksek mikroengel değeri için (W_c=0.03mm) Newton tipi akışkan ile elde edilen ortalama karışma indeksi değeri, Newton tipi olmayan akışkan tarafından aşılmıştır. Düz kanalda V=30V ve W_c=0.01mm mikroengelli geometri için yeniden Newton tipi akışkan ile elde edilen ortalama karışma indeksi değeri Newton tipi olmayan akışkanlara göre yüksektir. Fakat aralarındaki fark, önceki duruma göre daha azdır. Nitekim, Newton tipi olmayan akışkanlar için ortalama karışma indeksi değeri W_c=0.02mm mikroengel genişliğinde Newton tipi akışkanı aşmıştır. Bu fark Wc=0.03mm değerinde ise daha da artmıştır. Bunda, yüksek mikroengel genişliklerinde (W_c=0.02mm ve 0.03mm) Newton tipi akışkanın ortalama karışma indeksi düşerken, Newton tipi olmayan akışkanların yükselmesi önemli ölçüde etkilidir. Ayrıca, V=40V için de V=30V durumundaki ortalama karışma indeksine benzer bir kalıp elde edilmiştir. Newton tipi akışkan ile elde edilen ortalama karışma indekslerinin yüksek voltajlarda ve yüksek mikro-engel genişliklerinde düşmesi, çözünen türlerin taşınımındaki azalma ile açıklanabilir.

Salınımlı akış frekansı karışma indeksine ciddi ölçüde etki eden bir parametredir. Salınımlı akış frekansına göre karışma indeksindeki değişim bütün mikroengel genişliklerine göre ifade edilmiştir. Düz kanal ve W_c=0.01mm mikroengel genişliği için bütün akışkanlarda farklı frekans değerlerine göre benzer eğriler elde edilmiştir. En yüksek karışma indeksi f=1Hz frekans değeri için elde

edilirken, en düşük karışma indeksi f=2Hz frekansı için gözlemlenmiştir. Newton tipi akışkan ile elde edilen karışma indeksi, Newton tipi olmayan akışkanlara göre daha yüksektir. Tanımlanan eğri, Newton tipi olmayan akışkanlar için W_c=0.02mm ve W_c=0.03mm mikroengel genişliklerinde de geçerlidir. Fakat Newton tipi olmayan akışkan için f=0.5Hz frekans değerinde daha yüksek karışma indeksi elde edilmiştir. Karışma indeksi f=1.5Hz ve f=2Hz frekanslarında yine düşmüştür. Ortalama karışma indeksi f=1Hz frekansı için Newton tipi akışkan için Newton tipi olmayan akışkanların ortalama karışma indeksi tarafından aşılmıştır. Ortalama karışma indeksi W_c=0.03mm mikroengel genişliği için, hem f=1Hz hem f=1.5Hz frekans değerlerinde Newton tipi akışkan için Newton tipi olmayan akışkanın ortalama karışma indeksi tarafından aşılmıştır.

Bu çalışma çözünen türlerin karışmasına reaksiyon eklenerek genişletilebilir. Bu sayede antikor-antijen bağlanması, protein-ligand reaksiyonu gibi her türlü biyokimyasal etkileşimler incelenebilir.

ACKNOWLEDGEMENT

I want to send my biggest thanks to my supervisor, Assist. Prof. Dr. Çetin CANPOLAT. He has directed and taken care of me sensitively during the preparation of this thesis.

I also thank to Assist. Prof. Dr. Ahmet AYDIN and Assist. Prof. Dr. İlyas KARASU with my kindest regards for sharing his valuable knowledge with me.

My parents were always stood by me during my thesis studies. They deserve a limitless thanking for their moral support.

Çukurova University Scientific Research Office financially supported this research under contract no FBA-2017-7960. Their contributions are greatly appreciated.

CONTENTS **PAGE**

LIST OF TABLES **PAGE**

LIST OF FIGURES **PAGE**

LIST OF ABBREVIATIONS AND NOMENCLATURE

2D	:	2 Dimensional
3D	:	3 Dimensional
AC	:	Alternating Current
DC	:	Direct Current
DEP	:	Dielectrophoresis
EDL	:	Electrical Double Layer
EO	:	Electroosmosis
EP	:	Electrophoresis
ICEO	:	Induced-Charge Electroosmosis
LOC	:	Lab-on-a-Chip
PB	:	Poisson-Boltzmann
PNP	:	Poisson-Nernst-Planck
Re	:	Reynolds Number
RMS:	:	Root-mean-square
Pe	:	Péclet Number
St	:	Strouhal Number
TAS	:	Total Analysis System
μTAS	:	Micro Total Analysis System
C	:	Concentration
C_0	:	Initial concentration
C_D	:	Diffuse layer capacitance
D	:	Diffusion coefficient
E	:	Electrical Field
e	:	Elementary charge
f	:	Body force
f	:	Pulsation frequency
k_B	:	Boltzmann constant

L	:	Characteristic length scale
m	:	Flow consistency index
n	:	Flow behavior index
p	:	Pressure
R	:	Reaction term
T	:	Temperature
t	:	Time
$\mathbf{u}$	:	Fluid velocity
U_m	:	Maximum pulsatile velocity
U_s	:	Laminar flow velocity
Van	:	External potential difference
z	:	Valence ion number
$\dot{\gamma}$	:	Shear rate
ε	:	Permittivity of the fluid
ε_0	:	Permittivity of the free space
ε_r	:	Relative permittivity of the fluid
ζ_i	:	Induced zeta potential
ζ_w	:	Zeta potential of the channel walls
λ	:	Characteristic relaxation time
ρ	:	Density of the fluid
ρ_e	:	Net space charge density
ρ_s	:	Net surface charge density
σ	:	Conductivity

1. INTRODUCTION

1.1. Microfluidics

Performing rapid and accurate analysis is a critical issue for the scientists and clinicians in micron scale, in which total analysis system (TAS) was proposed as a solution by Kopp et al. (1997). It is proved that TAS is capable of performing a laboratory analysis for applications of mixing, separation, detection, and isolation; however, significant disadvantages still exist, such as long duration for the analysis, necessity of high sample/reagent amount and low separation efficiency (Rios et al., 2012). Following the general trend of miniaturizing, micro total analysis system (μTAS) was reported by Manz et al. (1990), which was successfully adapted into different fields of the research and expressed with a general term as Lab-on-a-Chip (LOC) (Rios et al., 2012). As a result of miniaturization, LOC has the advantages of portability, low fabrication cost, low analysis time, high separation efficiency, low mixing/reagent consumption and high sensitivity (Trietsch et al., 2011), and thus, the drawbacks of TAS are overcome with the aid of LOC.

Many disciplines; such as physics, chemistry, electronics, and micro-engineering are included in the field of LOC. Integrated structure is imposed to the LOC with the components of injector, preparator, transporter, mixer, reactor, separator, detector, controller and power supply (Lim et al., 2010). Therefore, development in this field is directed mainly by the study of fluid flow naming as microfluidics (Jain et al., 2009). Microfluidics is defined as manipulating and processing the fluid in microchannels, which has at least one dimension smaller than a millimeter (Martinez et al., 2010, Stone et al., 2004). A sample for a microfluidic device is shown in Figure 1.1 for the study of Godin et al. (2006)

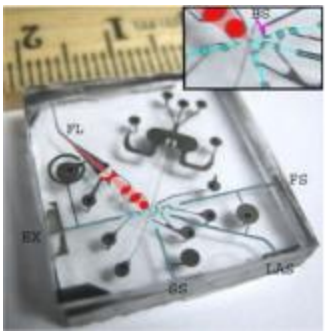

Figure 1.1. Microfluidics system with various components as an example (Godin et al., 2006)

To the best of our knowledge, the microfluidic chip was introduced to open literature in 1994 and attracted significant attention after 2005 with a slow evolution pace, which can be seen in Fig 1.2 (Fung, 2016). The research topics in microfluidics can be classified as capillary, pressure-driven, centrifugal, electrokinetic and acoustic using platforms for driving the liquid, which is schematized in Figure 1.3 (Mark et al., 2009). Here, some specific application areas within this discipline: Laser processing (Malek, 2016), micro reaction engineering (Jensen, 1999), printing (Bhattacharjee et al., 2016) and optics (Psaltis et al., 2006). In biomedical engineering perspective, some specific applications are biomolecule detection (Diercks et al., 2009), pathogen detection (Wang et al., 2009), separation of DNA particles (Krishnan et al., 2008), generating bone microtissues (Shimizu et al., 2015) and gene mutation detection (Li et al., 2010).

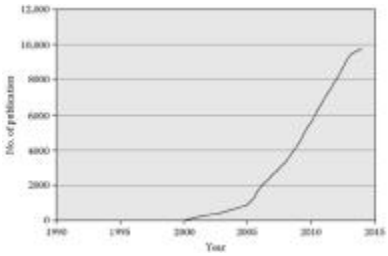

Figure 1.2. Published scientific papers related to the microfluidic chip during the years of 1994 - 2014 (Fung et al., 2016)

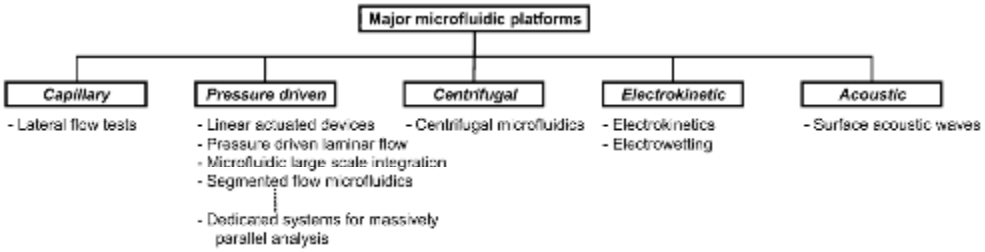

Figure 1.3. Major microfluidics platforms which are classified according to the fluid driving mechanism (Mark et al., 2009)

1.2. Newtonian and Non-Newtonian Fluids

Deformation rate exhibits linear proportionality with respect to shear rate for Newtonian fluids, which are primarily stated by Sir Isaac Newton (Çengel and Cimbala, 2006). Therefore, the viscosity of the fluid, which is the ratio between shear stress and deformation rate remains constant for each value of shear rate. Water, air, and oil are some typical examples of Newtonian fluids. On the other hand, the relationship between the rate of deformation and fluid shear exhibit non-linear behavior for non-Newtonian fluids which are mainly branched into three different categories according to variation in viscosity values under different magnitudes of shear rate. Since lower viscosity values are observed for higher shear rates in shear-thinning fluids, (or pseudoplastic), viscosity values are incremented for higher shear rates in shear-thickening fluids (or dilatant) (Zhao et al., 2008). Another type of non-Newtonian fluids is Bingham plastic, which includes threshold stress level for starting the fluid flow (Rubenstein et al., 2012). The most of the biofluids such as blood, saliva, urine possess non-Newtonian nature as well as shear-thinning behavior. The plot showing shear stress-deformation behavior of Newtonian and non-Newtonian fluids is demonstrated in Figure 1.4.

Characteristics of non-Newtonian fluids must be deeply understood for estimating the behavior of the microfluidics system (Tang et al., 2009). Power-law model (Chakraborty, 2007), Carreau model (Zimmermann et al., 2003), Powell-

Eyring model (Goswami et al., 2015) and Bingham model (Das et al., 2008) are some of the successfully utilized constitutive models for numerical non-Newtonian fluid analyses. In this study, the fluids are modeled as Newtonian, Power-law, and Carreau.

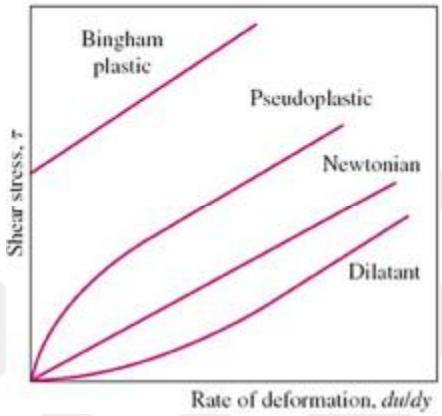

Figure 1.4. Shear stress curves against the rate of deformation for Newtonian and non-Newtonian fluids (Çengel and Cimbala, 2006)

1.3. Pulsatile Flow

Pressure difference is another tool for driving the fluid in our design. If the pressure gradient between inlet and outlet of a microchannel is not time-dependent, generally Poiseuille flow regime is observed. In contrast, the magnitude of pulsatile flow velocity has time-dependent nature. Pulsatile flow is initially introduced in 1930 (Tikekar et al., 2010). In some studies, such as Mao and Xu, (2009) and Fallenius et al., (2013), it is reported that pulsatile flow regime enhances micromixing performance. Parabolic laminar flow profile is observed in the pressure-driven systems, because of the no-slip condition on stationary walls of the channel (Figure 1.5). That is, the flow velocity is zero at the boundaries and reaches maxima at the centerline of the channel.

Micropumps with and without microvalves are employed for generating pressure differences. Microvalves are designed as a part of the micropumps and act

in controlling the fluid flow and/or species transport (Au et al., 2011). However, microvalves suffer from fatigue and switching control, which diminish the performance and reliability of the system (Nejat et al., 2014). Therefore, micropumps excluding microvalves are much more popular in engineering applications (Van De Pol, 1989). Nevertheless, a pressure difference is generated via mechanical parts, which may cause friction and heating as well as high costs. Similarly, pulsatile flow can be generated via dynamic controllers (Li and Kim, 2017). However, the designs excluding dynamic controllers are preferred for preserving simplicity.

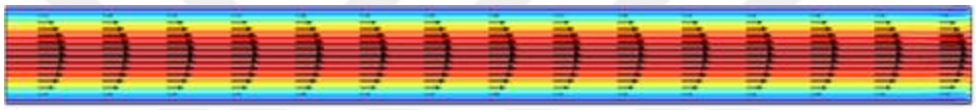

Figure 1.5 Parabolic flow profile

1.4. Electrokinetics

Electrokinetics is another topic in microfluidics, which utilizes electrical field to manipulate fluid and species transport (Kamali et al., 2016). In contrast to pressure-driven flow, fluid flow is driven without any mechanical part, which leads to popularity in the use of microfluidics applications, such as mixing (Shin et al., 2005), bioparticle detection (Wu et al., 2005), separation (Garcia et al., 2008), drug delivery (Chung et al., 2007), soil remediation (Zhou et al., 2004). Although issues of specificity and robustness are not fully resolved; sensitivity, portability, and efficiency are critical accomplishments for electrokinetic microdevices (Chang, 2006).

Three types of primary electrokinetic effects are commonly studied in the open literature, which are named as electroosmosis (EO), electrophoresis (EP) and dielectrophoresis (DEP). In electrokinetic phenomena, electrostatic or Coulombic force, which is exerted upon charged fluids and suspended particles, is derived from the externally applied electrical field for inducing the movement in

electrokinetics (Qian and Ai, 2012). This external electrical field can be applied as DC (Direct Current) or AC (Alternative Current). The mechanism behind this phenomenon is briefly explained in the following subchapters.

1.4.1. Electrical Double Layer

Electrical Double Layer (EDL), which is responsible for the movement of charged ions in a fluid adjacent to a solid object, is the cornerstone of the electrokinetically driven microfluidic systems. When a charged solid surface interacts with suspended fluid, positively or negatively charged ions in the electrolyte are either attracted to or repelled from the surface (Hunter, 1981). Approximately after 10^{-7} seconds, which is the timescale for the system establishing Poisson – Boltzmann equilibrium, a charge cloud with nonzero charge density is observed near the surface (Halpern and Wei, 2007). This charge cloud is known as Electric Double Layer (EDL) as shown in Figure 1.6, which screens the electric potential of the surface charges. The EDL, which has a characteristic thickness of the order of 10 nm consists of the Stern layer and diffuse layer to the extent of electrolyte mobility (Probstein, 1994). Ions in the Stern layer are immobile because of the high surface attraction force; however, the ions within the diffuse layer are free to move. If the diffuse layer is sheared off via an externally applied electric field, the ions adjacent to the wall start to move from anion side to cation side and thus electroosmosis or electrophoresis are observed (Masliyah and Bhattacharjee, 2006). In electroosmosis, the fluid within the rest of microchannel is occupied by bulk solution leading to electrically neutral, i.e., same amount of positively and negatively charged ions, follows ion motion in the diffuse layer in electroosmosis.

Electrokinetically driven microfluidics is modeled via several methods, which are PNP (Poisson-Nernst-Planck), Poisson-Boltzmann (PB) and Debye-Hückel approximation. In some numerical models similar to this study EDL is

wholly left out of the consideration to decrease computational cost. Because the fluid domain is large enough to neglect the effects of EDL during computations.

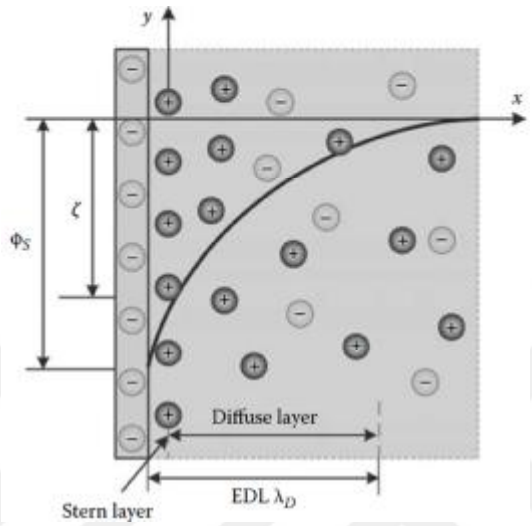

Figure 1.6. Charge distribution near a solid surface which holds nonzero electrical potential (φ_s). Electrical Double Layer (EDL) is illustrated as Stern Layer plus Diffuse layer (λ_D). Zeta potential (ζ) is induced in the shear plane, which is the defined boundary between the Diffuse layer and Stern layer (Qian and Ai, 2012).

1.4.2. Electroosmosis

If an external electric field is applied across a microchannel, ions in the diffuse layer of EDL migrate towards oppositely charged electrode, which results in dragging bulk fluid in the same direction (Li, 2004). This process is known as electroosmosis (EO) as demonstrated in Figure 1.7 (Sadeghi et al., 2013) which is identified by Reuss in 1809 (Arulanandam and Li, 2000). It is observed that velocity magnitude of the fluid, which is normal to the surface of the channel and increases within the EDL (Hunter, 1981). In bulk solution, the velocity is maximum and constant in every location. As a result, plug-like flow profile is generated dissimilar to parabolic flow profile, which is obtained in pressure-driven flow. Electroosmosis is a widely used mechanism for driving the fluid (Wang et al.,

2006). Zeta potential is an important parameter, which is the electrical potential on the interface of the Stern layer and diffuse layer (Sze et al., 2003). Electroosmotic fluid velocity is varied linearly with zeta potential and external electric field strength (Canpolat et al., 2013).

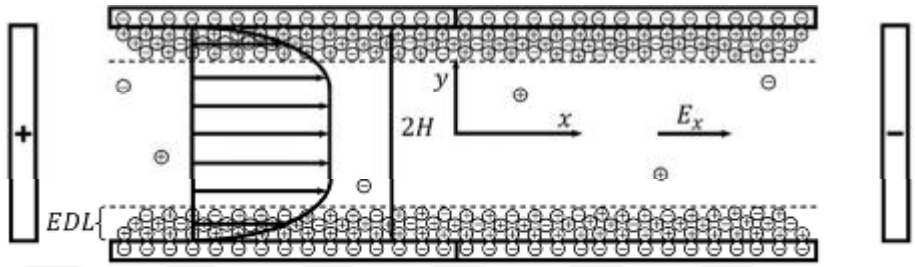

Figure 1.7. Illustration of electroosmosis phenomena with plug-like flow profile (Sadeghi et al., 2013)

1.4.3. Electrophoresis

Transport and manipulation of synthetic/bioparticles are emerging research field in microfluidics (Toner and Irimia, 2006). When a particle is confined in a charged solution, freely suspended ions in the electrolyte migrate towards the particle surface, and the EDL is formed as shown in Figure 1.8 schematically. Net motion of ions within the EDL triggers particle movement under the externally applied electric field, which is known as electrophoresis (EP) (Qian et al., 2006). EP is a popular method in microfluidics science because low heat dissipation is generated during processing, the higher electrical field could be utilized for rapid analysis, and sample/reagent consumption is relatively low (Wu et al., 2007). Therefore, many applications are governed with electrophoresis; such as sorting (Krüger et al., 2002), separation (Wainright, 2003), enzyme assay (Xue et al., 2001), immunoassay (Cheng et al., 2001).

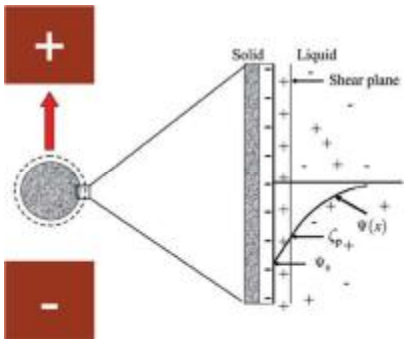

Figure 1.8. Formation of EDL around negatively charged particle in ionic media as well as electric potential distribution as regards particle surface (Velev et al., 2017)

1.4.4. Dielectrophoresis

Dielectrophoresis (DEP) is the motion of dielectric particles under non-uniform external electric fields (Pethig et al., 2010). DEP motion is observed only under non-uniform electric fields, which is the distinctive characteristics of DEP from the other electrokinetic phenomena previously listed in this study (Morgan and Green, 2002). Initially, the translational movement of particles is solely classified as DEP; however, the other electrokinetic effects, which drive the particles under non-uniform electric fields are also included to this topic (Srivastava et al., 2010). Travelling-wave electrophoresis and electrorotation are typical examples of non-uniformly induced electrokinetic effects.

DEP force is quite sensitive to the electrical properties of the media and the particle (Zhang et al., 2010). If the polarizability of the particle is higher than the media, DEP force takes positive value, otherwise negative DEP force is observed (Morgan and Green, 2002). Particles are directed to the higher electrical field regions in positive DEP (pDEP) and the lower electrical field regions in negative DEP (nDEP) (Frénéa et al., 2003), which is illustrated in Figure 1.9. Wide range of applications is carried out with DEP; such as particle separation (Pommer et al., 1992), detection (Gascoynea et al., 1997), mutation identification (Castellarnau et

al., 2006), immunosensing (Yamamoto et al., 2012) fabricating gas sensor (Suehiro, 2006).

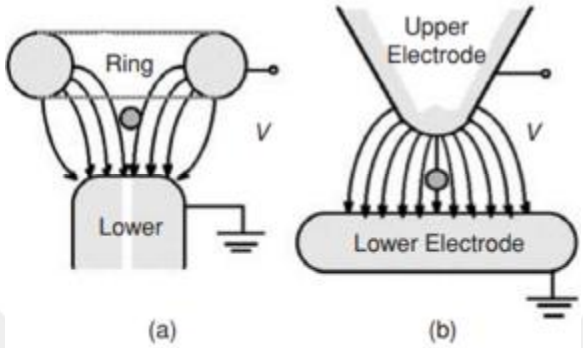

Figure 1.9. While moving direction of the particle is (a) towards to sparser electrical field region in nDEP, (b) opposite conditions are applied in pDEP (Jones, 2006).

1.4.5. Induced-Charge Electroosmosis

In linear electrokinetic phenomena, DC must be applied to maintain the electric field and targeted electric field strength is reached for high potential differences, which restrict the application area of electroosmosis and electrophoresis (Bazant and Squires, 2010). These drawbacks have created the need for nonlinear electrokinetic phenomena (Bazant and Squires, 2004). In nonlinear systems, the fluid velocity does not vary linearly with applied electric field strength, and the flow topology exhibits different characteristics than linear electrokinetics (Ramos et al., 1998, Ajdari, 2000). When an electric field is applied across an electrolyte solution containing a freely suspended polarizable material, ions in the electrolyte solution are attracted to the surface of the material. Thus, ions in the electrolyte solution migrate to either side of the material, and an induced EDL is formed around the conducting material (Squires and Bazant, 2004). This phenomenon is known as induced-charge electro-osmosis (ICEO), which is firstly termed by Squires and Bazant (2004). In conventional EO, the zeta potential of the surface is considered as a simple material property; however, it is induced by the

externally applied field in ICEO (Squires and Bazant, 2006). Meanwhile zeta potential is constant in conventional EO continuously; non-uniform zeta potential is exhibited in ICEO. This situation also yields dramatic difference in velocity magnitudes. In conventional electroosmosis, velocity magnitude is dependent on electrical field linearly; in ICEO, instead, this dependence is quadratic. The first power of electric field generates induced zeta potential, and the fluid flow is driven by the second power (Squires and Bazant, 2004). In contrast to linear electrokinetic phenomena, ICEO can be observed under AC and DC electric fields.

In ICEO, conducting material is electrically isolated from external electrodes. Therefore, the total charge on the conductor is fixed. On the other hand, the electric potential can be fixed according to external electrodes by means of charge flowing towards and off the material (Squires and Bazant, 2004). This phenomenon is known as fixed-potential ICEO. If non-uniform zeta potential is imposed to the channel walls, direction of the flow can be manipulated, thus mixing becomes possible using ICEO. Four identical vortices are obtained around the cylindrical conducting material, which has zero net charge density as shown experimentally in Figure 1.10. (Canpolat et al., 2013) and numerically in Fig 1.11 (Sharp et al., 2011). In case of nonzero charge density, the vortices are no longer identical, thus the symmetry in ICEO flow breaks down as indicated in Figure 1.12 (Squires and Bazant, 2004). The asymmetry in the flow field is presented for fixed potential ICEO as well as demonstrated in Figure 1.13 (Ren et al., 2013). In our study, whose flow field is represented in Figure 1.14, ICEO material is embedded upon the straight channel wall, which leads to two identical vortices. As a result, mixing performance of the system can be efficiently increased by implementation of ICEO.

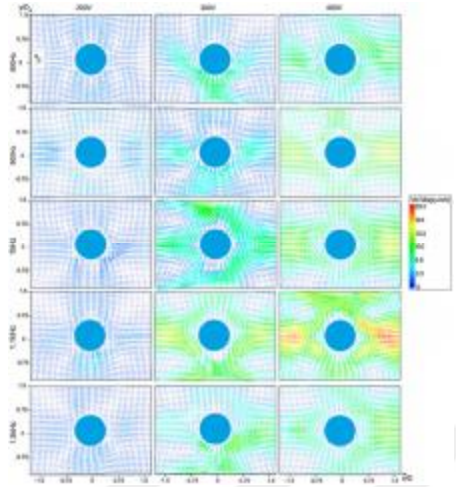

Figure 1.10. Created ICEO vortices with various potential differences and frequency values for external source around a conducting material with no charge density. (Canpolat et al., 2013)

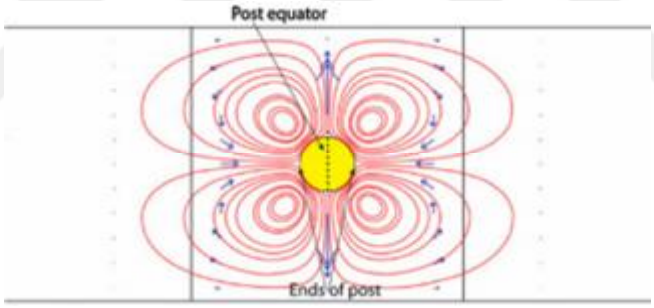

Figure 1.11. Numerical surface plots for velocity field around cylindrical ICEO electrodes (Sharp et al.)

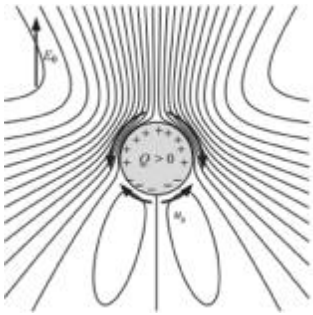

Figure 1.12. ICEO vortices around a conducting material with charge density (Squires and Bazant, 2004)

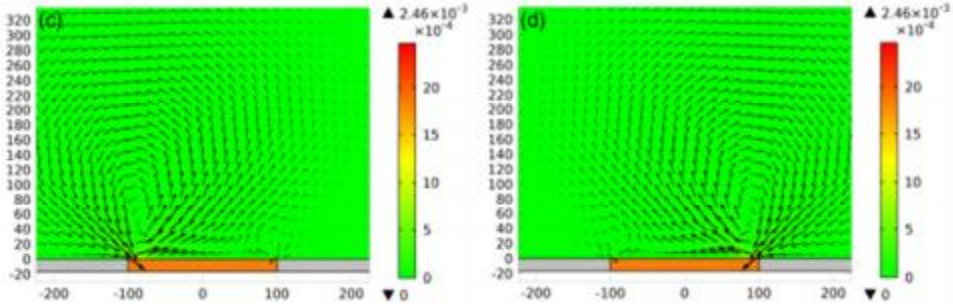

Figure 1.13. Asymmetric vortices of fixed-potential ICEO (Ren et al., 2013)

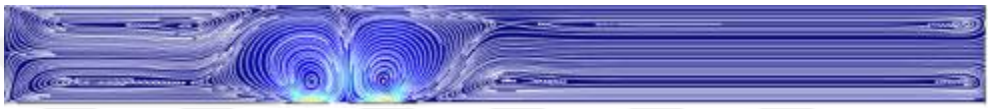

Figure 1.14. Two symmetrical vortices obtained upon ICEO material in our study

1.5. Mixing

Mixing is considered as one of the most widely seen application in microfluidics (Suh and Kang, 2010). These fields can be mainly categorized as chemical applications, analytical processes, and biological applications. Subcategories of chemical applications are a chemical synthesis, extraction, polymerization; analytical processes are Nuclear Magnetic Resonance Spectroscopy (NMR), Fourier Transform Infrared Spectroscopy (FTIR) or Raman spectroscopy and biological applications are enzyme assays, biological screening, protein folding (Jeong et al., 2009). Some applications could include the combination of two or more research fields, whose interactions are schematically represented in Figure 1.15. In biomedical engineering, mixing is exploited in many specific applications; such as enhancing antibody-antigen binding (Gao, 2015), enabling PCR (polymerase chain reaction) (Kim et al., 2009), nanoparticle synthesis (Valencia et al., 2010). Moreover, an efficient mixing must be secured for rapid analysis in a microfluidic chip (Fan et al., 2017).

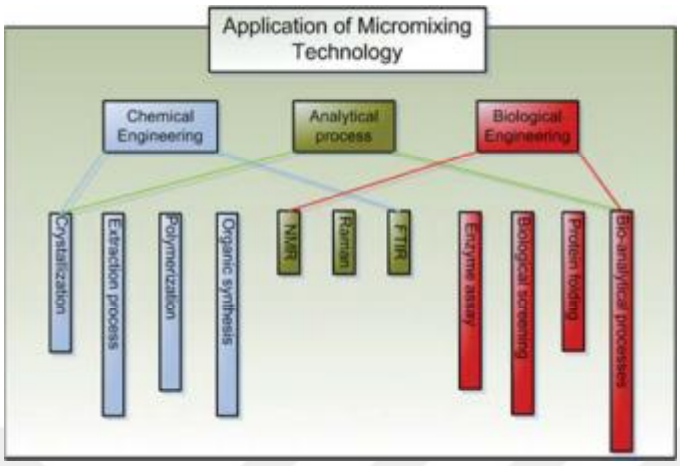

Figure 1.15. Application fields for micromixing (Jeong et al., 2009)

Mixing is majorly characterized by dimensionless Reynolds number (Re) and Peclet number (Pe). Reynolds number is the ratio of inertial forces over viscous forces (Frommelt et al., 2008). Due to microscale size, Reynolds number is quite low (Re<1) for microfluidics. That is, viscous forces are dominant over inertial forces in microfluidics systems, which pave the way for strict laminar velocity profile (Fowler et al., 2002). The Péclet number is the ratio of mass transport mechanisms, which are convection and diffusion (Lee et al., 2016). Under the low Reynolds number condition, mixing is dominated by molecular diffusion of chemical species, which requires excessively long micro channel and mixing duration. (Chang and Yang, 2004). On the other hand, surface to volume ratio is dramatically high in microscale, which is an advantage for the mixing (Yang et al., 2005). The key to adequate mixing is creating an extensive contact between the fluids, by this means, decreasing time for the diffusion (Afzal and Kim, 2015).

Mixers are broadly classified into two categories: passive mixers and active mixers (Nguyen and Wu, 2005). Passive mixers, which are based on the channel configurations and molecular diffusion, have geometrical complexity as compared to active mixers. The designs are carried out for the enhancing the interfacial contact of the fluids to be mixed. T-shaped and Y-shaped microchannel

inlet configurations are the fundamental designs for mixing applications (Galletti et al., 2012). Also, the obstacles, flow compression, zig-zag channels, nozzles, channel branching, the plates with multi-holes are used for passive mixing (Hessel et al., 2005). Assay sensitivity may be lower in passive mixers, because of the hydrodynamic dispersion (Harnett et al., 2008). Types of passive mixing techniques are schematically shown in Figure 1.16. For active micromixers, external energy supply is required to run the system for increasing the mixing performance (Shamloo et al., 2016). Acoustic, dielectrophoretic, electrokinetic time-pulse, pressure perturbation, electro-hydrodynamic, magnetic and thermal techniques are the external energy supplies, which are used in active mixers (Lee et al., 2011). List of active mixing methods is represented in Figure 1.17.

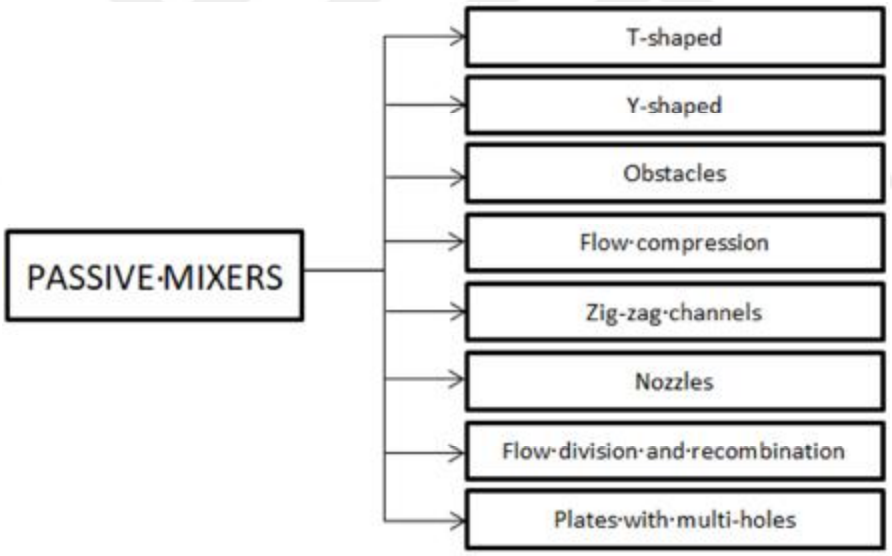

Figure 1.16. Passive mixer types (Hessel et al, 2008)

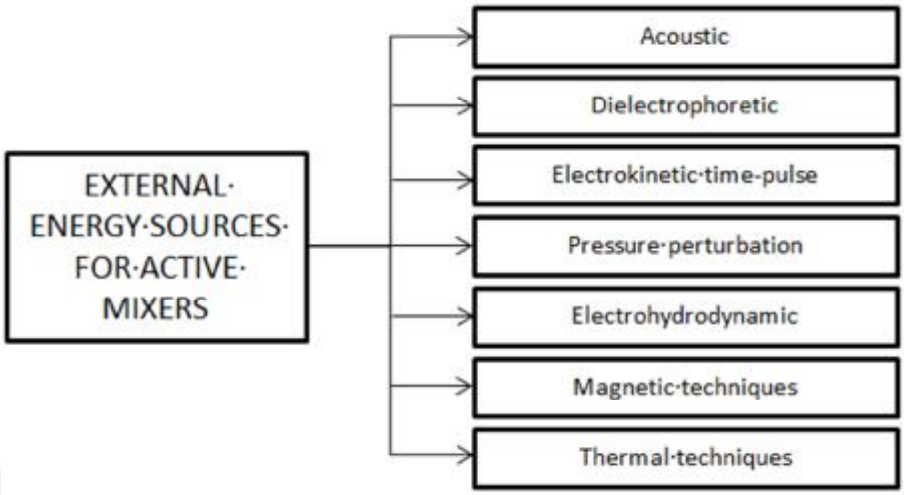

Figure 1.17. External energy sources used for active mixing (Lee et al., 2011)

1.6. Objective of the Study

In this work, optimum parameters of an efficient pulsatile flow micromixer coupled with a nonlinear electrokinetic effect are aimed to be determined numerically. Newtonian, Power-law, and Carreau models for the fluids are used for numerical analyses. Induced-charge electro-osmosis (ICEO) is generated around a floating electrode, which is embedded in a wall of the straight microchannel to create disturbance along the interface between two fluid streams. To decrease mixing length, a rectangular obstruction is placed upon channel wall, where the floating electrode is located. The magnitude of the external electric field, the length of floating electrode, the frequency of pulsatile flow and the width of rectangular obstruction are systematically varied to constitute a comprehensive parametric study. Their effectiveness on micromixing is studied using time-dependent distributions of streamlines, concentration, and vorticity. Moreover, mixing index values are plotted according to obstruction width, electrode length, and Strouhal number. The resulted mixing index values are compared among Newtonian, Power-law, and Carreau models under same circumstances.

2. LITERATURE SURVEY

Topics of microfluidics, non-Newtonian fluids, pressure-driven flow and electrokinetics, are within the scope of the present investigation. The studies, which are incorporated within these fields, are reviewed in compliance with the specific application of this study, namely mixing. This review includes both experimental and numerical works. Due to scope of current investigation; the studies in macroscale with same topics are not taken into consideration.

2.1. Mixing with Non-Newtonian Fluids

Investigating non-Newtonian fluid behavior is an attractive and significant topic for the researchers. Das and Chakraborty (2006) analyzed investigating the velocity, temperature and concentration distribution of a biofluid under pure electroosmotic flow conditions. The coefficients of power-law model were determined based on the experimental solutions as the aim of their work. Numerical solutions according to specified model parameters agreed well with the experimental results as shown in Figure 2.1. These coefficients are preferred in the present study. Zhao and Yang (2011) conducted numerical work for understanding non-Newtonian behavior under electroosmotic flow conditions. The viscosity of the fluid was described with the power-law model. With the lower fluid behavior index value (n), more plug-like flow was observed across the cross-section of the channel and fluid velocity decreases towards to the upper and lower boundaries of the channel with increasing EDL thickness as shown in Figure 2.2, respectively. Tang et al. (2009) investigated non-Newtonian fluid flow under pressure driven as well as electroosmotic flow conditions. Power-law model was used for modeling viscosity behavior. Parabolic flow profile was sharpened with increasing n value for both flow mechanisms as shown in Figure 2.3. The same rule was valid, when EDL thickness increases. Goswami et al. (2015) investigated non-Newtonian fluid flow. Velocity distribution and volumetric flow rate were determined for Power-

Eyring fluid and compared to the case of a Newtonian fluid. The slip length was defined as the distance where velocity magnitude decreases to zero. This length was used for evaluating the variations in the considering parameters. The results of these parameters are presented in Figure 2.4 and Figure 2.5, respectively.

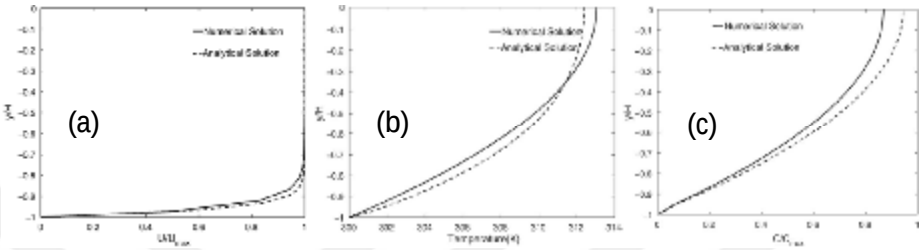

Figure 2.1. Experimental results as compared to numerical solutions for the parameters of (a) velocity distribution (b) Temperature distribution (c) Concentration distribution (Das and Chakraborty, 2006)

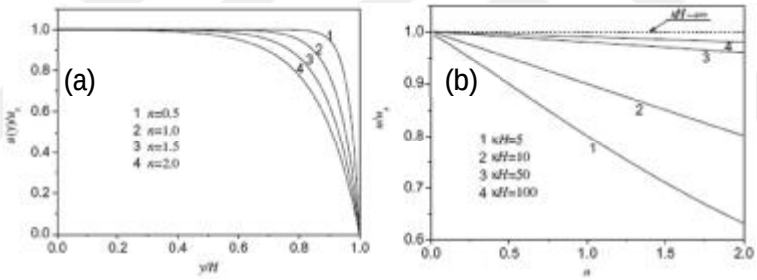

Figure 2.2. (a) Velocity distribution for the cross-section of the microchannel about different n values (b) Velocity distribution according to various channel width-EDL thickness ratio with different n values (Zhao and Yang, 2011)

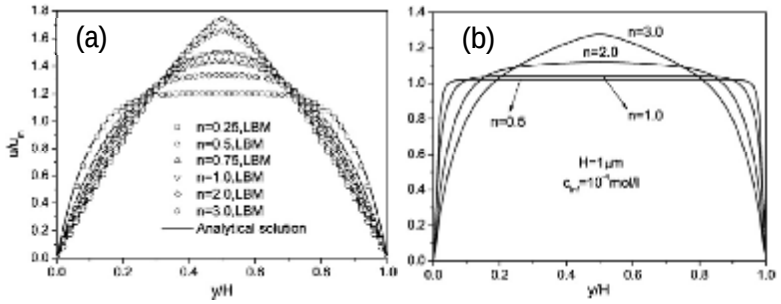

Figure 2.3. Flow profile for (a) pressure-driven flow and (b) electroosmotic flow (Tang et al., 2009)

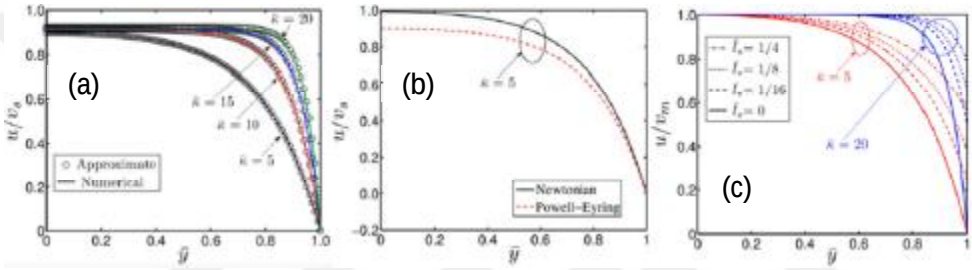

Figure 2.4. Velocity distribution for (a) Powell-Eyring fluid under various EDL thicknesses (b) Newtonian and Powell-Eyring fluids under single EDL thickness (c) various slip velocities (Goswami et al., 2015)

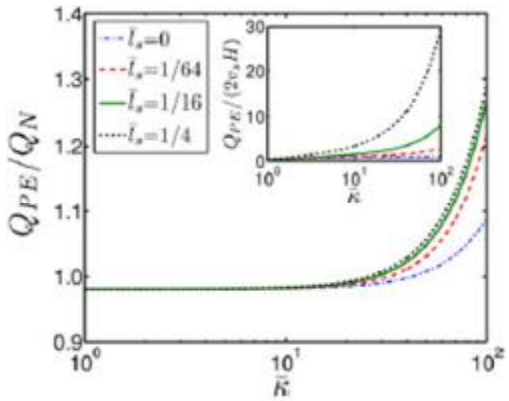

Figure 2.5. Ratio between volumetric flow rates of Powell-Eyring and Newtonian fluids for various slip velocities (Goswami et al., 2015)

Channel geometry is a highly influential factor on micromixing. Hadigol et al. (2011) investigated micromixing for uniform straight channel. Fluid was driven electrokinetically, and EDL was modeled according to Poisson-Boltzmann approach and non-uniformities were defined for the surface potential on microchannel boundaries. By using creation of the vortices, strong perturbations are observed along the flow. Concentration distributions are evaluated according to various flow behavior index (n) values for every cross-section of the microchannel as shown in Figure 2.6. Reynolds number was utilized for describing mixing efficiencies with various n values as illustrated in Figure 2.7. Cho et al. (2012) investigated mixing efficiency along microchannels, which include rectangular or wavy blocks as demonstrated in Figure 2.8. Higher mixing efficiencies were obtained for both longer rectangular and wavy blocks with increasing surface potential as shown in Figure 2.9a. Moreover, the better mixing efficiency was achieved for rectangular blocks compared to wavy blocks as shown in Figure 2.9b. Afzal and Kim (2014) conducted a numerical micromixing study in T-shaped and serpentine microchannels. Fluid viscosity was defined using Carreau and Casson models. Mixing index values were calculated for various mass flow rates as shown in Figure 2.10. Higher mixing index values were obtained for the lower mass flow rates due to the lower velocity magnitudes. Kunti et al. (2017) proposed a numerical micromixer which operated with non-Newtonian fluids. While electrode pairs were defined to the upper boundary, the grooved pattern was imposed to the lower boundary. The shear dependency of the fluid viscosity was modeled using power-law approach. The fluid was driven by AC electrothermal micropump. Mixing performance increased with rising flow behavior index values in contrast with aforementioned studies, which is seen in Figure 2.11.

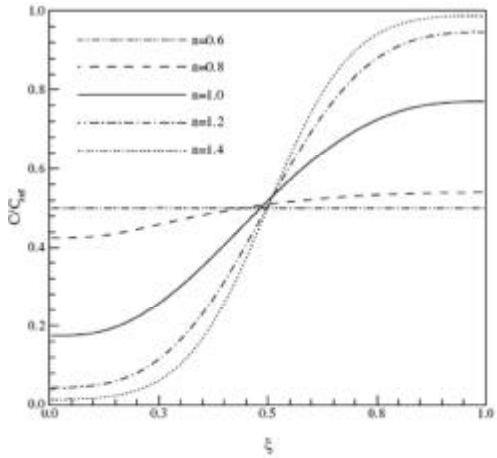

Figure 2.6. Concentration distributions in every cross-section of the microchannel for various flow behavior index values (Hadigol et al., 2011)

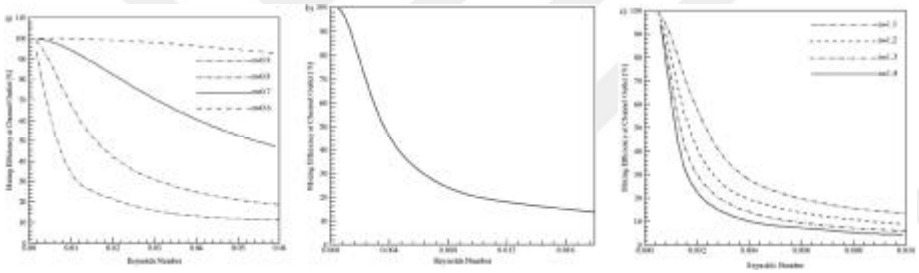

Figure 2.7. Mixing efficiencies for (a) Shear-thinning fluid (b) Newtonian fluid (c) Shear-thickening fluid (Hadigol et al., 2011)

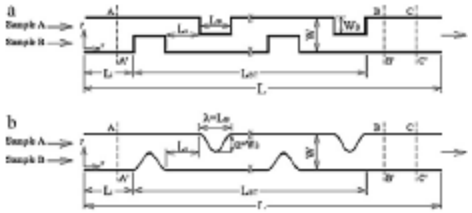

Figure 2.8. Schematic of a microchannel with (a) Rectangular blocks (b) Wavy blocks (Cho et al., 2012)

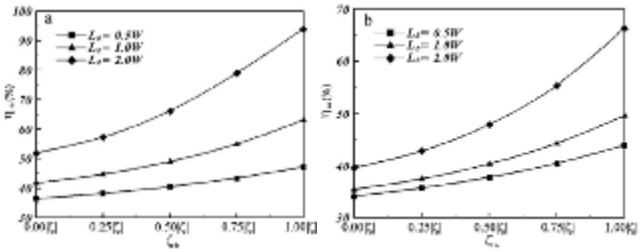

Figure 2.9. Mixing efficiencies according to various block lengths with increasing surface potentials for (a) Rectangular blocks (b) Wavy blocks (Cho et al., 2012)

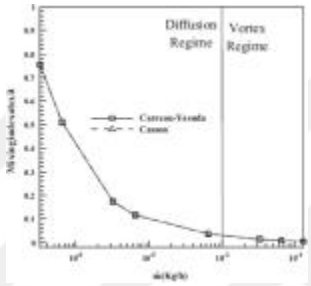

Figure 2.10. Mixing index values for Carreau and Casson models under various mass flow rates (Afzal and Kim, 2014)

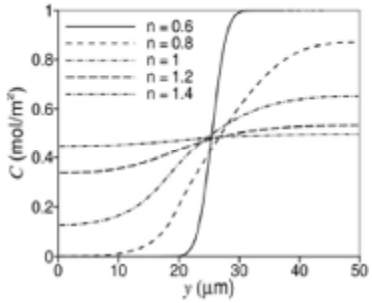

Figure 2.11. Concentration profiles at the outlet (Kunti et al., 2017)

Stirred tanks are useful tools and thus, widely appealed for micromixing applications. Shamsoddini et al. (2012) numerically investigated non-Newtonian fluid mixing in a tank, which includes stir bar (Figure 2.12). Various flow behavior index values under distinct Strouhal numbers as well as two different Reynolds numbers were tested for mixing efficiencies. Higher mixing efficiencies were

obtained for both lower Strouhal numbers and higher flow behavior index values as shown in Figure 2.13. Han et al. (2012) numerically investigated micromixing effect on chemical reactions in a tank. The experimental conditions were simulated with the discretization of feeding time for decreasing computational work load. In their study, fresh feeds were introduced to the exhausting portions, consecutively. Mixing performance was enhanced with the lower viscosities and higher agitation speeds. Therefore, the reaction rate was increased. It is concluded that mixing performance was also influenced by reaction plum trajectory. The volume of reaction plum approaches to the maximum in the mixing-reaction process as seen in Figure 2.14.

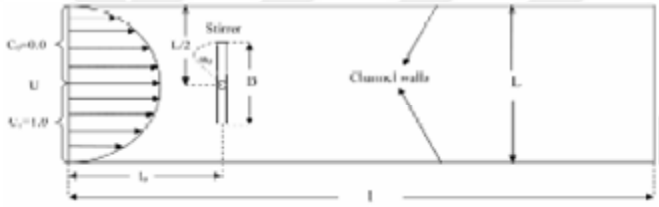

Figure 2.12 Modelled stirred tank (Shamsoddini et al., 2012)

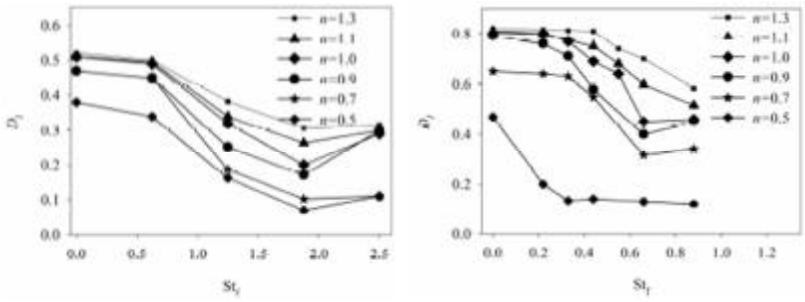

Figure 2.13. Mixing performances for various Strouhal numbers under Re=20 (b) Re=72 (Shamsoddini et al., 2012)

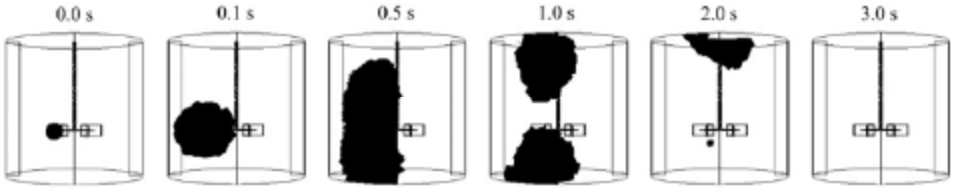

Figure 2.14. Reaction plum volumes in the stirred tank during the numerical analysis (Han et al., 2012)

2.2. Mixing with Pulsatile Flow

Pulsatile flow is a sub-branch of time-dependent or unsteady flow regimes (Özdinç Çarpınlıoğlu and Gündoğdu, 2001). Periodically oscillating velocity profile is generated using pulsation. Pulsatile flow has critical importance for biomedical engineering because blood flow in human arteries is typically described as a non-Newtonian pulsatile flow, which is surrounded by a tapered elastic conduit (Yılmaz and Gündoğdu, 2008). The first study in pulsatile flow in open literature was proposed by Sexl (1930), and this study was adapted to the blood flow in arteries by Womersley (1955) according to the report of Rao and Devanathan (1973). Pulsatile flow characteristics investigated by Tikekar et al. (2010), experimentally. The results for average root-mean-square (RMS) pressure drop were presented as a function of duty cycle, pulsation frequency, and mass flow rate. Average flow rate behaved linearly with the flow rate, whereas RMS pressure increased quadratically. While average pressure drop was linearly proportional to flow rate, quadratic increase was observed for RMS pressure. Moreover, RMS pressure was linearly dependent to pulsation period and there was no natural variation between duty cycle. Mass transport was another central component of the present study. Horner et al. (2002) reported that the pulsatile flow could enhance mass transport.

Pulsatile flow can be generated via micropumps as mentioned in the previous chapter. However, heating and friction effects were derived from mechanically moving parts. Wang et al. (2011) proposed a pulsation system with no moving parts as schematized in Figure 2.15. The actuator was driven by the

thermal bubble and acted analogously to the human heart. Moreover, it can be used for biological applications due to thermal bubble, which was suspended inside the actuator. When the actuator was utilized for mixing applications, 94% of mixing efficiency was acquired at high frequencies. In some researchers, the pulsation was generated by dynamic controllers, such as solenoid valves (Nauman et al., 1999), voltage supplies (Egnor et al., 2002) and function generators (Shiose et al., 2010). Similarly, Kim et al. (2015) developed an oscillator, which can generate pulsations without dynamic controllers as shown in Fig 2.16. Gravity water head generates flow, thereby system was designed without dynamic controllers. Moreover, complexity and cost of the system were significantly reduced. However, switching frequency could be increased with only increasing flow rate, which leaded to low mixing efficiency. Li and Kim (2017) solved this problem by distinguishing oscillation and mixing components of the system as shown in Figure 2.17. Therefore, the component of mixer controlled the flow rate, while oscillator controls switching frequency,

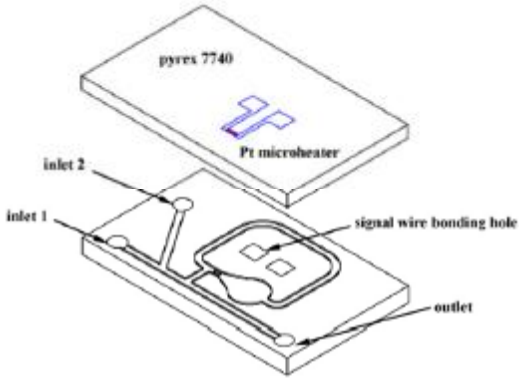

Figure 2.15. Schematic of the bubble-driven actuator (Wang et al., 2011)

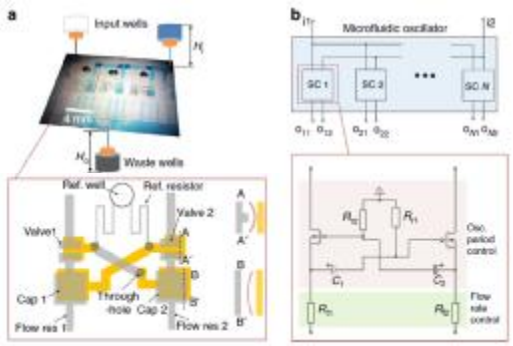

Figure 2.16. (a) Image for oscillator array chip and schematic of single oscillator sub-circuit (b) Schematic of the microfluidic oscillator (Kim et al., 2015)

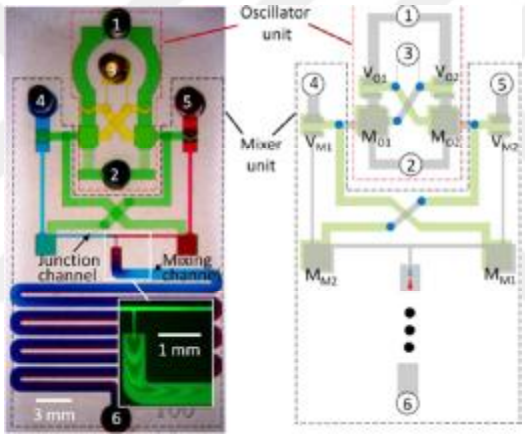

Figure 2.17. (a) Photograph of the components of micromixer (b) Schematic of the components of micromixer (Li and Kim, 2017)

Pulsatile flow is significantly affected by microchannel geometry. Goullet et al. (2006) numerically investigated mixing efficiency whether ribs exist along the lower wall of the microchannel. Mixing efficiency was increased with ribs, even better mixing was obtained for out-of-phase (180°) pulsing. The concentration profiles were depicted for four different configurations in Figure 2.18. Ammar et al. (2014) investigated mixing of pure water and Rhodamine B for four different geometries, which possess same width and length. These geometries were right angle intersection, Y intersection, T intersection and arrowhead intersection, as

seen in Figure 2.19. The best mixing was performed using arrowhead intersection in their study. Afzal and Kim (2015a) numerically investigated pulsatile flow mixing in various types of channel geometries which were straight, square wave, zigzag, sinusoidal, convergent-divergent as shown in Figure 2.20. The best mixing performance was obtained from convergent-divergent with out-of-phase pulsing. This model was optimized with a numerical method by the same authors (Afzal and Kim, 2015b). Cortelezzi et al. (2017) proposed a scalable micromixer, which is depicted in Fig 2.21. Although the diameter of microchamber, where the mixing occurs, was altered for which same dimensionless numbers (Reynolds, Péclet, and Strouhal), and mixing efficiency remained constant.

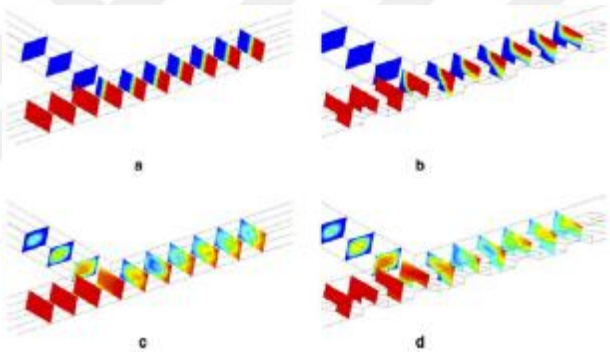

Figure 2.18. Concentration profiles of two species with (a) no pulsing and no obstacles (b) no pulsing and ribs (c) pulsing and no ribs (d) pulsing and ribs (Goullet et al., 2006)

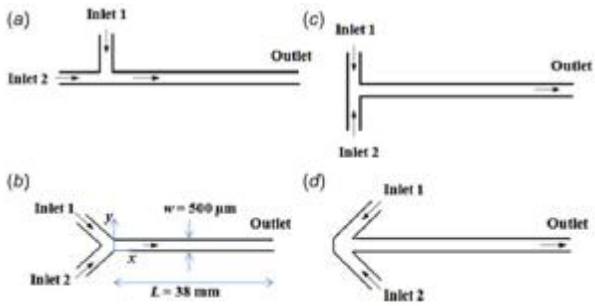

Figure 2.19. (a) Right angle intersection (b) Y intersection (c) T intersection (d) arrowhead intersection (Ammar et al., 2014)

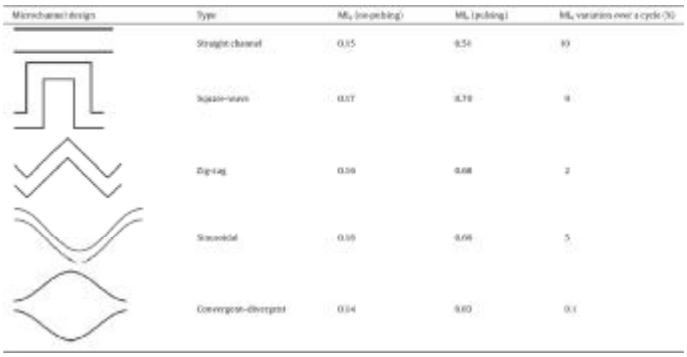

Figure 2.20. Investigated microchannel geometries and corresponding mixing indexes (Afzal and Kim, 2015a)

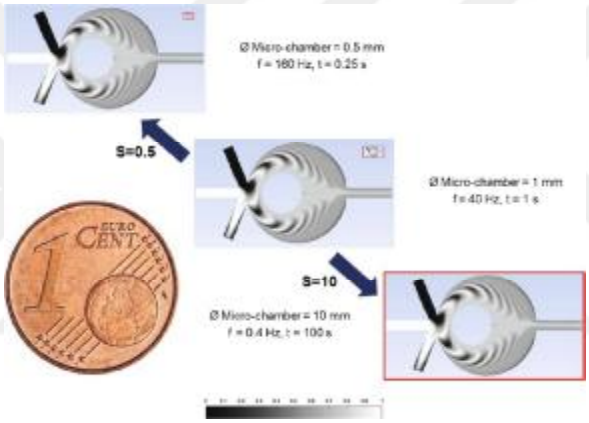

Figure 2.21. Same mixing indexes are obtained for different size of microchambers in the work of Cortelezzi et al. (2017)

It can be reported that pulsatile flow enables to create perturbations along flow streams. Therefore, the pulsatile flow has the capability of being a useful tool for mixing applications, especially in micron scale. Accordingly, mixing performances of steady flow and pulsatile flow are compared in the numerical work of Karami et al. (2014). Micromixing was performed in an irregular geometry, which was bent at some locations as shown in Figure 2.22. Mixing performances were evaluated at the inlets of these bends and the velocity amplitude ratio (β), which was defined as the fraction of the peak pulsatile velocity and steady velocity. Better mixing performance was obtained for all inlets and β values with

the pulsatile flow as shown in Figure 2.23. Glasgow and Aubry (2003) also reported that pulsation was able to increase micromixing in T-shaped channels. Moreover, a further increase in mixing efficiency was provided with the additional pulsation from another inlet. Specifically, the better mixing was obtained for pulsation from microchannels with two inlets compared to that of the single inlet. Maximum mixing efficiency was obtained for out-of-phase pulsing, which agreed with the work of Goullet et al. (2006). Xia and Zhong (2013) were conducted an experiment, which is schematized in Fig 2.24a, for mixing two water streams under pulsatile flow condition. Mixing was performed in Y-shaped jet configuration as shown in Fig 2.24b. The vortices were produced using pulsation, thus mixing performance of the system was enhanced. In this study, the best mixing performance was obtained by out-of-phase pulsing. Bottausci et al. (2006) developed an efficient and rapid micromixer via pulsation. The system consisted of two inlets and six secondary channels as shown in Fig 2.25. Fluids were driven with a steady flow from inlets and vortices were generated by pulsatile flow from the secondary channel (Fig 2.26).

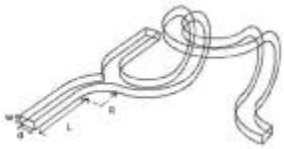

Figure 2.22. Bended geometry which is used in the work of Karami et al. (2014)

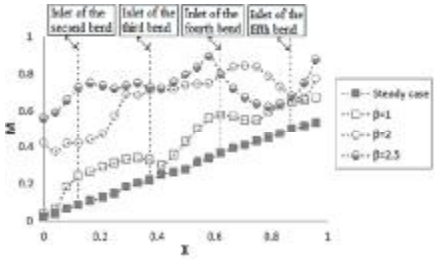

Figure 2.23. Mixing performance for steady flow and pulsatile flow with different β values (Karami et al., 2014)

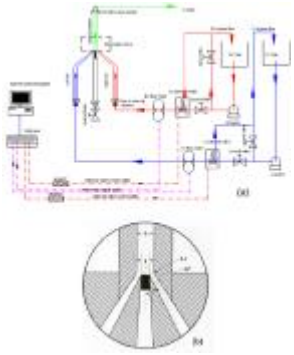

Figure 2.14. (a) Schematic of the experimental setup (b) Y-shaped jet configuration (Xia and Zhong, 2013)

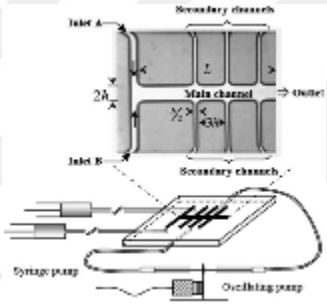

Figure 2.25. Schematic of the developed micromixer (Bottausci et al., 2006)

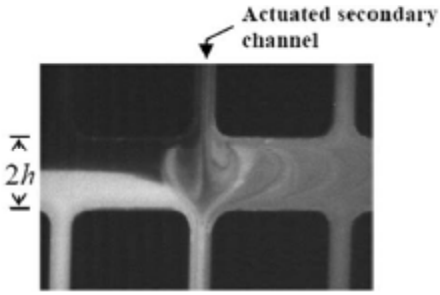

Figure 2.26. Generated vortices at the intersections (Bottausci et al., 2006)

Dimensionless numbers are critical parameters, which are utilized for characterizing the mixing performance of the system. Reynolds number (Re), Péclet number (Pe) and Strouhal number (St) are always investigated in the studies above versus mixing performance of the system. Effects of these dimensionless

numbers, as well as Stokes number (Sto) and pulse volume ratio (PVR) on mixing index, were compiled in the numerical study of Glasgow et al. (2004) under pulsatile flow conditions. Stokes number is defined as the ratio of time duration for fully developed flow to the period ($Sto = (fL^2)/v$). PVR is a proposed parameter by the authors of this study for defining the ratio between pulsed fluid volume to inlet as well as to outlet. Mixing performance was particularly influenced by Stokes number, Strouhal number and PVR as shown in Fig 2.27 and Figure 2.28, respectively. Tanthapanichakoon et al. (2006) reported mixing performances inside slugs, which were modelled two-dimensionally (2D) or three-dimensionally (3D). Slug geometries are depicted in Fig 2.29. Mixing performances of the slugs were characterized by a novel dimensionless number, which was termed as modified Peclet number (Pé*) as shown in Figure 2.30a. Pé* was defined as the ratio between diffusive time scale and convective time scale ($Pé^* = U_s d_s^2/lD$). U_s was defined as steady velocity of the fluid. Although, mixing durations were evaluated with this parameter as shown in Figure 2.30b, mixing quantification was not investigated under pulsatile flow conditions.

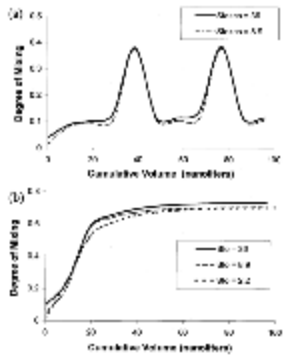

Figure 2.27. Mixing index variations for different Stokes numbers. Due to (a) St = 0.094 and PVR = 1.88 (b) St = 0.375 and PVR = 1.88, it can be concluded that mixing index can be significantly altered by St numbers (Glasgow et al., 2004)

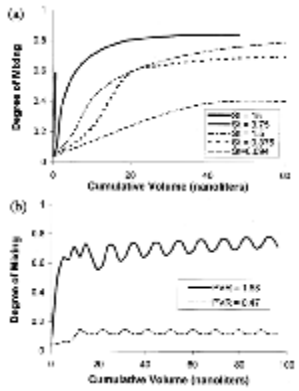

Figure 2.28. Mixing performances for (a) various Strouhal number and constant PVR which equals to 1.88 and (b) two PVR values (Glasgow et al., 2004)

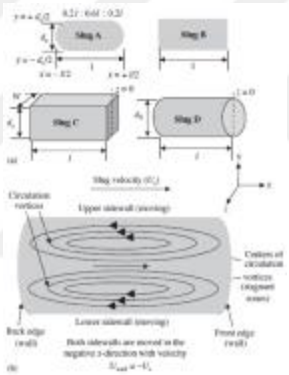

Figure 2.29. (a) 2D or 3D slug geometries with boundary length symbols
(b) Generated vortices inside the slugs (Tanthapanichakoon et al., 2006)

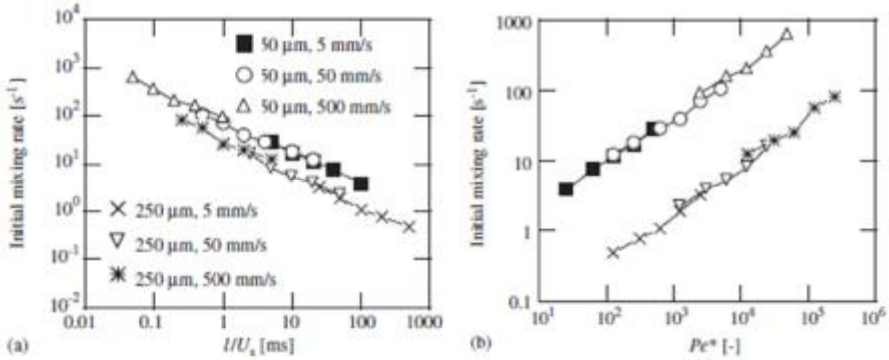

Figure 2.30. (a) Mixing index against l/U_s (b) Mixing index against the modified Péclet number (Tanthapanichakoon et al., 2006)

2.3. Mixing with Induced-Charge Electro-Osmosis

Induced-Charge Electro-Osmosis (ICEO) is a robust mechanism for mixing applications due to its capability of creating strong perturbations along the streamline via vortices. Various components affect the ICEO, such as the magnitude of external potential difference, size, and shape of conducting material. Feng et al. (2016) investigated EO and ICEO mixing according to channel geometry. Mixing application was carried out in an eccentric annulus, which is depicted in Figure 2.31, with the endorsement of Lagrangian chaos. Homogenous mixing was provided for both driving mechanisms under a second as shown in Figure 2.32. However, superior mixing performance was obtained using ICEO compared to EO. Alapati et al. (2011) governed a numerical ICEO mixing study in a microcavity. ICEO electrode was embedded in the bottom of the microcavity as depicted in Fig 2.33. Mixing performance was enhanced further by via external DC potential. Due to redistribution was ensured by switching on and off (charging and de-charging processes), the parallelism between equicharge and equipotential lines were disturbed and creating additional vortices are enabled which as in Fig 2.34.

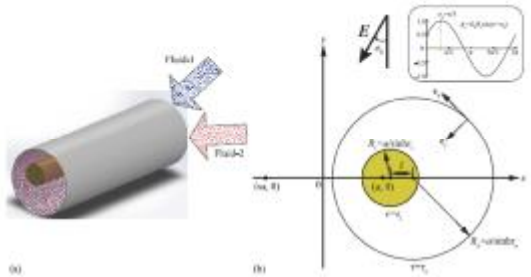

Figure 2.31. (a) Illustration of eccentric annulus (b) Demonstration of eccentric annulus according to cylindrical coordinate system Feng et al. (2016)

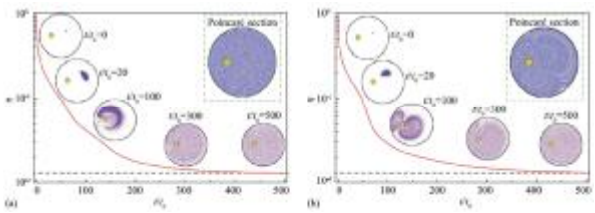

Figure 2.32. Mixing performances for dimensionless time scale of (a) EO (b) ICEO configurations. Perfect mixing is described with dashed line (Feng et al., 2016)

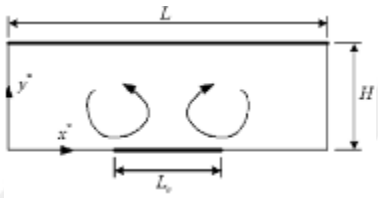

Figure 2.33. Microcavity which mixing occurs (Alapati et al., 2011)

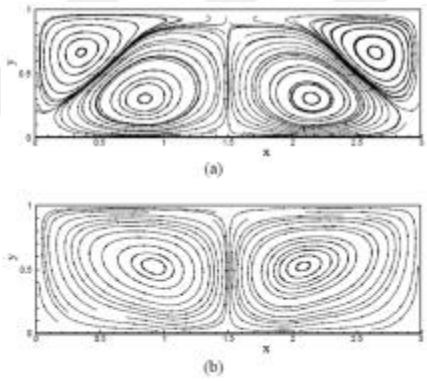

Figure 2.34. Streamlines for (a) switching on and (b) switching off stages (Alapati et al., 2011)

Charges adjacent to the floating electrode are induced and correspondingly electrolytes in the solution are attracted or repelled in ICEO. This mechanism is strongly dependent on the floating electrode geometry. Wu and Li (2008a) investigated ICEO mixing with a pair of triangular electrodes, numerically. Mixing performance of the system was dramatically increased with ICEO, which is illustrated in Fig 2.35. Further simulations were performed by the same authors

(2008b). The number of electrode pairs was increased as well as cylindrical and rectangular electrode shapes were defined. Mixing indexes of these configurations were investigated along with varying electrode numbers as shown in Fig 2.36. Rectangular electrodes exhibited the best mixing performance with the number of three. Also, numerical models were validated with experimental procedures which are depicted in Fig 2.37. Jain et al. (2009a) proposed a numerical ICEO mixer, which possessed cylindrical electrodes. The EDL was also modeled with PNP method for total concentration of charged species. Effects of cylindrical electrodes radii and the EDL thickness on mixing indexes were reported. Although mixing index was proportional to electrode size, inverse proportionality was observed against the EDL thickness in their study. Results are shown in Figure 2.38 and Figure 2.39, respectively. This research was extended according to different shaped ICEO electrodes by the same authors (2009b). In their study, cylindrical, triangular, rectangular and right angle triangular electrodes were tested for micromixing. On the other hand, EDL was discarded from the model due to enlarging in channel width. Higher Péclet number was obtained from the design, which also derives from enlarging in channel width. The best mixing performance was provided by the right triangular electrode as clearly shown in Fig 2.40. Zhang et al. (2012) numerically analyzed a micromixer, which incorporates cylindrical Janus and conducting materials as ICEO electrode. The center of ICEO electrodes were embedded into the midline of the U-shaped microchannel as shown in Fig 2.41. While four vortices were observed around conducting particle, two and smaller vortices occured around Janus particle. Approximately, 90% of mixing efficiency was obtained under various DC electric fields. Harnett et al. (2008) performed an ICEO micromixing analysis with triangular electrodes. The triangular electrodes were aligned in a horizontal direction, successively. The analysis was carried out both numerically and experimentally as shown in Fig 2.42. Mixing efficiency was quantified by the mixing metric, which is described mathematically in Fig 2.43 as well as the results of numerical and experimental analyses.

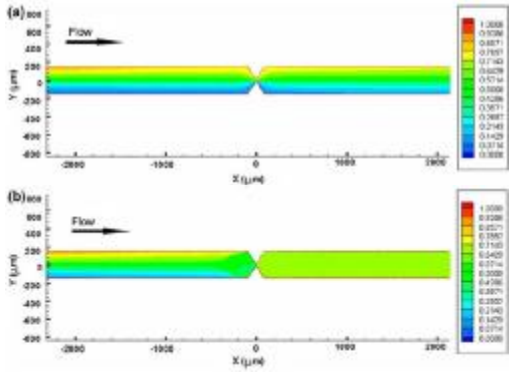

Figure 2.35. Concentration profiles for (a) non-conducting triangular electrodes i.e. ICEO is inactive (b) conducting triangular electrodes i.e. ICEO is active (Wu and Li, 2008a)

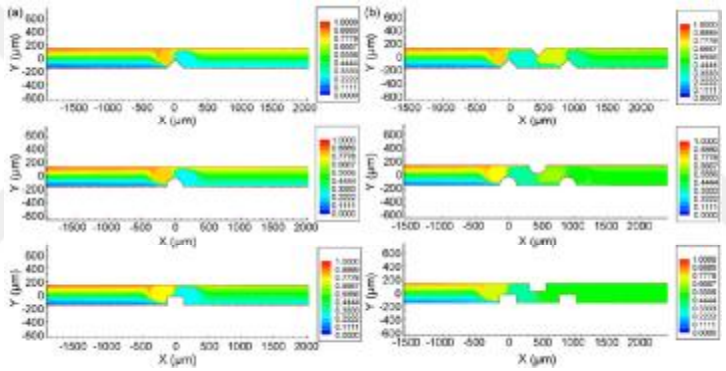

Figure 2.36. Concentration distribution for (a) single ICEO electrode (b) three ICEO electrodes (Wu and Li, 2008)

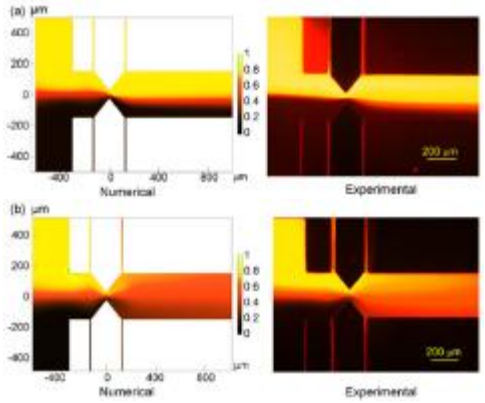

Figure 2.37. Experimental validation of the proposed model (Wu and Li, 2008)

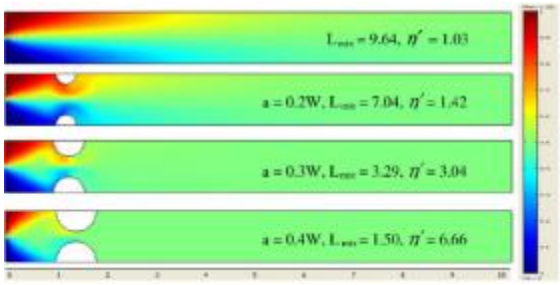

Figure 2.2. Mixing indexes (η') for different sizes of ICEO electrodes. Efficient mixing is also achieved without ICEO which derives from the small Péclet number (Jain et al., 2009a)

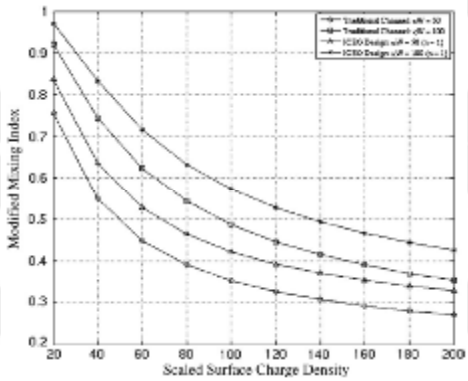

Figure 2.39. Mixing index variations according to different EDL thickness. Surface charge densities remain constant (Jain et al., 2009)

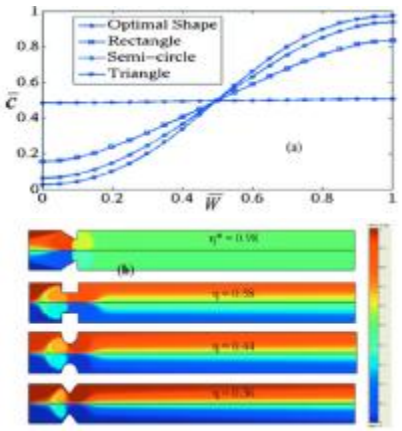

Figure 2.40 (a) Concentration profiles at the outlet of the microchannel for different electrode shapes (b) Concentration profiles on the 2D surface for different electrode shapes (Jain et al., 2009b)

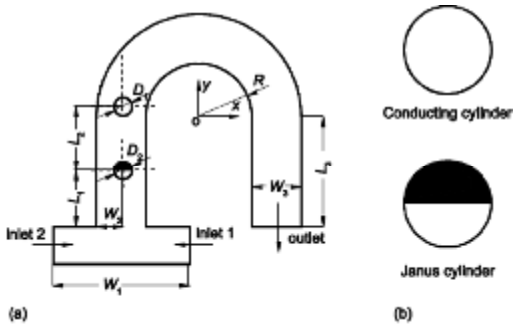

Figure 2.41. (a) Schematic of U-shaped microchannel geometry (b) Schematics of conducting cylinder and Janus cylinder (Zhang et al., 2012)

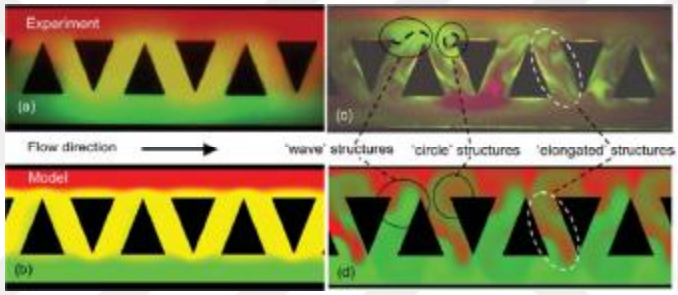

Figure 2.42. Flow visualization after loading the fluids (a, b) and mixing (c, d) for experimental (a, c) and numerical (b, d) studies (Harnett et al., 2008)

$$M = 1 - \frac{M'}{M'_0}, \quad M' = \frac{\int |m - \bar{m}| dv}{v} \qquad \text{(a)}$$

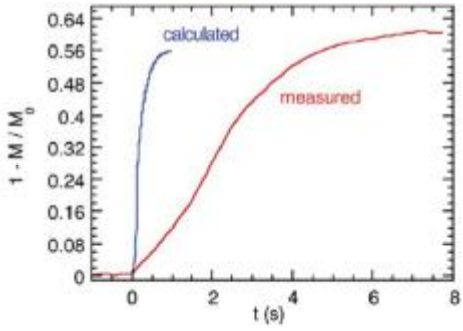

(b)

Figure 2.43. (a) Calculation of mixing metric. (b) Mixing metric results for numerical and experimental analyses (Harnett et al., 2008)

If a particle is suspended in a conductive medium, electrophoresis phenomena is considered. Kazemi et al. (2017) numerically analyzed induced-charge electrophoresis (ICEP). A conducting particle was defined in the middle of the microchannel as depicted in Fig 2.44. Mixing efficiency was investigated under the variations of electrical fields (Figure 2.45) and the distance between two inlet boundaries (Figure 2.46) as well as induced zeta potential magnitude with various particle diameter (Figure 2.47).

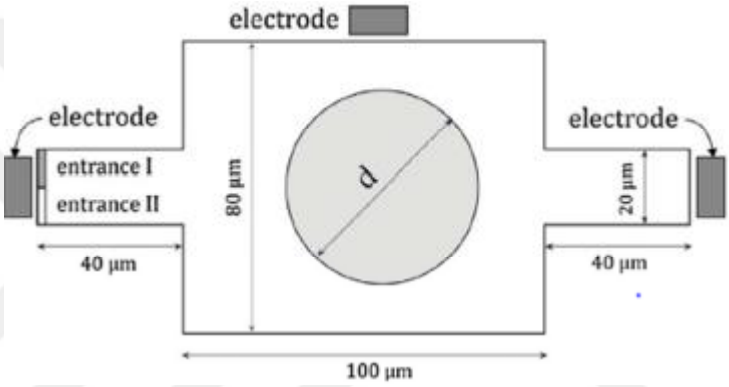

Figure 2.44. Defined microparticle in the microchannel with dimensional parameters for the application of ICEP (Kazemi et al., 2017)

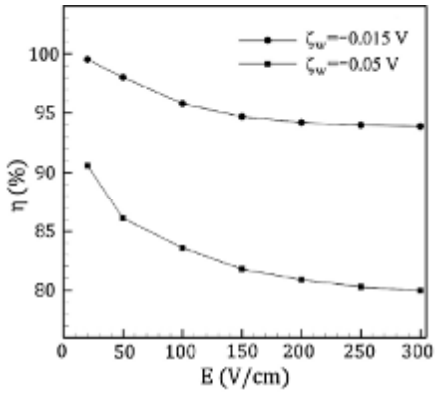

Figure 2.45. Mixing efficiency variations under various electrical fields compared to two different zeta potentials on the upper and lower walls of the channel (Kazemi et al., 2017)

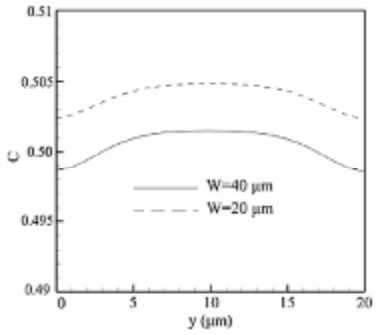

Figure 2.46. Mixing index variations for the distance between two inlet boundaries of the channel (Kazemi et al., 2017)

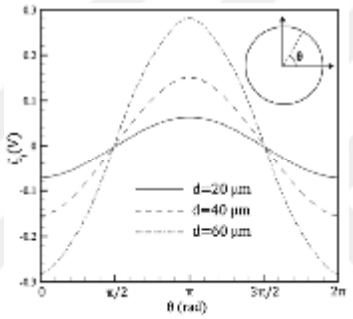

Figure 2.47. Induced zeta potential variations according to variations in the particle diameter (Kazemi et al., 2017)

Until this point, mixing applications were conducted with fixed charge ICEO, i.e. symmetric vortices. Mixing efficiency under asymmetrical vortices was investigated by Wu et al. (2017). Asymmetrical vortices were generated by fixed potential ICEO. Two floating electrodes, which have different potentials, were defined at the bottom of the Y-shaped channel. Floating electrodes and the designed channel were depicted in Figure 2.48 and Figure 2.49, respectively. Mixing efficiency of the system was evaluated according to floating electrode potential (Figure 2.50a), conductivities of the electrolytes against frequency of externally applied AC field (Figure 2.50b), phase shift between the external fields (Figure 2.50c) and type of AC signals which are sinus wave and square wave (Figure 2.50d). Simulations were validated using the experimental studies.

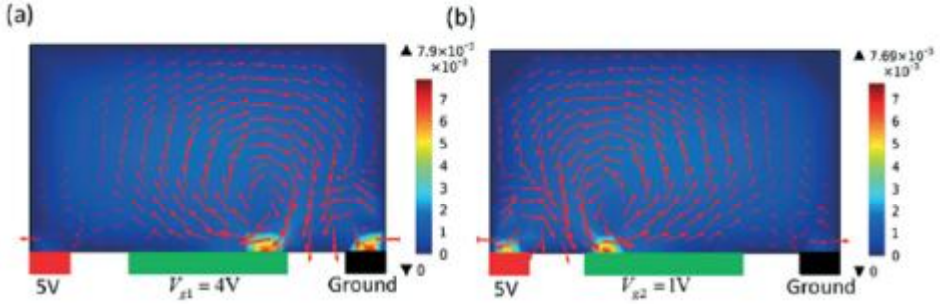

Figure 2.48. Asymmetrical vortices upon floating electrodes for (a) 4V fixed potential and (b) 1V fixed potential (Wu et al., 2017)

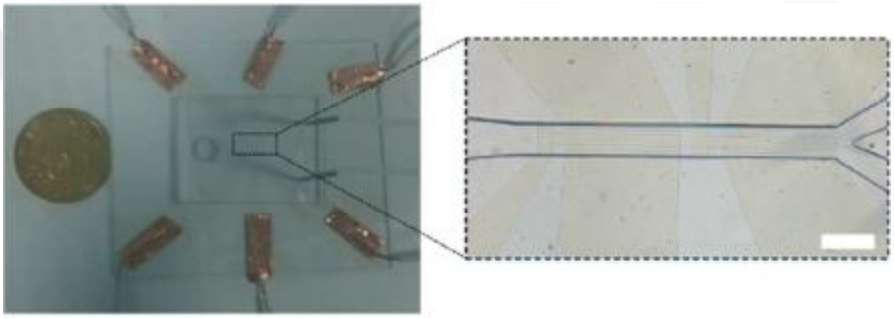

Figure 2.49. Microfabricated Y-shaped channel for fixed potential ICEO experiments (Wu et al., 2017)

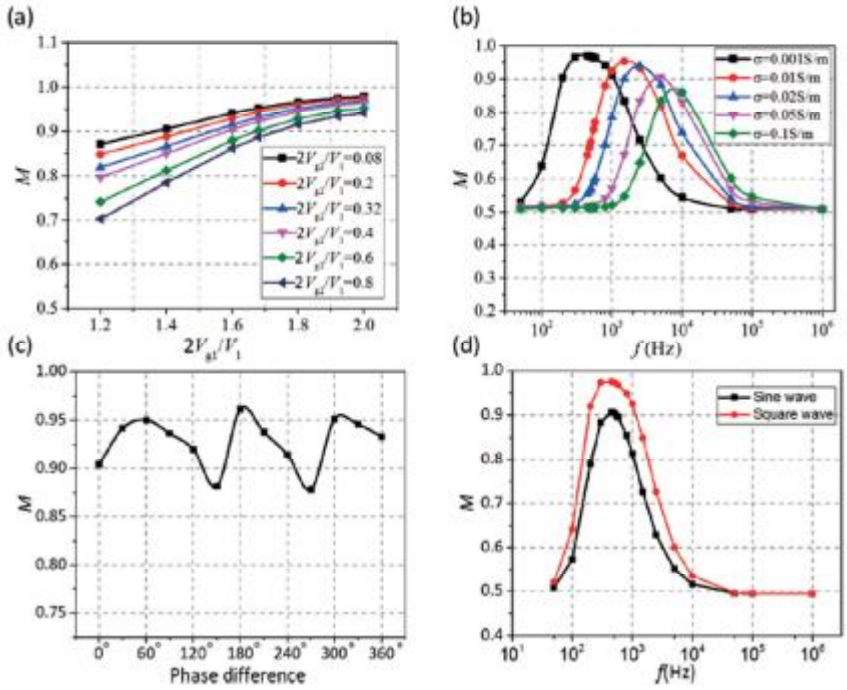

Figure 2.50. (a) Mixing efficiency under different ratios between the potential of first and second floating electrodes (V_1-V_2) and external potential (b) Mixing efficiency variations for electrolyte solutions which have different conductivities (c) Mixing efficiency for phase shifts between external electrodes (d) Mixing efficiency for the type of AC signal (Wu et al., 2017)

3. MATERIAL AND METHODS

Two-dimensional (2D) simulations are carried out with a finite element modeling (FEM) package, COMSOL Multiphysics 5.3a. A microchannel with a rectangular cross-section, whose dimensions are Width (W)=0.1mm x Length (L)=1mm is utilized for this study. A micro rectangular obstruction with various widths of W_c=0, 0.01, 0.02, 0.03, 0.04, 0.05 mm is employed to increase mixing efficiency. Two rectangular obstruction lengths of L_c=0.1mm and 0.2 mm are tested. The top side of the obstruction is also defined as floating ICEO electrode. The microchannel geometry along with key parameters is shown in Figure 3.1

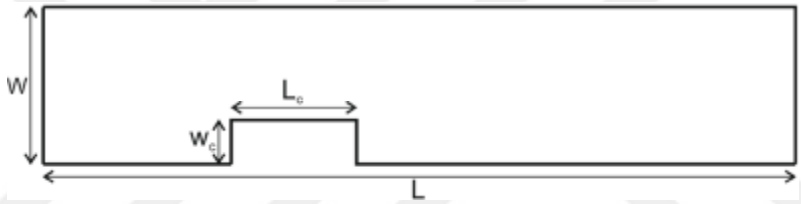

Figure 3.1. Designed microchannel geometry

Mesh independence test is performed for 6450, 13492, 21436 and 26676 triangular elements, consecutively. In addition, mesh density around the rectangular obstruction is refined to get a more precise solution. Same microchannel geometry and identical flow conditions are defined for every mesh density. A typical mesh distribution used in current simulations is shown in Figure 3.2. To be able to determine an optimal number of elements in mesh domain, maximum relative error in mixing index between successive mesh densities of 1% is chosen. Therefore, the mesh with 21436 elements is selected as an optimal mesh density and used in every simulation. Simulation duration is also determined using a similar approach. Durations of 10s and 20s are simulated successively for no obstruction and similar flow conditions. The relative error of average mixing index

at the outlet is under 0.2%. Thus t=10s is selected to decrease computational workload.

Another mesh independence analysis is carried out for non-Newtonian fluids, because of the mesh number is utilized for non-Newtonian case requires mesh structure different than that of Newtonian case. This can be attributed to the nonlinear flow equation for non-Newtonian fluids, which is derived from variable viscosity values. Simulations are performed in a straight microchannel with the mesh numbers of 21436, 29614, 34457 and 39593. Due to the relative error between 34457 and 39593 elements is below 1%; mesh with 34457 elements is used during the simulations as seen in Figure 3.3. Simulation duration is again determined as 10s because difference between average mixing index values of 10s and 20s are calculated as lower than 0.2%.

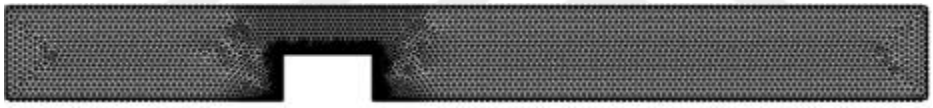

Figure 3.2. Mesh structure for Newtonian fluid

Figure 3.3. Mesh structure for non-Newtonian fluid

The fluids are assumed to be incompressible Newtonian and non-Newtonian for this study. Left and right ends are the inlet and outlet boundaries of the channel, respectively. Therefore, fluid flow is determined as from left to right in numerical simulations. The species, which are diluted in the fluids, are also identical and having same initial concentration value of C_0=10 mol/m^3. Two-step functions, which are defined oppositely to each other, are defined for separating the fluids as well as contained diluted species from the middle point of the inlet. The step functions are depicted in Figure 3.4.

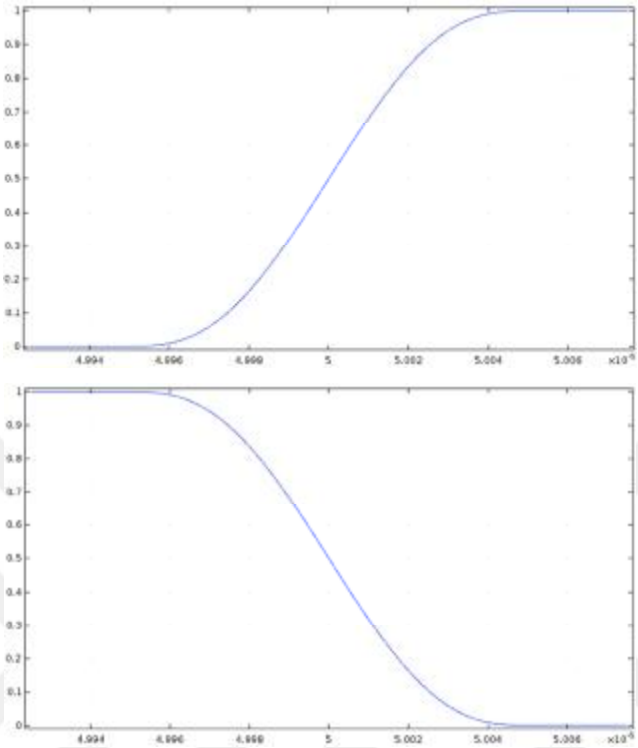

Figure 3.4. Oppositely defined step functions against channel width for separating the fluids at the inlet

The motion of the fluids is described by Navier – Stokes Equation and continuity equation, which are presented below, respectively.

$$\rho\left(\frac{\partial \boldsymbol{u}}{\partial t} + (\boldsymbol{u}.\nabla)\boldsymbol{u}\right) = -\nabla p + \nabla.(\eta\nabla^2\boldsymbol{u} - \frac{2}{3}\eta(\nabla.\mathbf{u})\mathbf{I}) + \boldsymbol{f}$$

$$\frac{\partial \rho}{\partial t} + \nabla.(\rho\boldsymbol{u}) = 0$$

where **u** and ρ is the velocity and the density of the fluid, respectively, p is the pressure, **f** is the body force, bold characters are preferred for indicating the vector quantity. Viscous forces and inertial forces are represented by the second term of the right-hand and the left-hand side of the equation, respectively. These

equations are modified due to the incompressibility of the fluid, i.e. density of the fluid remains constant on every point on the microchannel for each case.

$$\rho(\frac{\partial \boldsymbol{u}}{\partial t} + (\boldsymbol{u}.\nabla)\boldsymbol{u}) = -\nabla p + \eta\nabla^2\boldsymbol{u} + \boldsymbol{f}$$

$$\nabla.\boldsymbol{u} = 0$$

The fluids experience body force is evaluated according to the thickness of EDL, which is calculated by

$$\lambda_D = \kappa^{-1} = \sqrt{\frac{\varepsilon k_B T}{2e^2 z^2 n_\infty}}$$

where ε is the permittivity of the fluid, which equals to product of the permittivity of free space (ε_0) and permittivity of the fluid relative to free space (ε_r), k_B is the Boltzmann constant ($1.381x10^{-23}$), T is the temperature (293.15 °K), e is the elementary charge ($1,609x10^{-19}$ C), z is the ion valency (1), and n_∞ is the ionic number density for 0.001M ($=6.02x10^{-21}$ 1/L). For the symmetric binary electrolyte, which cations and anions have the same valency, EDL thickness is calculated less than 10 nm for 1mMol KCl. Due to the EDL thickness is quite lower than the width of the microchannel, infinitesimal thin EDL approximation can be conveniently adapted to our system. Because only the bulk solution, which incorporates zero net charge density (ρ_e), is modeled fluids experience no body force ($\boldsymbol{f} = \rho_e \boldsymbol{E}$).

Viscosity term in the Navier-Stokes Equation is a constant value for a Newtonian fluid. However, it depends on the shear rate for non-Newtonian fluids:

$$\mu = \mu(\dot{\gamma})$$

where γ represents the shear rate.

In this study, the viscosity of non-Newtonian fluids is described according to Power-law and Carreau models which are given below, respectively.

$$\mu = m\,\mu^{n-1}$$

$$\mu = \mu_{\infty} + (\mu_0 - \mu_{inf})[1 + (\lambda\dot{\gamma})^2]^{\frac{(n-1)}{2}}$$

where m is the flow consistency index for Power-law fluid. n is the common dimensionless parameter for both models which represents fluid behavior index. While n<1, the shear-thinning behavior is observed; shear-thickening behavior emerges when n>1. Otherwise, i.e. for the cases of n equals to 1, the Newtonian behavior is considered. For Carreau model, viscosity equation takes into account zero shear rate viscosity (μ_0) and infinite shear rate viscosity (μ_{inf}). In addition, λ is the relaxation time constant. Values for these parameters are obtained from the studies of Das and Chakraborty (2006) and Johnston et al. (2004) for Power-law and Carreau models, respectively.

Reynolds number is the ratio of inertial forces to viscous forces:

$$Re = \frac{\rho \boldsymbol{u} L}{\eta}$$

where L is the characteristic length scale of the microchannel, which is taken as the width of the microchannel. Therefore, Reynolds number is determined as 0.2 in the system, continuously. It can be concluded that viscous forces dominate inertial forces in the current flow environment.

The transport of diluted species is governed by Nernst – Planck Equation which is:

$$\frac{\partial C}{\partial t} + \nabla . \boldsymbol{N} = R$$

where C is the concentration of the species, R is the chemical reaction term and **N** is the total flux of mass transport which consist of diffusive and convective flux:

$$\boldsymbol{N} = -D_i \nabla C + C . \boldsymbol{u}$$

where D is the diffusivity coefficient of the species. If the total flux is substituted in Nernst-Planck Equation and no chemical reaction is considered, the last form of the equation is obtained:

$$\frac{\partial C}{\partial t} + (\boldsymbol{u} . \nabla) C = D \nabla^2 C$$

The aforementioned Péclet number is the ratio between this convective flux and diffusive flux:

$$Pe = \frac{C . \boldsymbol{u}}{D \nabla C}$$

In the case of relatively low diffusion coefficient, Péclet number is high, and convection rather than diffusion dominates mass transport.

Electroosmosis is another component of our design, which is explained by this means: Electrical potential distribution between the charged surface and the medium, by which electrolytes are suspended, is described by Poisson equation:

$$\varepsilon \nabla^2 \phi = \rho_e$$

where ε is the permittivity of the fluid which equals to the product of the permittivity of free space (ε_0) and permittivity of the fluid relative to free space (ε_r), ρ_e is the space charge density. Resulting potential distribution for a flat surface is demonstrated in Fig 3.5.

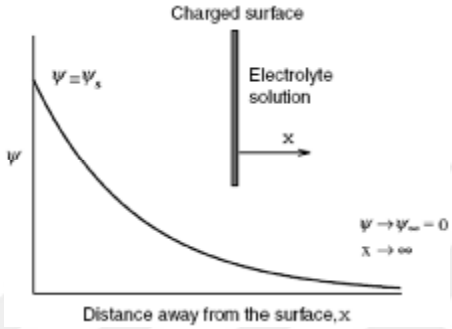

Figure 3.5. Electric potential distribution from the solid surface towards a bulk solution (Masliyah and Bhattarjee, 2008)

Due to thin EDL approximation, Laplace equation is solved instead of Poisson equation:

$$\varepsilon \nabla^2 \phi = 0$$

Thin EDL approximation also affects Dukhin number (Du), which is the ratio of surface conductivity to bulk conductivity (Crespy et al., 2006). In this study Du<<1 is constituted. Hence, the effect of the concentration gradient can be safely neglected. In ICEO, zeta potential possesses a constant value on the upper and lower walls, which can be calculated as:

$$\zeta_w = \frac{\rho_s}{\varepsilon_0 \varepsilon_r \kappa}$$

where ρ_s is the surface charge density of the material. In Debye-Hückel limit, i.e. zeta potential is smaller than 0,025V; EDL exponentially screens the surface potential:

$$\phi = \zeta_w e^{-\kappa z}$$

Electroosmotic flow velocity for channel walls is defined regarding fixed zeta potential and tangential component of the electrical field.

$$\boldsymbol{u}_{eo} = -\frac{\varepsilon_0 \varepsilon_r \zeta_w}{\mu} \boldsymbol{E}_t$$

which is well-known Smoluchowski slip velocity equation and ε_0 and ε_r are permittivities of free space and relative permittivity of the fluid, ζ_w is the zeta potential of the upper and lower walls, E_t is the tangential component of the externally applied electrical field, and μ is the fluid viscosity.

Plug-like flow profile is observed through conventional electroosmosis. In order to initiate mixing enhancement, a nonlinear electrokinetic phenomenon is introduced to the system: Induced-charge electroosmosis (ICEO). ICEO theory is explained for cylindrically shaped electrodes by Squires and Bazant (2004). When a conducting surface is placed into the medium with an external electrical field, electric field lines intersect conductor at right angles, which are illustrated in Fig 3.6a. In response to the applied field, free ions in the solution are dragged by a current ($\boldsymbol{J} = \sigma \boldsymbol{E}$) to either side of the conductor. Therefore, a dipolar surface charge is induced on the conducting surface. Amount of the opposite ions are equal with respect to charge conservation law. The induced EDL is formed around the induced charges. Equilibrium state is reached when no field lines penetrate the induced EDL as shown in Fig 3.6b. Fluid is driven from the poles of the particle to the equator by tangential component of the electrical field.

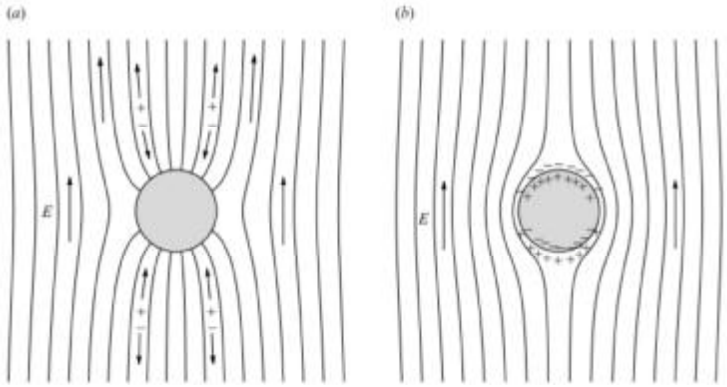

Figure 3.6. (a) Electrical field lines intersect conducting surface at right angles initially (b) Electrical field lines is expelled from the surface after the steady-state is constituted (Squires and Bazant, 2004)

Electric potential is formed by conducting surface at starting time of t=0, which equals to:

$$\phi_0 = -E_0 z(1 - \frac{a^2}{r^2})$$

where a is the radius of the cylinder. Equilibrium electrical potential on the conducting surface is given by

$$\phi_f = -E_0 z(1 + \frac{a^2}{r^2})$$

Then, the zeta potential of the conducting surface is expressed as

$$\zeta(\theta) = \phi_0 - \phi(a) = 2E_0 a cos\theta$$

In our study, an electrode is embedded upon the surface of micro rectangular obstruction and a direct current is applied externally across the channel, where the positive electrode is located at the inlet, and the outlet is grounded. As a result, a steady state ICEO flow is generated around a straight floating electrode.

The electric field can be calculated from externally applied electric potential, as **E**= -∇ ϕ. Under this electrical condition, the channel walls are assumed to be made of a non-polarizable material, thus **n**·σ∇ϕ =0, where **n** is the unit normal to the surface. EDL of the polarized surface can be modeled by three ways: Guoy's model ($C_D = \varepsilon/\lambda$), Stern's model ($\delta = C_D/C_S$) and empiric model ($Z(w) \propto (i\omega)^{-\beta}$) which is shown in Figure 3.7 (Levitan et al., 2005).

Figure 3.7. EDL of (a) Guoy's model which consists of a capacitance (b) Stern's model which consist of series capacitors (c) empirical model (Levitan et al., 2005)

For capacitor models, the electrical boundary condition of the conducting surface, which incorporates bulk current and the EDL capacitive charging is

$$\sigma \mathbf{n} \cdot \nabla \phi = C_D \frac{d\zeta}{dt}$$

σ represents the bulk conductivity and defined as $\sigma=\varepsilon D/\lambda^2$. Diffuse layer capacitance is denoted as C_D and defined as $C_D=\varepsilon/\lambda$.

For Stern model, the induced zeta potential on the conducting surface is defined as

$$\zeta = \frac{\phi_0 - \phi}{1 + \delta}$$

where ϕ_0 is electric potential across floating electrodes and $\delta = C_D / C_S$ and C_s is Stern layer capacitance. As a result, the tangential component of fluid velocity over floating electrodes is

$$\mathbf{u}_t = \frac{\varepsilon\zeta}{\mu}\nabla_t\phi$$

Fluid streamlines, which show two identical counter-rotating vortices due to ICEO solely is shown in Fig 3.8.

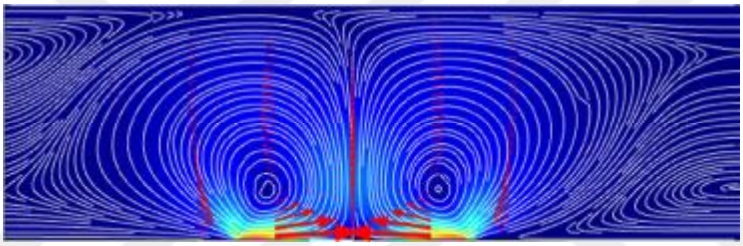

Figure 3.8. Counter-rotating identical vortices which derive from ICEO

Externally applied potential differences are selected within a widespan. Electroosmotic flow velocity and induced zeta potential values are also varied, which is dependent on alterations in the external potential difference. The potential differences of V=10V, 20V, 30V, 35V, 40V, 45V, and 50V are tested and the selection is made based on the ratio between maximum pulsatile velocity magnitude and total steady velocity magnitude. Electroosmotic velocity contributes steady velocity, thus, increasing this potential difference leads to suppression in the pulsatile flow regime, whereas species transport is attenuated by decreasing it. As a result, the V=20V, 30V and 40V potential differences, which correspond to the ratios of 0.32, 0.41 and 0.51 are selected as external electrode potential for current micromixer design, respectively.

The last component of the design, which is pulsatile flow is introduced by defining a sinusoidal time-dependent equation to the inlet of the channel:

$$U = U_s + U_m \sin(2\pi f t)$$

where U_m and U_s represent maximum pulsatile velocity value and time-independent laminar velocity value, respectively. Steady laminar flow is superimposed upon the oscillating flow, as shown in Fig 3.7, which is an obligation for this study. Unless this steady flow expression is included in this equation, transporting of diluted species until the outlet becomes inadequate. In addition, the phase shift between defined pulsatile flows is defined as zero. Velocity distribution at the inlet of the channel due to pulsatile flow is shown in Fig 3.9. As a result, the fluids are accelerated through the channel by three different mechanisms, which are pulsatile flow, steady laminar flow, and electroosmotic flow. Navier – Stokes and Nernst – Planck Equations are coupled with same **u** quantity, which consists of the superposition of these different flow driving mechanisms:

$$\boldsymbol{u} = \boldsymbol{u}_{pulsatile} + \boldsymbol{u}_{laminar} + \boldsymbol{u}_{eo}$$

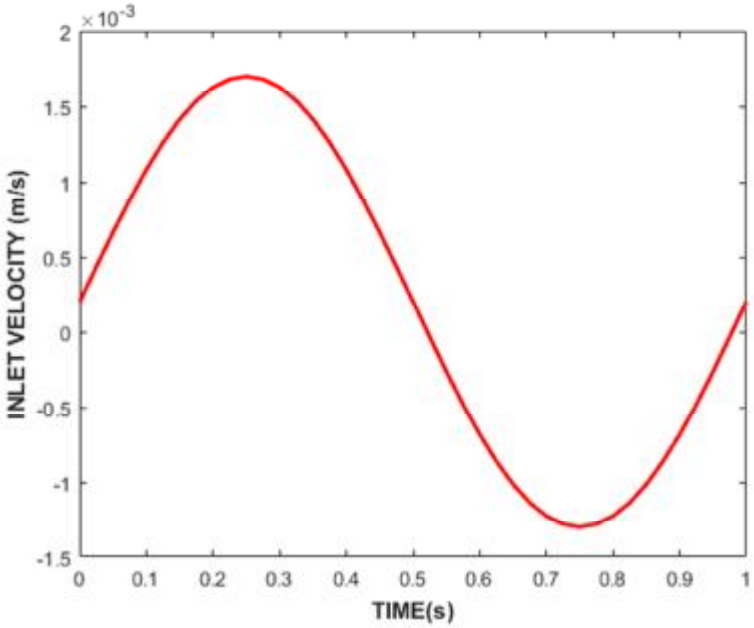

Figure 3.9. Inlet velocity profile

The behavior of the system with different pulsation frequencies is also concerned, which is quantified by Strouhal number:

$$St = \frac{fL}{\boldsymbol{u}}$$

Initially, all simulations are carried out with f=1 Hz frequency. To investigate the effect of frequency of flow pulsation, various frequency magnitudes of f=0.5Hz, 1.5Hz and 2Hz are applied to single channel geometry, which contains floating electrode with L_c=0.1mm for different obstruction widths. All parameters are quantitatively listed in Table 2.1.

Table 3.1. Key parameters used in simulations

PARAMETER	DEFINITION	VALUE
ε_0	The permittivity of free space	8.854×10^{-12} F/m
ε_r	The relative permittivity of the Newtonian (non-Newtonian) fluid	80 (59.86)
ρ	Density of the Newtonian (non-Newtonian) fluid	998 kg/m^3 (1060 kg/m^3)
μ	Viscosity of the Newtonian fluid	1×10^{-3} Pa.s
D	Diffusivity of the diluted species for Newtonian (non-Newtonian) fluid	1×10^{-10} m^2/s (1.38×10^{-10} m^2/s)
C_0	The initial concentration of diluted species	10 moles/m^3
U_m	Maximum pulsatile flow velocity	1.5 mm/s
U_s	Pressure-driven flow velocity	0.2 mm/s
Van	External electrical potential difference	20V – 30V – 40V
f	Frequency of pulsatile flow	0.5Hz-1Hz-1.5Hz-2Hz
n	Fluid behavior index for Power-law (Carreau) models	0.785 (0.3568)
m	Flow consistency index for Power-law	0.0134 kg/m.s
μ_0	Zero shear rate viscosity for Carreau	0.056 Pa.s
μ_{inf}	Infinite shear rate viscosity for Carreau	0.0035 Pa.s
λ	Relaxation time constant for Carreau	3.313s

Since all results are obtained, performances of the different parameter combinations are evaluated according to mixing index, which is calculated as:

$$Mixing\ Index = \left(1 - \frac{\int_0^W |\ C - C_\infty| dy}{\int_0^W |\ C_0 - C_\infty| dy}\right) \times \%100$$

where C is the concentration of the diluted species for any cross-sectional plane through the channel, which is selected as outlet during calculations, C_∞ is the perfect mixing concentration value, which corresponds to 5 moles/m^3 for this study, and C_0 is the no mixing concentration, which corresponds to 0 or 10 moles/m^3.

4. RESULTS AND DISCUSSIONS

In this study, mixing performance is evaluated under the mechanisms of pulsatile flow and ICEO. Initially, pulsatile flow and ICEO are separately applied to micromixer designs. It is observed that transport of diluted species is inadequate for both solely pulsatile and electrokinetic flows. Maximum concentration is not able to reach to the outlet of the channel even in the last period of pulsation, which is shown in Figure 4.1. This is also utilized as a model validation study. The resulting solution is consistent with theoretical knowledge using pushing (flow is directed to the positive x-axis) and pulling the fluids (flow is directed to the negative x-axis), consecutively. Transport of diluted species to the outlet is provided by introducing steady laminar flow to the pulsation. Thus, pushing stage of the pulsatile flow is rendered longer than pulling stage. Even though the half of the maximum velocity of pulsatile flow is defined as laminar flow velocity (V_0=0.75 mm/s), only 23% of mixing performance is achieved through this system. Concentration throughout the channel is shown for this configuration in Figure 4.2. Higher velocity values for steady flow are avoided for preventing the suppression of pulsatile flow. Therefore, rectangular obstructions are embedded in the lower wall of the channel. Again, low mixing performance of 26.58% is obtained under same conditions, as shown in Figure 4.3 which agrees with the computational study of Wang et al., (2008). When ICEO is attached to the design, efficient mixing is obtained with the disturbance of flow field within the cross-section of the microchannel. The magnitude of the electrical field, as well as width and length of ICEO electrode, is varied for investigating the behavior of mixing efficiency of the system.

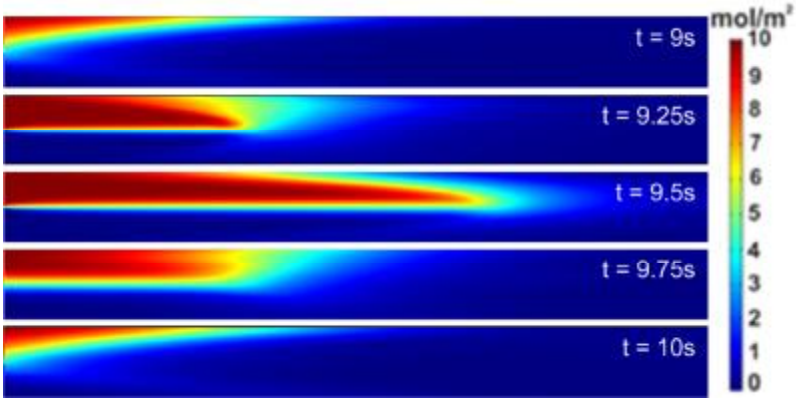

Figure 4.1. Concentration distribution for solely pulsatile flow

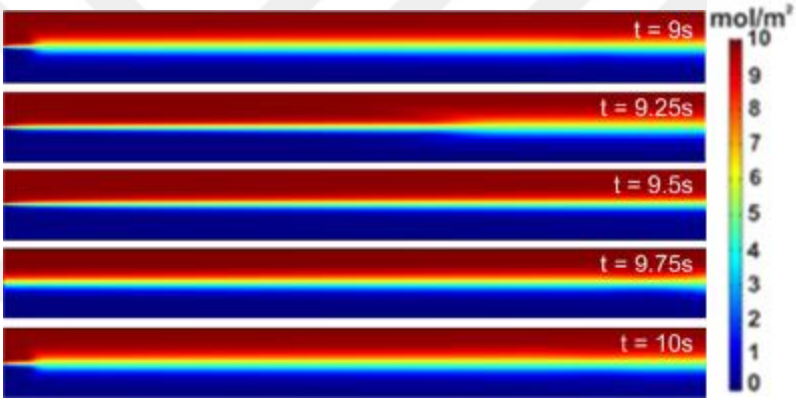

Figure 4.2. Concentration distribution for steady flow superimposed pulsatile flow

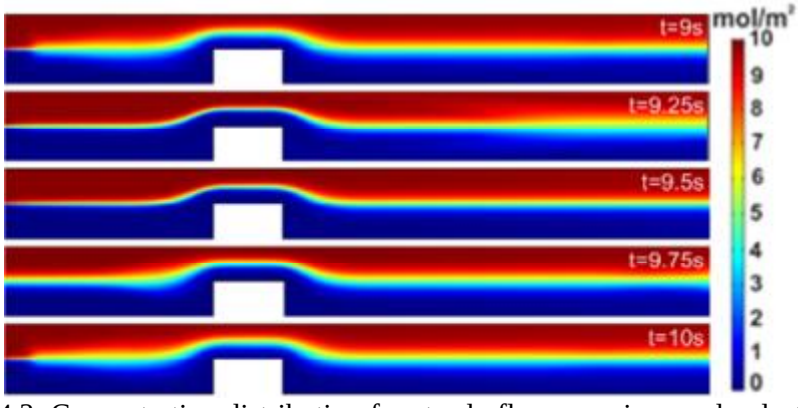

Figure 4.3. Concentration distribution for steady flow superimposed pulsatile flow in which case of microobstructed geometry

Distribution of streamlines and concentration of diluted species for V=20V, 30V and 40V are illustrated in Figure 4.4, Figure4.5 Figure 4.6, Figure 4.7, Figure 4.8, Figure 4.9, Figure 4.12 respectively. Velocity and concentration figures, which visualize same potential differences, are divided into three parts for better understanding. Results are presented for the last period of pulsatile flow with the time step of t=0.25s. The magnitude of fluid velocity and species concentration are described with color bars, which stand next to the relevant figures. Flow directions of the fluid streams are effectively manipulated with the vortices; thus, mixing becomes possible. These vortices, however, are smaller in size compared to pure ICEO, which arises from the suppression of the pulsation and the steady flow. Moreover, straightening of the shape of the vortex is observed for the time steps of t=9.25 and t=9.75, which can be seen in Figure 4.4a. At highest velocity value of positive pulsation, vortex on the left-hand side is suppressed for applied potential difference of V=20V. As correspondence, vortex on the right-hand side is suppressed at t=9.75s, which holds the highest velocity value of negative pulsation. Due to ICEO electrode is defined along the obstruction boundary, characteristics of vortices can significantly be altered by adding obstruction to the flow field. Therefore, ICEO electrode is enlarged in size around the obstruction, which paves the way for preventing the disappearance of vortices. Therefore, stronger vortices are generated for a microchannel with certain obstruction level with V=20V potential differences. Thus the vortices are not suppressed due to the pressure-driven flow regimes. Similarly, the vortices are never suppressed for V=30V and V=40V, which can be seen in Figures 4.7, 4.8, 4.9, 4.10, 4.11, 4.12. The strength of the vortices is higher for larger obstructions. This behavior of the system can be theoretically attributed to ICEO velocity, which increases with external potential and electrode size proportionally.

Transport of diluted species is observed as analogous to all potential differences. Outlet concentration is enhanced for W_c=0.01mm (Figure 4.4d, Figure 4.7d, Figure 4.10d) in comparison with zero obstruction (Figure 4.4b, Figure 4.7b.

Figure 4.10b). Even more concentration is transported for W_c=0.02mm (Figure 4.5b, Figure 4.8b. Figure 4.11b). However, transport of diluted species is attenuated for W_c=0.03mm (Figure 4.5d, Figure 4.8d, Figure 4.11d). This can be explained by the increase in channel blockage. On the other hand, transport of diluted species is significantly increased for W_c=0.04mm (Figure 4.6b, Figure 4.9b, Figure 4.12b). Increase in concentration with higher obstruction can be attributed to pressure drop according to the references of Sahu et al., (2013) and Syham et al. (2018). However, transport of diluted species is decreased by more increase in pressure drop as well as more blockage for W_c=0.05mm (Figure 4.6b, Figure 4.9b, Figure 4.12b)

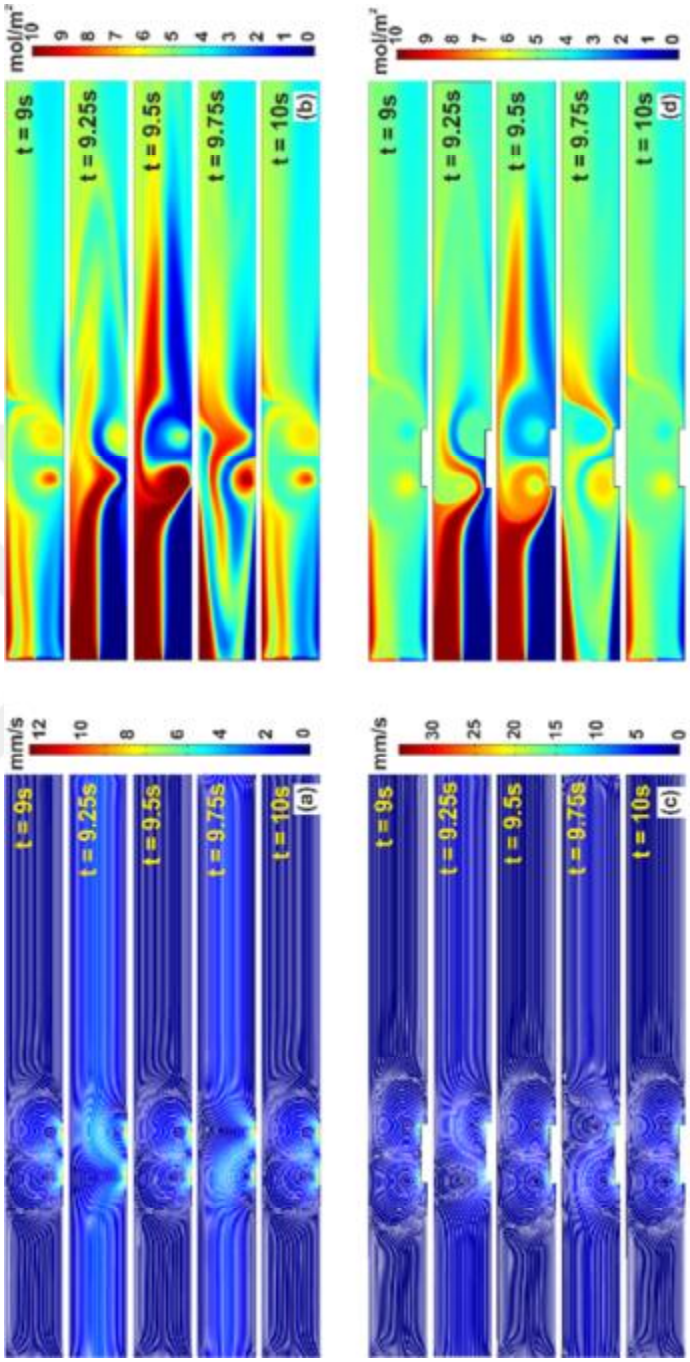

Figure 4.4. Velocity and concentration distributions for zero and 0.01mm microobstruction widths with a 20V potential difference

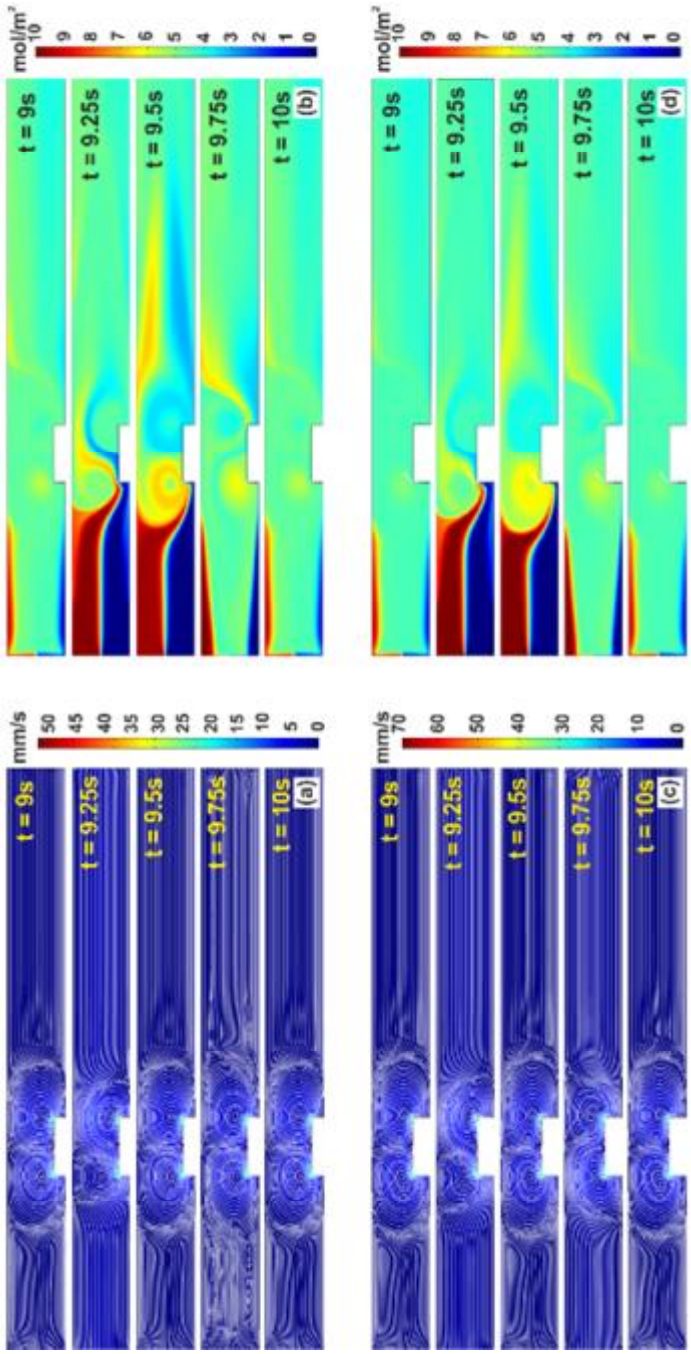

Figure 4.5. Velocity and concentration distributions for 0.02mm and 0.03mm microobstruction widths with a 20V potential difference

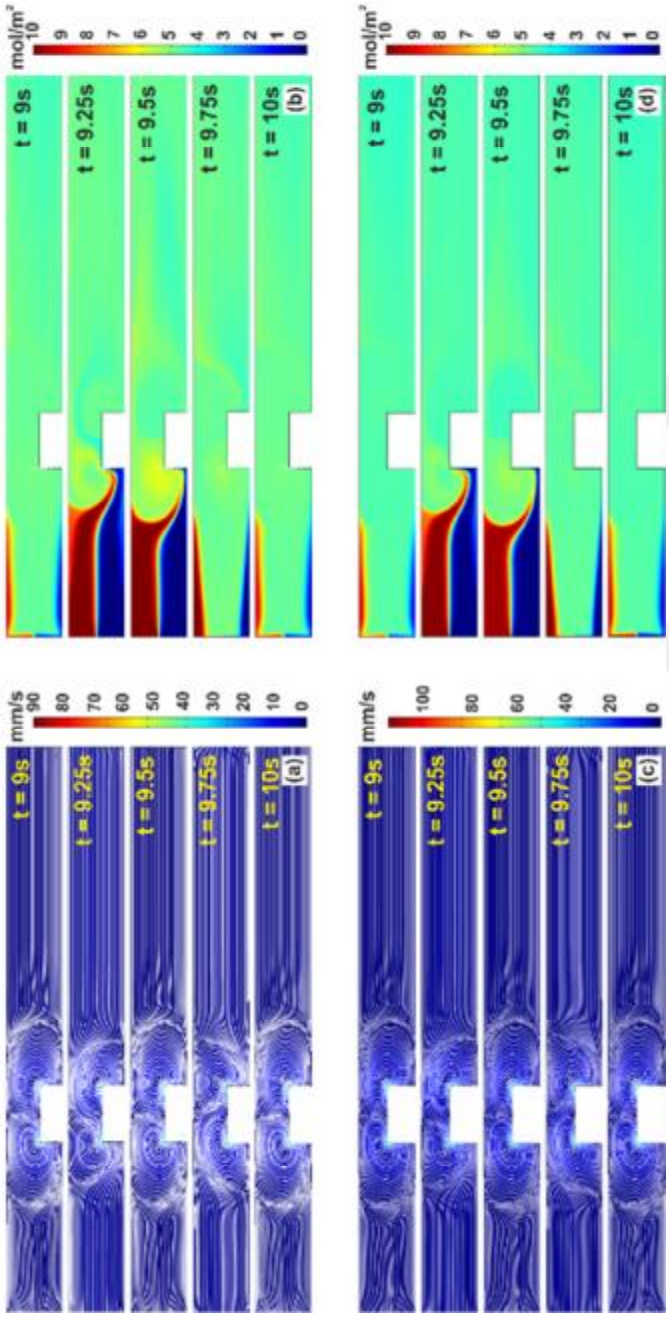

Figure 4.6. Velocity and concentration distributions for 0.04mm and 0.05mm microobstruction widths with a 20V potential difference

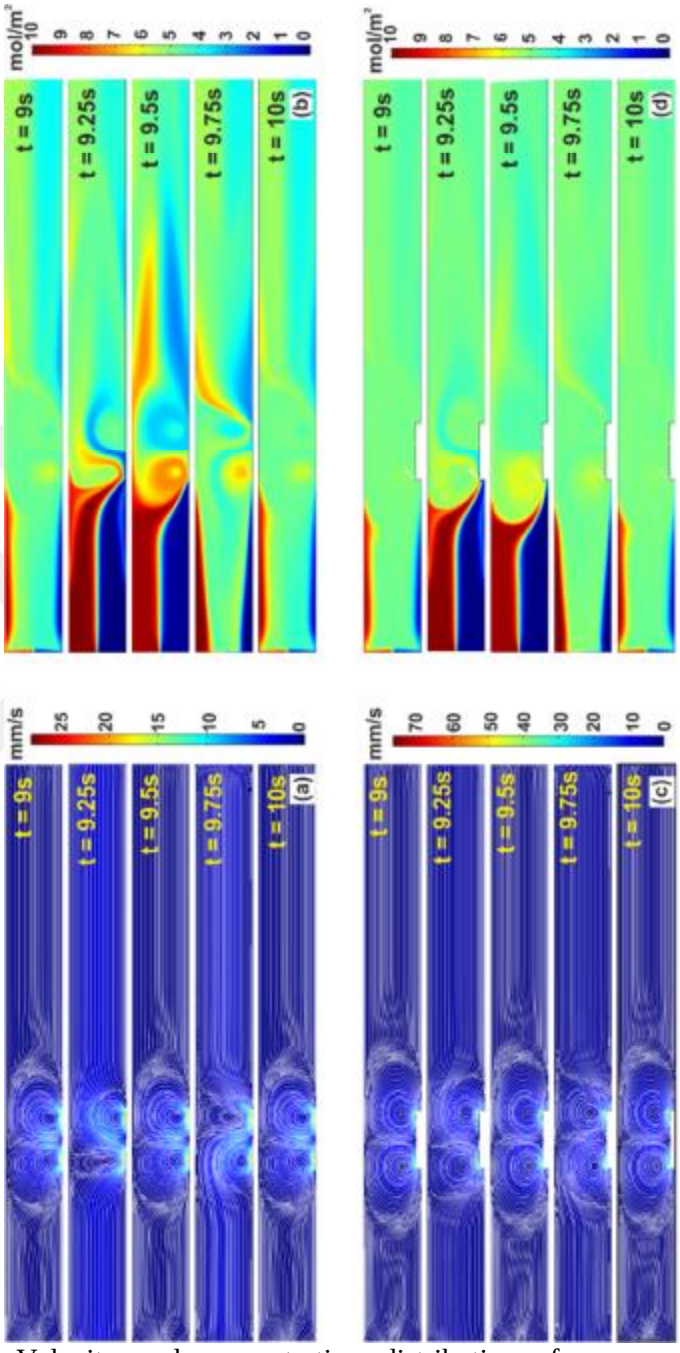

Figure 4.7. Velocity and concentration distributions for zero and 0.01mm microobstruction widths with a 30V potential difference

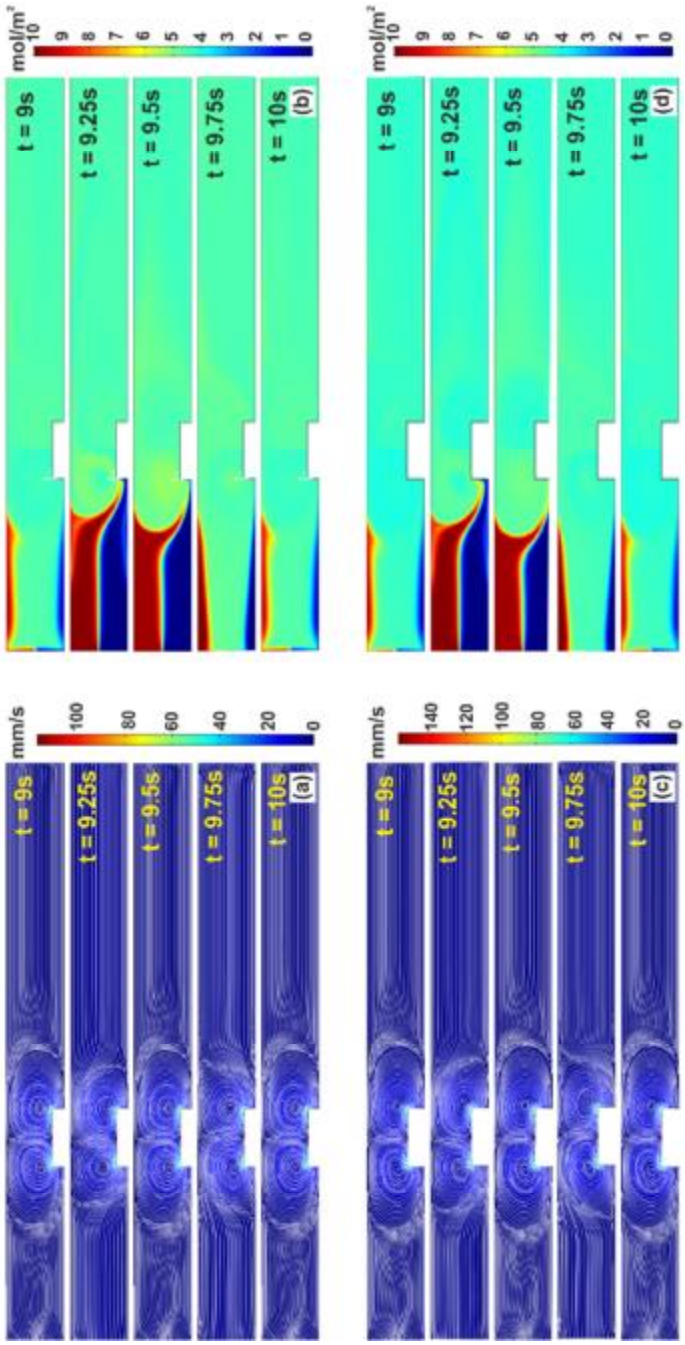

Figure 4.8. Velocity and concentration distributions for 0.02mm and 0.03mm microobstruction widths with a 30V potential difference

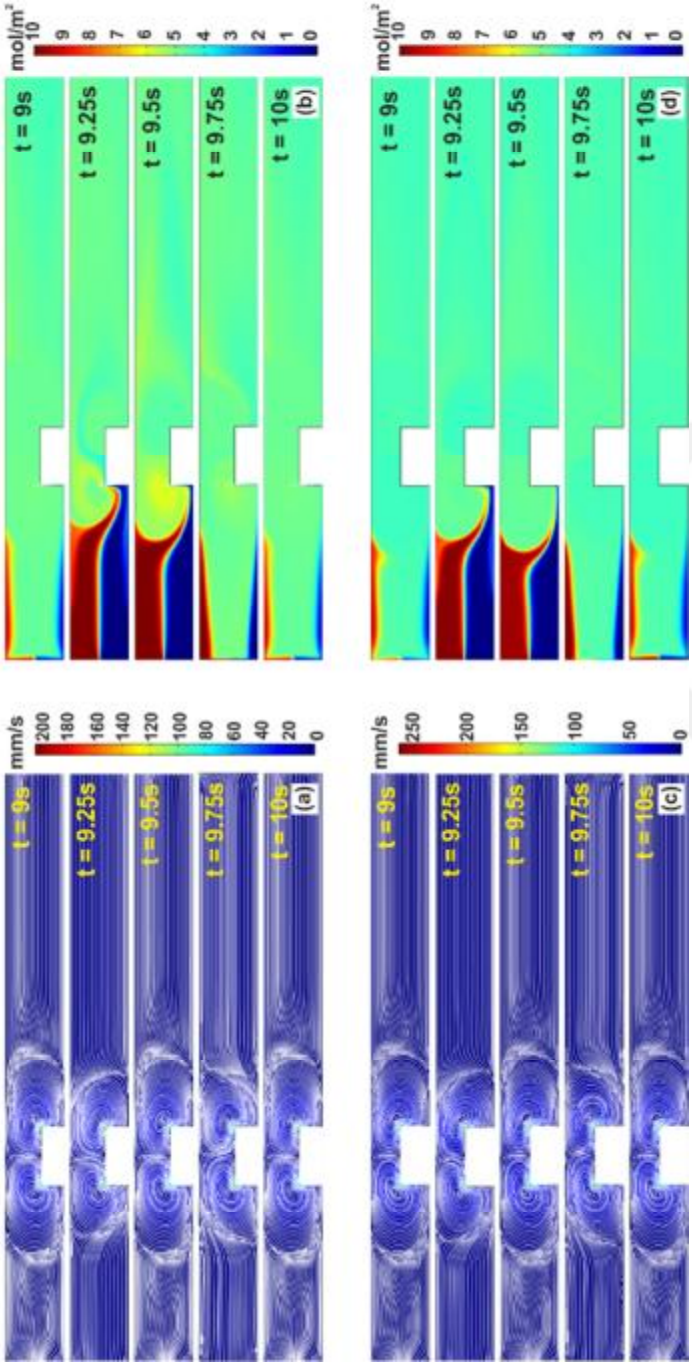

Figure 4.9. Velocity and concentration distributions for 0.04mm and 0.05mm microobstruction widths with a 30V potential difference

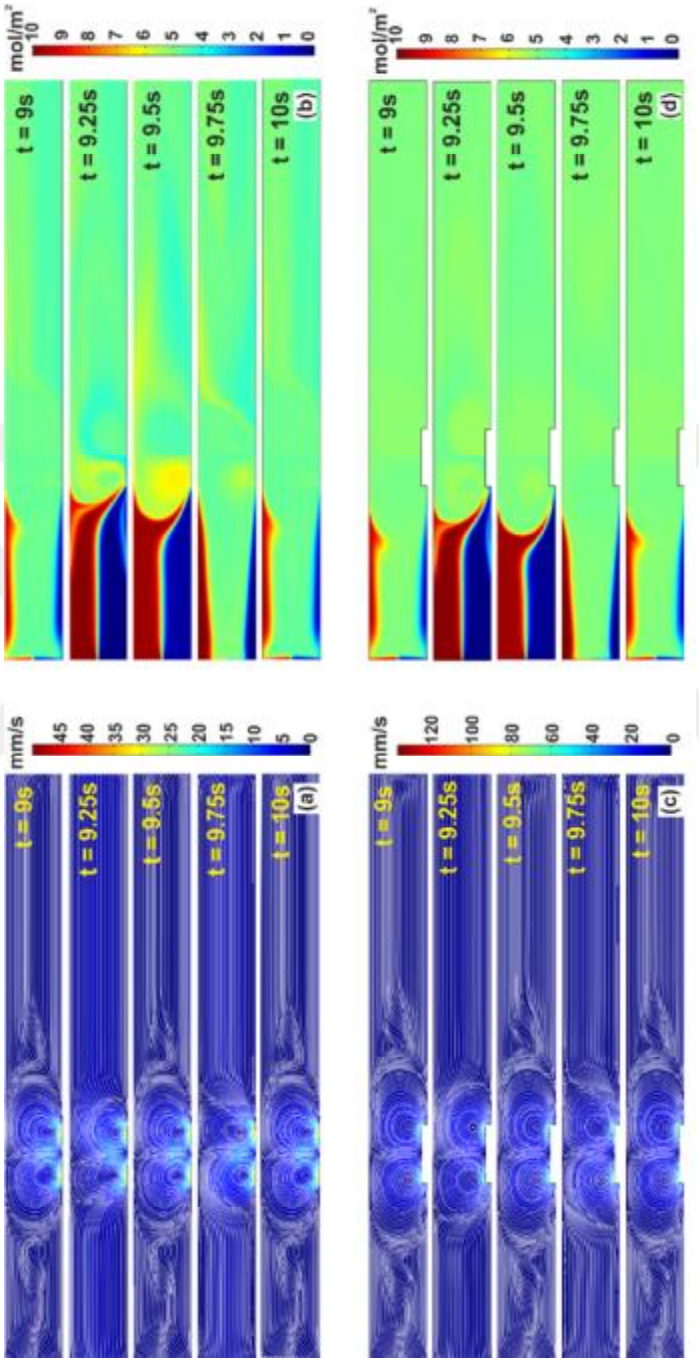

Figure 4.10. Velocity and concentration distributions for zero and 0.01mm microobstruction widths with a 40V potential difference

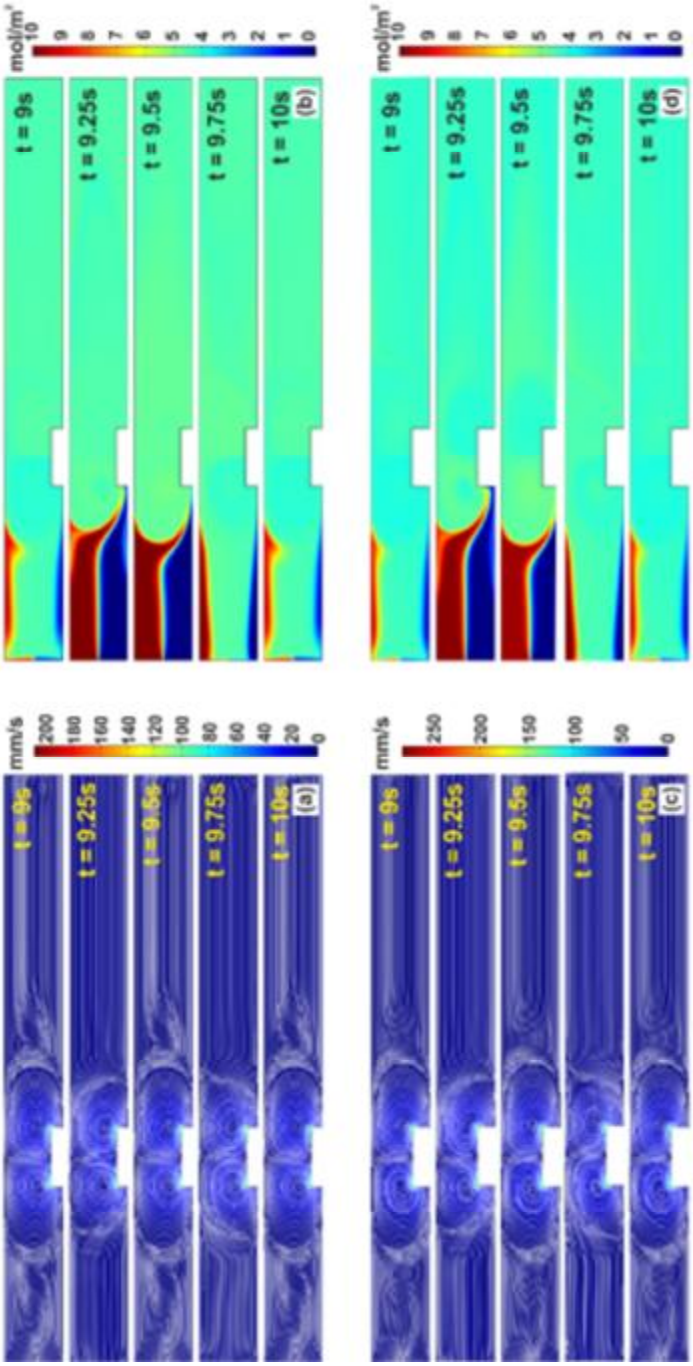

Figure 4.11. Velocity and concentration distributions for 0.02mm and 0.03mm microobstruction widths with a 40V potential difference

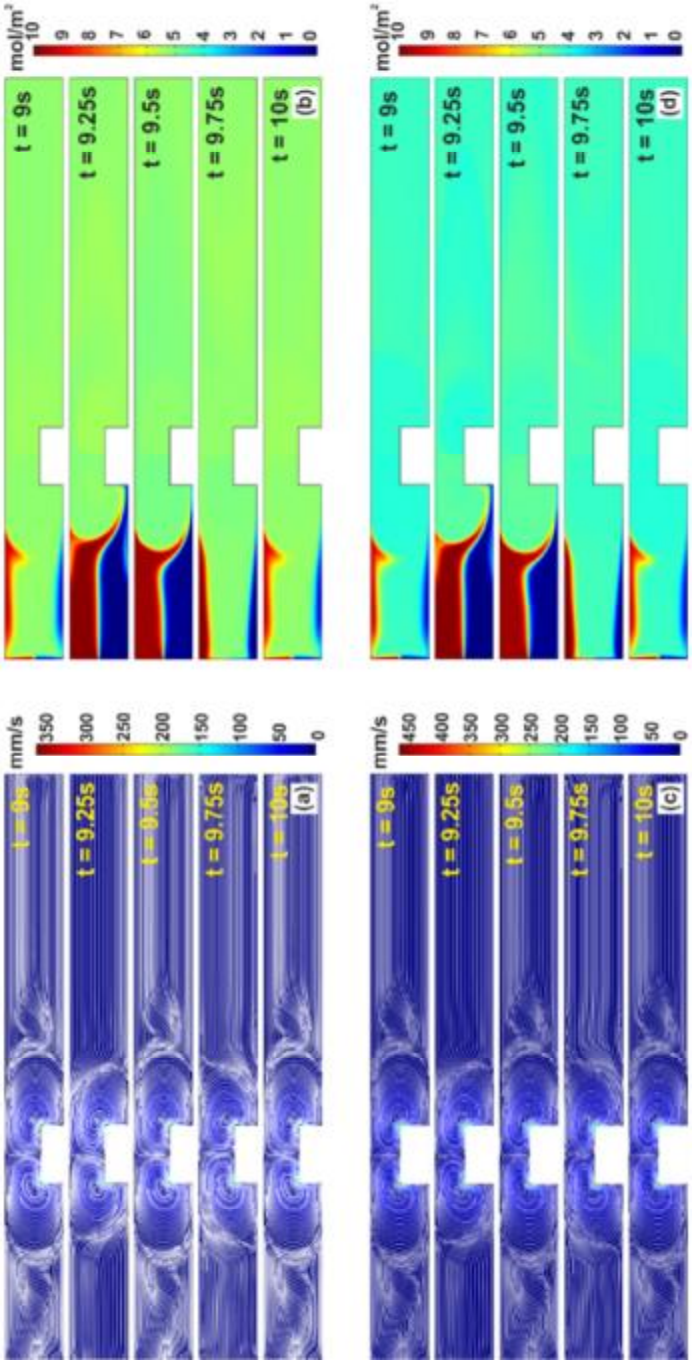

Figure 4.11. Velocity and concentration distributions for 0.04mm and 0.05mm microobstruction widths with a 40V potential difference

Mixing index distributions for the last period is depicted in Figure 4.13 with every obstruction widths, which are W_c=0mm, 0.01mm, 0.02mm, 0.03mm, 0.04mm, 0.05mm, respectively. Mixing index values exhibit fluctuations, which originate from pulsation. On the contrary, mixing index values are more stable for the case of V=40V. This can be explained by velocity magnitude and size of vortices, which is higher for V=40V. These fluctuations are attenuated by strengthening vortices via adding an obstruction for the case of W_c=0.01mm. For W_c=0.02mm, mixing dependence to voltage is significantly diminished, which can be understood from closer mixing index values of V=30V and V=40V. Higher mixing index values are reached at V=20V. It is observed that mixing index values are decreased for the obstruction width of W_c=0.03mm. As mentioned earlier transport of diluted species is blocked by increasing obstruction width and applied voltage, which causes to diminish in mixing performance of the system. After that, an increase in mixing performance is observed for W_c=0.04mm. This situation can be explained by increasing pressure drop, which enables higher rates of species transport with the references of Sahu et al., (2013) and Syham et al. (2018). However, transport of diluted species is decreased by more increase in pressure drop as well as more blockage for W_c=0.05mm, which results in a decrease in mixing indexes.

Mixing index distributions are compared for short (L_c=0.1mm) and long electrode (L_c=0.2mm) as seen in Figure 4.14. For longer electrode, mixing indexes are radically altered, and different voltages exhibit more consistent mixing indexes. Better mixing performance is obtained compared to same voltage in short electrode. As an example, lowest mixing performance is obtained by V=10V in short electrode case, whereas one of the highest mixing indexes is observed for V=10V in the long electrode case. Mixing performance of the system is attenuated with a certain voltage magnitude, which is referred as the critical value. In short electrode, the critical magnitude is V=30V, whereas, it is identified as V=35V for long electrode configuration. Therefore, it can be concluded that either relatively

higher voltage can obtain enhanced mixing with low electrode length or lower voltage with high electrode length.

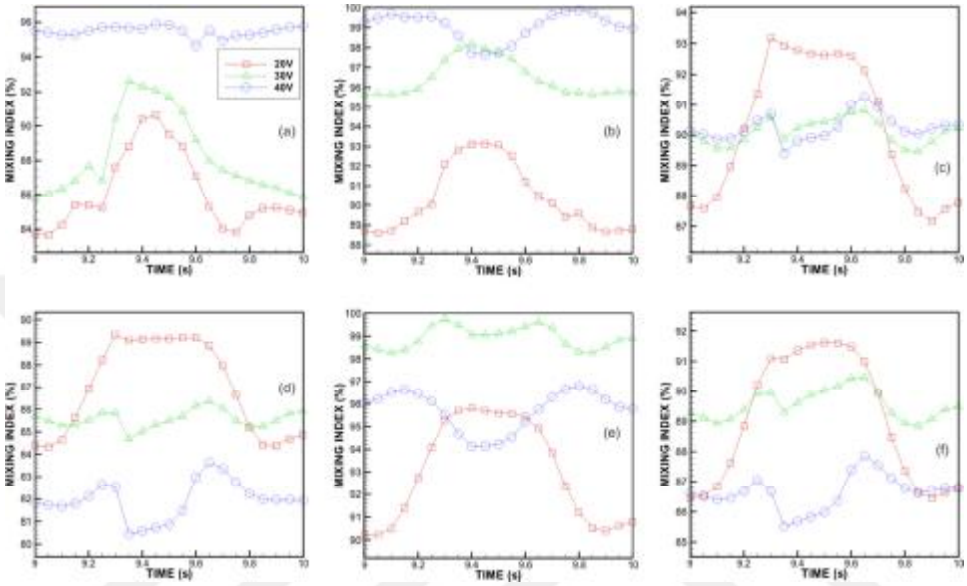

Figure 4.13. Concentration distribution at the outlet of microchannel for (a) no obstruction (b) W=0.01mm (c) W=0.02mm (d) W=0.03mm (e) W=0.04mm (f) W=0.05mm

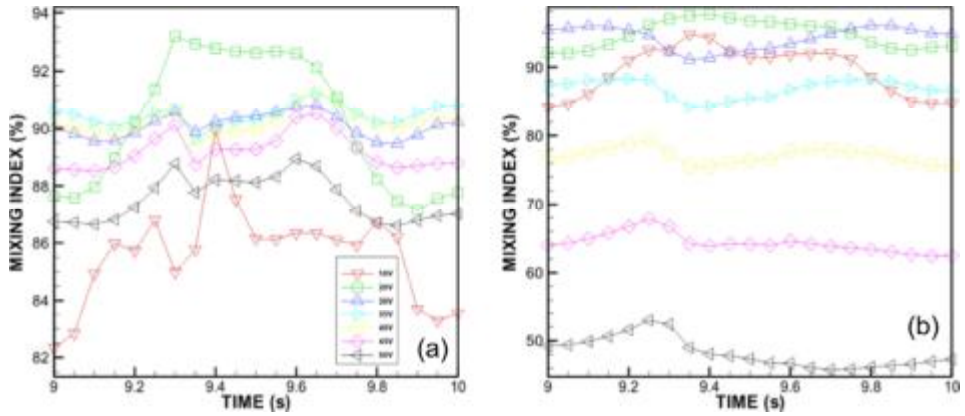

Figure 4.14. Mixing index values for (a) short and (b) long electrode configurations according to various potential differences

Mixing performance is also observed using the averages of mixing index values. Average mixing indexes are depicted in Figure 4.15 for the case of L_c=0.1mm. Average mixing index is relatively low for V=20V potential difference which is 86%. This can be explained by the disappearance of vortices at specific timescales. The highest mixing index is acquired for the V=40V potential difference in the channel geometry. All mixing indexes are increased with the presence of the obstruction. The highest increase among mixing indexes is obtained for V=40V, which contains the highest perturbation in the flow field. For W_c=0.02mm, mixing indexes are attenuated for V=30V and V=40V, wheras opposite trend is observed for V=20V. Mixing indexes are calculated as approximately equal for this obstruction width. All mixing indexes are decreased to the minimum point for the case of W_c=0.03mm, which is explained by lower transport of diluted species due to the high channel blockage. The decrease in mixing index, which is experienced by V=20V is the lowest and the highest is for V=40V. It is concluded that species can be transported better with lower ICEO velocity. Mixing index is increased for W_c=0.04mm. Higher pressure drop is observed with increased blockage; thus, higher concentrations of diluted species are accumulated at the outlet. However, mixing performance is attenuated by more increase in pressure drop as well as for more blockage, W_c=0.05mm.

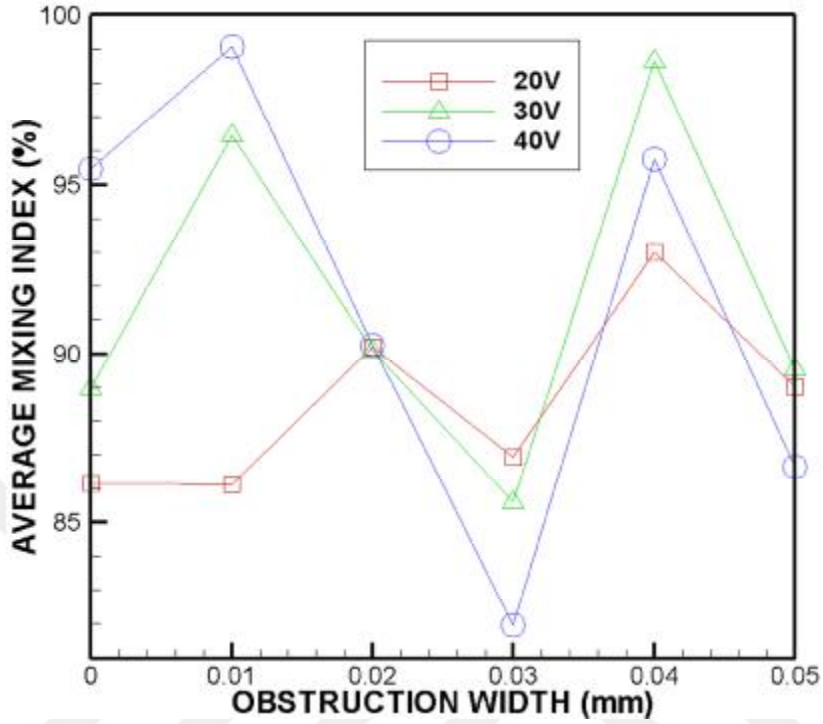

Figure 4.15. Periodic average mixing index values for every obstruction widths

Frequency dependence of mixing index is also investigated. Mixing index is significantly attenuated by which increasing the Strouhal number. This attenuation is quantified in Figure 4.16. The higher difference among mixing indexes is observed for various obstruction widths at low Strouhal numbers relative to high Strouhal numbers. For no obstructed channel, mixing index pattern is formed as for an increase in first step and decrease in the following steps which agrees well with the numerical study of Afzal and Kim (2015). The reason behind the decrease in higher Strouhal numbers is explained according to the transport of diluted species. When the frequency of the pulsation increases, diluted species have less time for convective transport and mixing index calculation is strongly dependent on concentration amount at the outlet. After f=2Hz, further simulations are considered as unnecessary due to the vast amount of concentration decrease at the outlet.

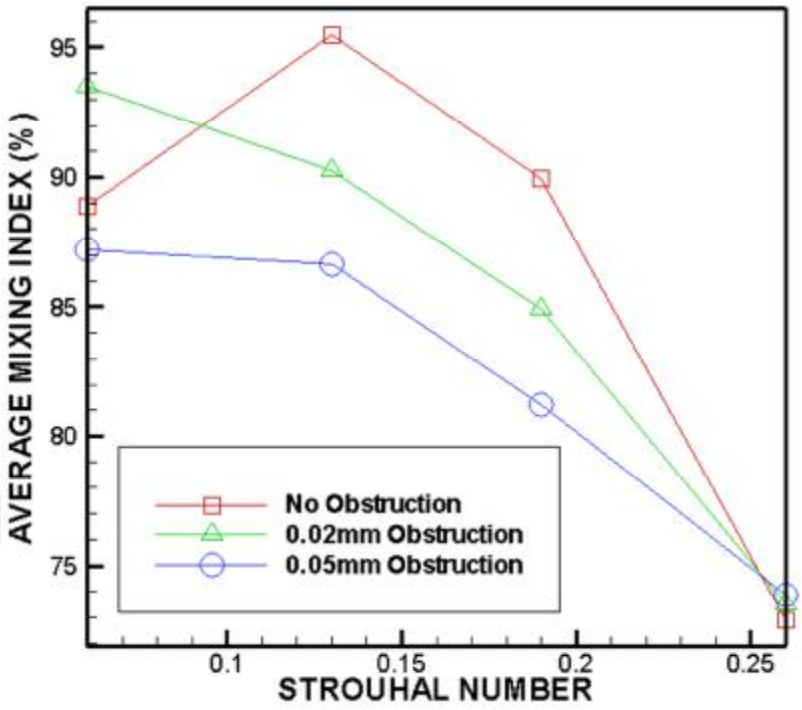

Figure 4.16. Average mixing index value against Strouhal number for various obstruction widths

Vorticity is the sign of rotation of the fluid. Vorticity patterns are compared for no obstruction and the highest obstruction with the electrode length of L_c=0.1mm and a potential difference of V=40V as seen in Figure 4.17. Vorticity magnitudes are illustrated by the color bars, which are located next to the figures. Positive vorticity is defined as the counterclockwise rotation of the fluid, which is demonstrated using red color and negative vorticity is defined as the clockwise rotation of the fluid, which is represented by blue color, correspondingly. Patterns of vorticity are observed only around the floating electrodes where ICEO flow occurs. The concentration of the vorticity is denser adjacent to the floating electrode. When the width of the obstruction is increased, vorticity also increases. This situation can be attributed to electrode size which gives in rise to stronger vortices.

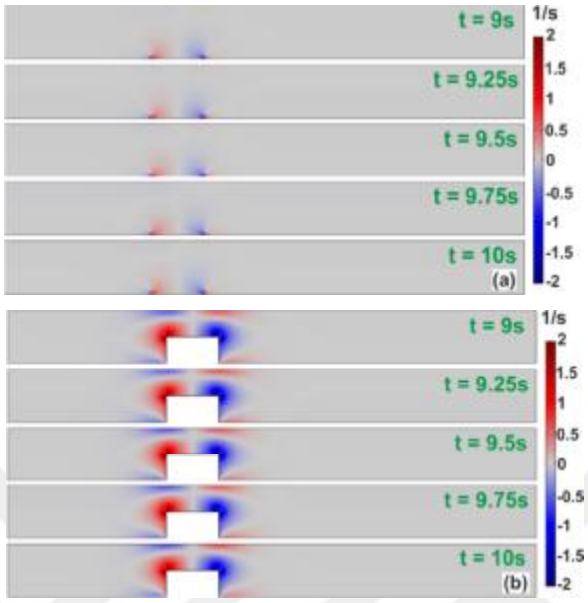

Figure 4.17. Vorticity patterns for (a) no obstruction (b) highest obstruction width with a potential difference of 40V

In the second part of the study, fluid nature is determined as non-Newtonian and same parameters are investigated under same flow conditions and microchannel geometry. Simulations are initially conducted with the only pulsatile flow. Due to the insufficient transport of diluted species, mixing application cannot be carried out as seen in Figure 4.18. Therefore, steady laminar flow, which has V_0=0.75 mm/s, is imposed on the pulsatile flow. Although sufficient transport of diluted species is achieved only 26.48% of mixing efficiency is obtained for power-law-type fluid as illustrated in Figure 4.19. Mixing efficiency increases up to 27.62% by adding microobstructions to the system. However, this increment is evaluated as quite low. In order to reach acceptable mixing efficiencies, ICEO is introduced to the system. These findings are consistent with the Newtonian fluid case.

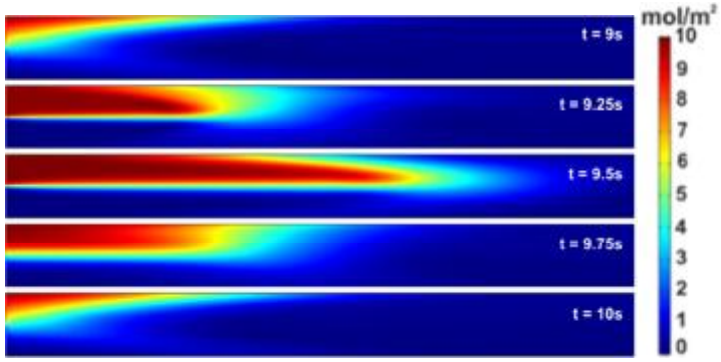

Figure 4.18. Concentration profile for solely pulsatile flow for power-law fluid

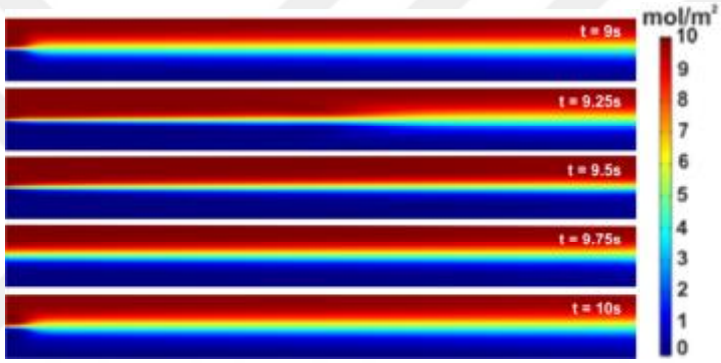

Figure 4.19. Concentration profile for steady laminar flow imposed pulsatile flow for a power-law fluid

The results of power-law and Carreau fluids are compared with Newtonian results. It is worth to note that the variation among the results of power-law and Carreau fluids are negligibly small. Therefore, non-Newtonian fluids are not mentioned as power-law and Carreau separately during the comparisons with a Newtonian fluid. Moreover, it is proven that blood can be safely modeled with either power-law or Carreau models for the given parameters in this study. Because the magnitudes of blood available in the literature are used in these models.

Simulations are mainly conducted with V=40V of potential difference and f=1Hz of pulsation frequency. Velocity and concentration distributions under these circumstances are illustrated in Figure 4.20a, Figure 4.20b, and Figure 4.20c for Newtonian, power-law and Carreau models in a straight channel, respectively. As

clearly seen in the figures, whereas vortices are suppressed by pulsation for the power-law and Carreau fluids at t=9.25 and t=9.75, the same rule is not valid for a Newtonian fluid. Moreover, size of vortices exposed to non-Newtonian fluids is smaller than that of Newtonian fluid. That is, weaker vortices are created using non-Newtonian fluids. This can be explained by higher viscosity and lower electrical permittivity of the non-Newtonian fluids. As previously stated, suppression of the vortices also occurs for Newtonian fluid at potential difference of V=20V. Due to suppression of vortices, targeted mixing index values are not reached for non-Newtonian fluid in straight channel geometry.

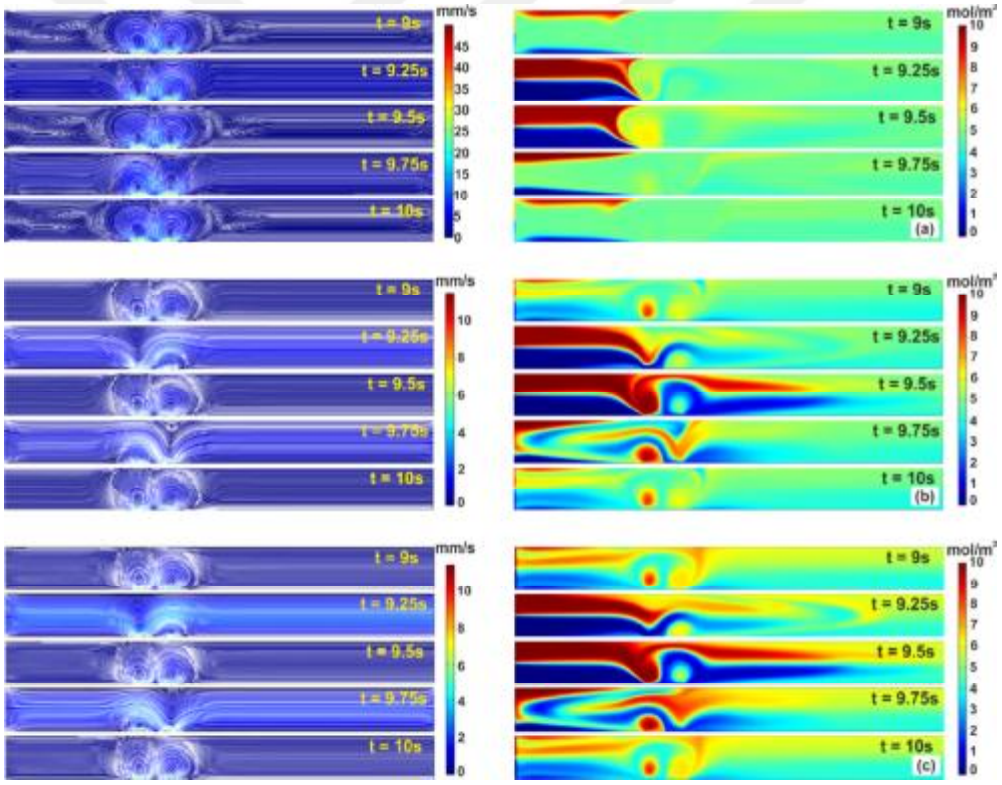

Figure 4.20. Velocity and concentration profiles for (a) Newtonian model (b) Power-law model and (c) Carreau model with zero obstruction

Mixing of the non-Newtonian fluids is investigated with microobstructions, subsequently. Obstruction widths are defined as W_c=0.01mm, 0.02mm and 0.03mm. Suppression of vortices is diminished when obstruction width is gradually increased. Velocity and concentration distributions at the highest obstruction width are illustrated in Figure 4.21a, Figure 4.21b and Figure 4.22c for Newtonian, power-law and Carreau models, respectively. With stronger and larger vortices, perturbations along flow streamlines are increased for non-Newtonian fluids and more uniform concentration profile is obtained at the outlet. Concentration profile for a Newtonian fluid is dropped below the average value due to the stronger vortices, which prevent transport of diluted species.

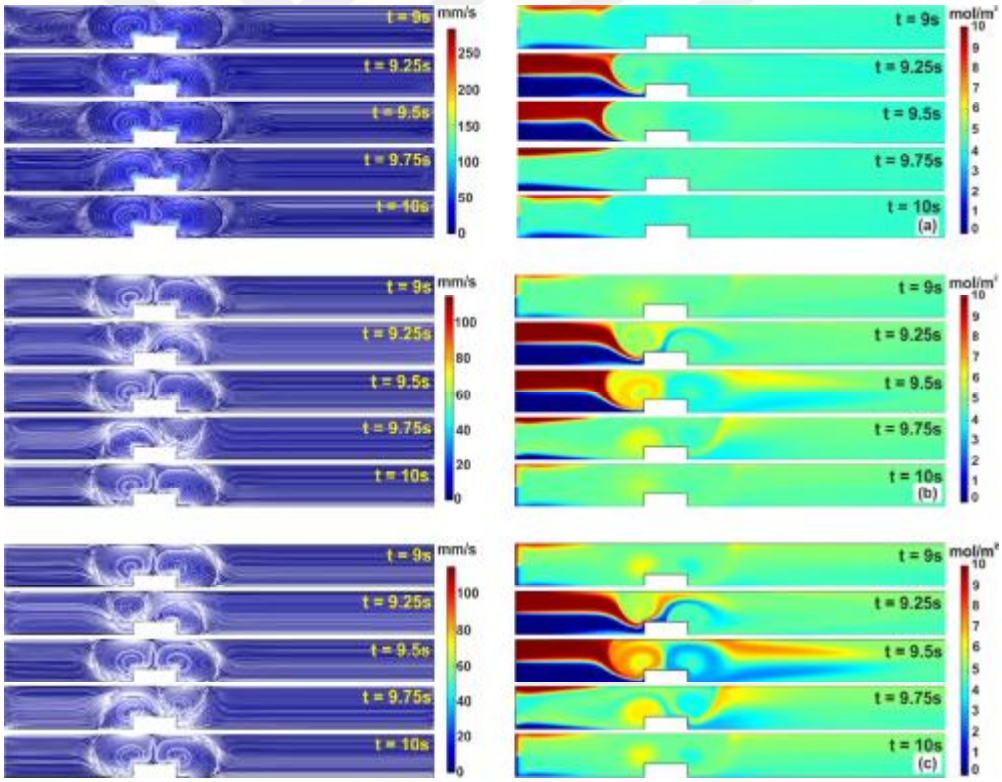

Figure 4.21. Velocity and concentration profiles for (a) Newtonian model (b) Power-law model and (c) Carreau model with the obstruction of 0.03mm

Mixing performances are demonstrated in Figure 4.22 by means of presenting mixing index values within the last period of pulsation under V=40V potential difference and f=1Hz frequency. These plots are created with twenty samples of timescale for increasing obstruction widths, such as Wc=(a) 0mm, (b) 0.01mm, (c) 0.02mm and (d) 0.03mm. Mixing index values are higher for Newtonian fluid as compared to non-Newtonian fluids for straight microchannel. While mixing index values are slightly increased with W_c=0.01mm increment, better performance is currently acquired from the Newtonian fluid. Lower viscosity value and higher permittivity result in higher mixing performance. In case of W_c=0.02mm, mixing index of a Newtonian fluid is decreased, even below the values of non-Newtonian fluid. This can be explained by transport amount of diluted species which is prevented by stronger vortices in Newtonian simulations. Mixing index values are further decreased with Newtonian fluid for the case of W_c=0.03mm. On the contrary, higher mixing indexes are achieved for non-Newtonian fluids starting from W_c=0.03mm. It can be concluded that mixing index can be increased with stronger vortices for lower obstructions, this trend is sustained with weaker vortices for higher obstructions.

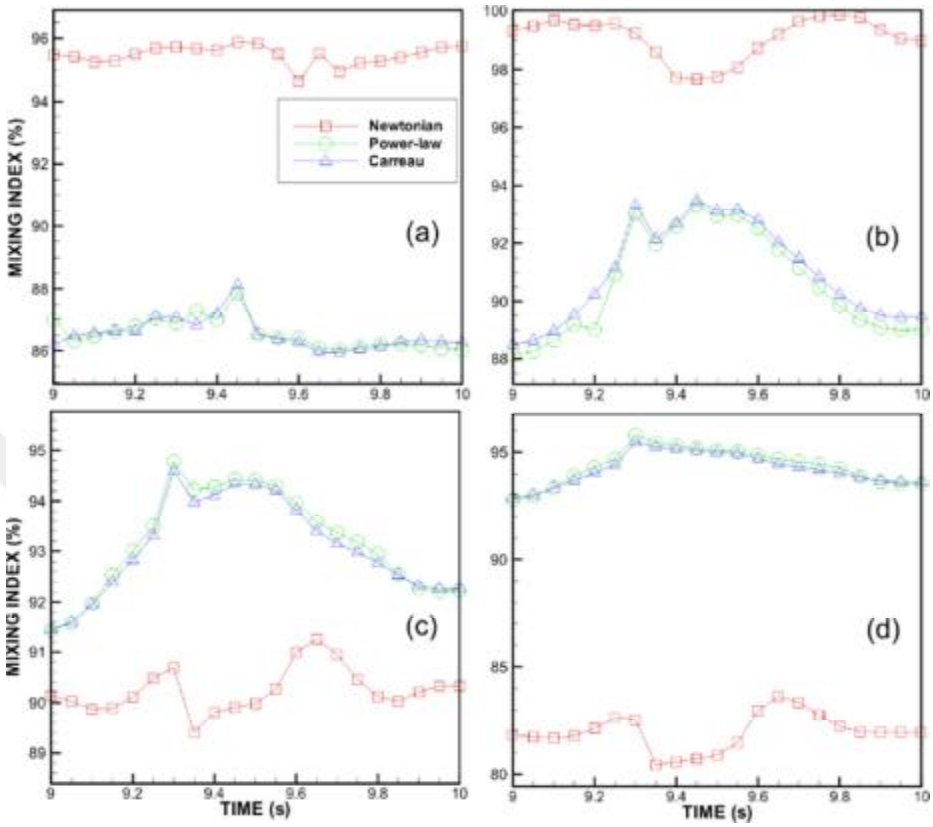

Figure 4.22. Mixing index values for (a) zero obstruction width (b) 0.01mm obstruction width (c) 0.02mm obstruction width (d) 0.03mm obstruction width

Effect of various external potential differences, such as V=(a) 20V, (b) 30V and (c) 40V, on mixing index values is presented in Figure 4.23, which is plotted for showing average mixing index during the last period of pulsation versus obstruction width for every fluid models. For V=20V, average mixing index value of Newtonian fluid is quite higher than non-Newtonian fluids. While this distinction is decreased with increasing obstruction widths, average mixing index of the Newtonian fluid is slightly exceeded by the non-Newtonian fluids for the highest obstruction width. For V=30V, average mixing index value of Newtonian fluid is again higher than that of non-Newtonian fluids. However, this distinction is

lower than the previous situation. Average mixing index value of non-Newtonian fluid is approached to the value of Newtonian fluid for W_c=0.01mm. Better average mixing performance is obtained from non-Newtonian fluids for W_c=0.02mm with decrease and increase in the average mixing indexes of Newtonian and non-Newtonian fluids, respectively. This trend is sustained in the following obstruction width of W_c=0.03mm. Thus, average mixing index values between the Newtonian and non-Newtonian fluids are increased. Similar increasing and decreasing pattern for average mixing index values are exhibited with the potential difference of V=40V. For the cases of W_c=0mm and Wc=0.01mm, average mixing index values are increased for each type of fluid in comparison with other potential differences. In addition, the increase in mixing index of non-Newtonian fluids is higher than that of Newtonian fluid. Therefore, average mixing values of non-Newtonian fluids are exceeded with higher distinction as compared to the 30V potential difference for the case W_c=0.02mm and W_c=0.03mm.

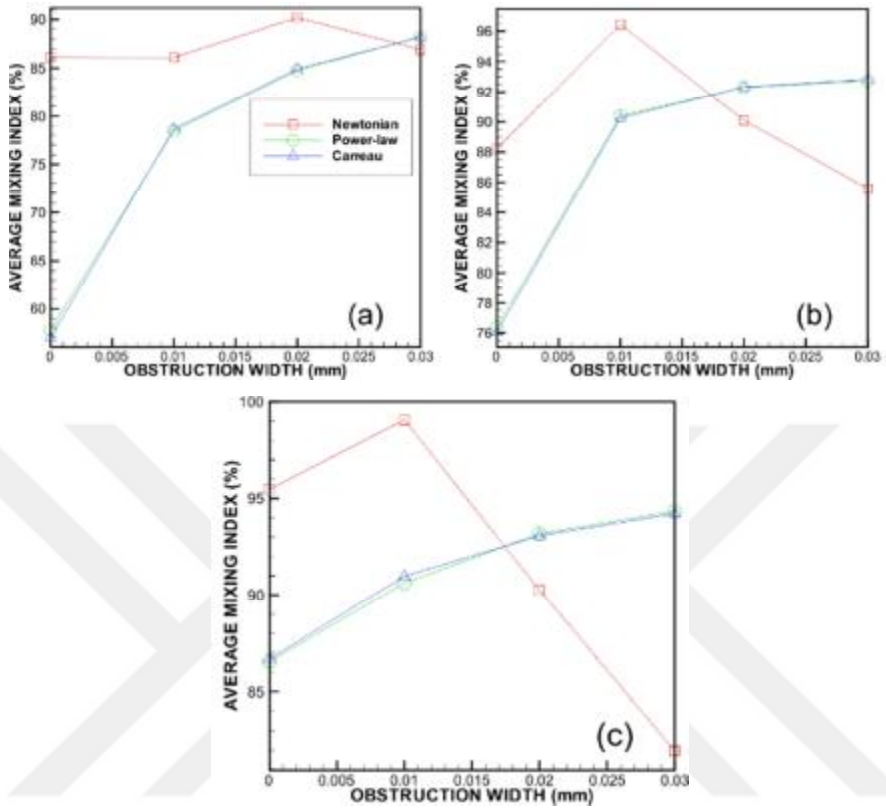

Figure 4.23. Average mixing index values of the last period of pulsation against obstruction width for the potential differences of (a) 20V (b) 30V (c) 40V

The frequency of pulsatile flow is a quite influential parameter on mixing index, which is represented by Strouhal number in the previous simulations for Newtonian fluid case. However, the velocity of the non-Newtonian fluid is altered continuously due to intrinsically varied viscosity value. Therefore, the frequency of pulsation is used directly for describing mixing behaviour in non-Newtonian cases. For enabling comparison in same graphic axis, results for the Newtonian fluid are also plotted using pulsation frequency. Frequency values of f=0.5Hz, 1Hz, 1.5Hz and 2Hz are employed for the simulations, likewise in Newtonian analyses, as shown in Figure 4.24. For straight microchannel, variations in mixing index typically exhibit a similar pattern for every fluid type. Mixing index is higher for a

Newtonian fluid and very close for non-Newtonian fluids in every pulsation frequency values. While the highest average mixing index is obtained for f=1Hz frequency, the lowest average mixing index is observed for f=2Hz. Mixing index is slightly and significantly decreased for f=1.5Hz and f=0.5Hz, respectively compared to f=1Hz. For W_c=0.01mm, variations in the average mixing index are maintained and increased approximately 7% for every fluid. Whereas this pattern is also valid for non-Newtonian fluids for the rest of the obstruction widths, better mixing performance is obtained with f=0.5Hz frequency for a Newtonian fluid. The decrease in the higher frequency values is contributed to less transport of diluted species which derives from lower flow duration for a single period. Average mixing index of the Newtonian fluid is exceeded by non-Newtonian fluids with f=1Hz frequency for the obstruction width of W_c=0.02mm. For W_c=0.03mm, average mixing index of a Newtonian fluid is exceeded by non-Newtonian fluids with both f=1Hz and f=1.5Hz frequency values. Moreover, the difference between these values is increased as compared to W_c=0.02mm obstruction width.

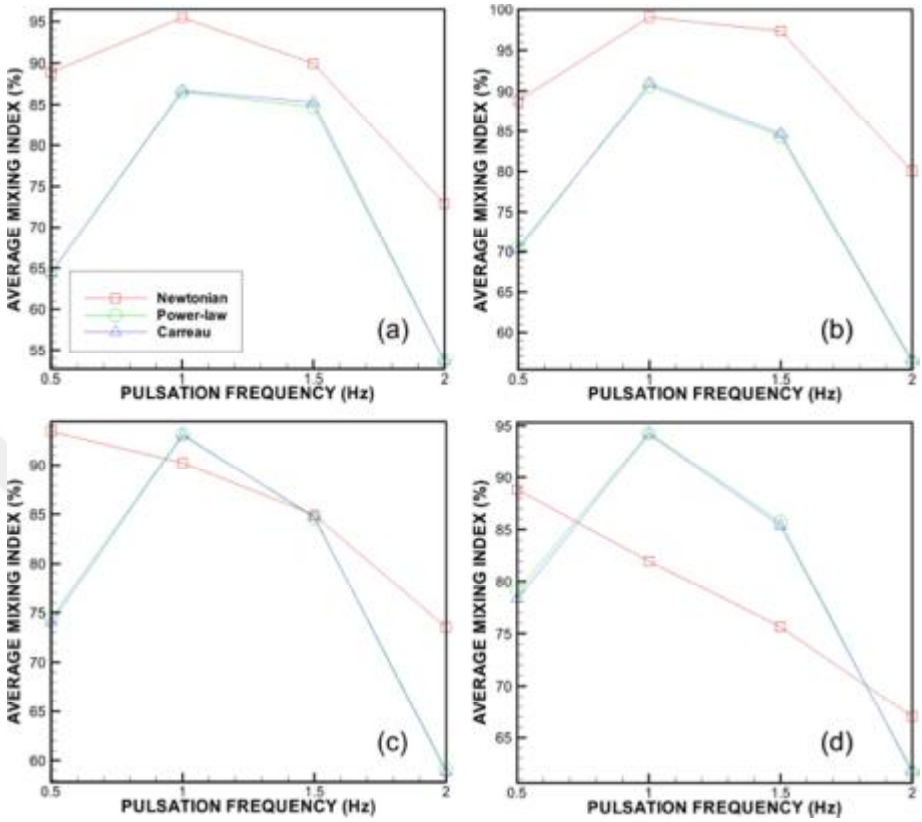

Figure 4.24. Average mixing index values of the last period of pulsation against pulsation frequency for (a) zero obstruction (b) 0.01mm obstruction (c) 0.02mm obstruction (d) 0.03mm obstruction

5. CONCLUSIONS

In this study, a micromixer design is investigated using numerical analysis. Both Newtonian and non-Newtonian fluids, namely water and blood, are driven by pulsation and electrokinetic effects and efficient mixing is achieved using coupling of pulsatile flow and ICEO phenomena. Mixing indexes are calculated according to the magnitude of electrical potential difference, height and length of the obstruction or i.e. ICEO electrode and the frequency of pulsatile flow. The conclusions are summarized below:

1- Since pulsatile flow has a positive effect on mixing efficiency, this advancement can be dramatically enhanced by presence of ICEO.
2- Mixing performance can be slightly increased by adding obstruction through the microchannel geometry. However, ICEO vortices can be strengthened, when floating electrode is placed on the top of rectangular obstruction.
3- Mixing index at the outlet of the microchannel is time-dependent due to pulsatile flow. However, mixing index values are more consistent with higher external potential differences.
4- More consistent mixing indexes are exhibited for longer obstructions (ICEO electrodes).
5- Mixing efficiency is proportional to magnitude of external potential differences. However, this tendency is broken by the presence of obstructions. Therefore, better mixing performances are observed for low external potential differences and wider obstructions.
6- Mixing performance is initially enhanced by an increase in the width of obstructions. However, further increase in its width, decreases the mixing efficiency.

7- Mixing indexes are increased until the value of f=1Hz pulsation frequency without obstruction in microchannel geometry. However, higher mixing performance is obtained for f=0.5 Hz with obstructed microchannel. Lower mixing performances are obtained for f=1.5Hz and 2Hz which can be attributed to low transport of diluted species.

8- Mixing performance value of 99% for Newtonian fluid can be obtained from the system with the specific parameters, which are L_c=0.1mm ICEO electrode length, W_c=0.01mm obstruction width, V=40V potential difference and f=1Hz pulsation frequency.

9- The performance of the current micromixer has slight variation for power-law and Carreau fluids.

10- Mixing index value is lower for non-Newtonian fluids compared to Newtonian fluid in the straight microchannel. However, mixing index for non-Newtonian fluids can be consistently enhanced with the presence of rectangular obstructions. This enhancement can reach higher values than Newtonian fluid for more substantial obstruction widths.

This study can be further enhanced by including chemical reactions between the diluted species. By means of modelling adsorption – desorption kinetics, antibody – antigen binding, protein – ligand reactions or any other bio-chemical analyses can be quantitively investigated.

REFERENCES

Abrams WR., Barber CA., McCann K., Tong G., Chen Z., Mauk MG., Wang J., Volkov A., Bourdelle P., Corstjens P.L.A.M., Zuiderwijk, M., Kardos, K., Li, S., Tanke H.J., Niebdala R.S., Malamud D., Bau, H., 2007. Development of a Microfluidic Device for Detection of Pathogens in Oral Samples Using Upconverting Phosphor Technology (UPT). Annals of the New York Academy of Sciences, 1098 (1): 375-388.

Afzal, A., Kim, K.Y., 2015a. Convergent-Divergent Micromixer Coupled with Pulsatile Flow. Sensors and Actuator B: Chemical, 211: 198-205.

Afzal, A., Kim, K.Y., 2015b. Optimization of Pulsatile Flow and g>Geometry of a Convergent–Divergent Micromixer. Chemical Engineering Journal, 281: 134-143.

Afzal, A., Kim, K.Y, 2014. Flow and Mixing Analysis of Non-Newtonian Fluids in Straight and Serpentine Microchannels. Chemical Engineering Science, 116: 263-274

Ajdari, A., 2000. Pumping Liquids Using Asymmetric Electrode Arrays. Physical Review E, 61 (1): R45-R48.

Alapati, S., Fernandez, D.V., Suh, Y.K., 2011. Enhancement of Mixing within a Micro Cavity by Use of Transient Induced-Charge Electro-osmotic Flow around Micro Electrodes. Journal of Mechanical Science and Technology, 25 (6): 1495-1499.

Ammar, H., el Moctar, A.O., Garnier, B., Peerhossaini, H., 2014. Flow Pulsation and Geometry Effects on Mixing of Two Miscible Fluids in Microchannels. Journal of Fluids Engineering, 136 (12): 121101(1-9).

Arulanandam, S., Li, D., 2000. Determining ζ Potential and Surface Conductance by Monitoring the Current in Electro-osmotic Flow. Journal of Colloid and Interface Science, 225 (2): 421-428.

Au, A.K, Lai, H., Utela, B.R., Folch, A., 2011. Microvalves and Micropumps for BioMEMS. Micromachines, 2 (2): 179-220.

Bazant, M.Z., Squires, T.M., 2004. Induced-Charge Electrokinetic Phenomena: Theory and Microfluidic Applications. Physical Review Letters, 92 (6): 066101(1-4).

Bazant, M.Z., Squires, T.M., 2010. Induced-Charge Electrokinetic Phenomena. Current Opinion in Colloid & Interface Science, 15 (3): 203-213.

Berselli, L.C., Miloro, P., Menciassi, A., Sinibaldi, E., 2013. Exact Solution to the Inverse Womersley Problem for Pulsatile Flows in Cylindrical Vessels, with Application to Magnetic Particle Targeting. Applied Mathematics and Computation, 219 (10): 5717-5729.

Bhattacharjee, N., Urrios, A., Kang, S., Folch, A., 2016. The upcoming 3D-printing revolution in microfluidics. Lab on a Chip, 16 (10): 1720-1742.

Bottauschi, F., Cardonne, C., Meinhart, C., Mézic, I., 2006. An Ultrashort Mixing Length Micromixer: The Shear Superposition Micromixer. Lab on a Chip, 7 (3): 396-398.

Canpolat, Ç., Qian, S., Beskok, A., 2013. Micro-PIV Measurements of Induced-Charge Electro-osmosis around a Metal Rod. Microfluidics and Nanofluidics, 14 (1-2): 153-162.

Canpolat, C., Zhang, M., Rosen, W., Qian, S., Beskok, A., 2013. Induced-Charge Electroosmosis around Touching Metal Rods. Journal of Fluids Engineering, 135 (2): 021103(1-10).

Castellarnau, M., Errachid, A., Madrid, C., Juarez, A., Samitier, J., 2006. Dielectrophoresis as a Tool to Characterize and Differentiate Isogenic Mutants of Escherichia Coli. Biophysical Journal, 91 (10): 3937-3945.

Chakraborty, S., 2007. Electroosmotically Driven Capillary Transport of Typical Non-Newtonian Biofluids in Rectangular Microchannels. Analytica Chimica Acta, 605 (2): 175-184.

Chang, C.C., Yang, R.J., 2004. Computational Analysis of Electrokinetically Driven Flow Mixing in Microchannels with Patterned Blocks, 14 (4): 550-558.

Chang, H., 2006. Electro-Kinetics: A Viable Micro-Fluidic Platform for Miniature Diagnostic Kits. The Canadian Journal of Chemical Engineering, 84 (2): 146-160.

Cheng, S.B., Skinner C.D., Taylor, J., Attiya, S., Lee, W.E., Picelli, G., Harrison, D.J., 2001. Development of a Multichannel Microfluidic Analysis System Employing Affinity Capillary Electrophoresis for Immunoassay. Analytical Chemistry, 73 (7): 1472-1479.

Cho, C.C., Chen, C.L., Chen, C.K., 2012. Flow Characteristics and Mixing Performance of Electrokinetically Driven Non-Newtonian Fluid in Contraction–Expansion Microchannel. Rheologica Acta, 51 (10): 925-935.

Chung, A.J., Kim, D., Erickson, D., 2008. Electrokinetic Microfluidic Devices for Rapid, Low Power Drug Delivery in Autonomous Microsystems. Lab on a Chip, 8 (2): 330-338.

Cortelezzi, L., Ferrari, S., Dubini, G., 2017. A Scalable Active Micro-mixer for Biomedical Applications. Microfluidics and Nanofluidics, 21: Article Number 31: 1-16.

Çengel, Y.A., Cimbala, J.M., 2006. Fluid Mechanics: Fundamentals and Applications. McGrew-Hill, New York, 959.

Das, M., Jain, V.K, Ghoshdastidar, P.S., 2008 Fluid flow Analysis of Magnetorheological Abrasive Flow Finishing (MRAFF) Process, International Journal of Machine Tools Manufacture, 48 (3-4): 415–426.

Das, S., Chakraborty, S., 2006. Analytical Solutions for Velocity, Temperature and Concentration Distribution in Electroosmotic Microchannel Flows of a Non-Newtonian Bio-fluid. Analytica Chimica Acta, 559 (1): 15-24.

Diercks AH., Ozinsky, A., Hansen, CL., Spotts, JM., Rodriguez, DJ., Aderam, A., 2009. A Microfluidic Device for Multiplexed Protein Detection in Nano-liter Volumes. Analytical Biochemistry, 386 (1): 30-35.

Egnor, M., Zheng, L., Rosiello, A., Gutman, F., Davis, R., 2002. A Model of Pulsations in Communicating Hydrocephalus. Pediatric Neurosurgery, 36 (6): 281-303.

Fallenius B.E.G., Sattari A., Fransson J.H.M, Sandberg M., 2013. Experimental study on the effect of pulsating inflow to an enclosure for improved mixing. International Journal of Heat and Fluid Flow, 44: 108-119.

Fan, L., Zhu, X., Zhao, H., Zhe, J., Zhao, L., 2017. Rapid microfluidic mixer utilizing sharp corner structures. Microfluidics and Nanofluidics, 21 (36): 1-12.

Feng, H., Wong, T.N., Che, Z., Marcos. Chaotic Micromixer Utilizing Electro-osmosis and Induced Charge Electro-osmosis in Eccentric Annulus. Physics of Fluids, 28: 062003-(1-19).

Fowler, J., Moon, H., Kim, C., 2002. Enhancement of Mixing by Droplet-Based Microfluidics. Micro Electro Mechanical Systems, 97-100.

Frénéa, M., Faure, S.P., Le Pioufle, B., Coquet, P., Fujita, H., 2003. Positioning living cells on a high-density electrode array by negative dielectrophoresis. Materials Science and Engineering: C, 23 (5): 597-603.

Frommelt, T., Kostur, M., Wenzel-Schafer, M., Talkner, P., Hanggi, P., Wixforth, A., 2008. Microfluidic Mixing via Acoustically Driven Chaotic Advection, 100 (3): 034502(1-4).

Fung, YS., 2016. Microfluidic Chip-Capillary Electrophoresis Devices. CRC Press, Hong Kong, 396.

Galletti, C., Roudgar, M., Brunazzi, E., Mauri, R., 2012. Effect of Inlet Conditions on the Engulfment Pattern in T-shaped Micro-mixer. Chemical Engineering Journal, 185-186: 300-313.

Gao, Y., Tran, P., Petkovic-Duran K., Swallow, T., Zhu, Y., 2015. Acoustic Micromixing Increases Antibody-Antigen Binding in Immunoassays. Biomedical Microdevices, 17: 79.

Garcia A., Ista L.K., Petsev D.N., O'Brien M.J., Bisong P., Mammoli A.A., Brueck S.R.J., Lopez, G. P., 2008. Electrokinetic Molecular Separation in Nanoscale Fluidic Channels. Lab on a Chip, 5 (11): 1271-1276.

Gascoynea, P. Pethig, R. Satayavivadc, J., Beckera, F.F, Ruchirawatc, M., 1997. Dielectrophoretic Detection of Changes in Erythrocyte Membranes Following Malarial Infection. Biochimica et Biophysica Acta (BBA) – Biomembranes, 1323 (2): 240-252.

Glasgow, I., Aubry, N., 2003. Enhancement of Microfluidic Mixing Using Time Pulsing. Lab on a Chip, 3 (2): 114-120.

Glasgow, I., Lieber, S., Aubry, N., 2004. Parameters Influencing Pulsed Flow Mixing in Microchannels. Analytical Chemistry, 76 (16): 4825-4832.

Godin J., Lien V., Lo YH., 2008. Microfluidics and Photonics for Bio-System-on-a-Chip: A Review of Advancements in Technology towards a Microfluidic Flow Cytometry Chip. Journal of Biophotonics, 1 (5): 355-376.

Goullet, A., Glasgow, I., Aubry, N., 2006. Effects of Microchannel Geometry on Pulsed Flow Mixing. Mechanics Research Communications, 33 (5): 739-746.

Goswami, P., Mondal, P.K., Dutta, S., Chakraborty, S., 2015. Electroosmosis of Powell–Eyring Fluids under Interfacial Slip. Electrophoresis, 36 (5): 703-711.

Hadigol, M., Nosrati, R., Nourbakhsh, A., Raisee, M., 2011. Numerical Study of Electroosmotic Micromixing of Non-Newtonian fluids. Journal of Non-Newtonian Fluid Mechanics, 166 (17-18): 965-971.

Halpern, D., Wei, H., 2007. Electroosmotic Flow in a Microcavity with Nonuniform Surface Charges. Langmuir, 23 (18): 9505-9512.

Han, Y., Wan, J.J., Gu, X.P., Feng, L.F., 2012. Numerical Simulation on Micromixing of Viscous Fluids in a Stirred-Tank Reactor. Chemical Engineering Science, 74: 9-17.

Harnett, C.K., Templeton, J., Dunphy-Guzman, K.A., Senousy, Y.M., Kanouff, M.P., 2008. Model Based Design of a Microfluidic Mixer Driven by Induced Charge Electroosmosis. Lab on a Chip, 8 (4): 565-572.

Hessel, V., Löwe, H., Schönfeld, F. 2005. Micromixers – A Review on Passive and Active Mixing Principles. Chemical Engineering Science, 60 (8-9): 2479-2501.

Horner, M., Metcalfe, G., Wiggins, S., Ottino, J.M., 2002. Transport enhancement mechanisms in open cavities. Journal of Fluid Mechanics, 452: 199-229.

Hunter, R.J., 1981. Zeta Potential in Colloid Science: Principles and Applications. Academic Press Inc., New York, 386.

Jain, M., Yeung, A., Nandakumar, K., 2009a. Efficient Micromixing Using Induced-Charge Electroosmosis. Journal of Microelectromechanical Systems, 18 (2): 376-384.

Jain, M., Yeung, A., Nandakumar, K., 2009b. Induced-Charge Electroosmotic Mixer: Obstacle Shape Optimization. Biomicrofluidics, 3 (2): 022413(1-15).

Jensen, KF., 2001. Microreaction Engineering – Is Small Better. Chemical Engineering Science, 56 (2): 293-303.

Jeong, G.S., Chung, S., Kim, C.B., Lee, S.H., 2009. Applications of Micromixing Technology. Analyst, 135 (3): 460-473.

Jones, T.B., 2003. Basic Theory of Dielectrophoresis and Electrorotation. IEEE Engineering in Medicine and Biology Magazine, 22(6): 33-42

Kamali, R., Manshadi, M.K.D., Mansoorifar A., 2016. Numerical Analysis of Non-Newtonian Fluid Flow in a Low Voltage Cascade Electroosmotic Micropump. Microsystem Technologies, 22 (12): 2901-2907.

Karami, M., Jarrahi, M., Shirani, E., Peerhossaini, H., 2014. Mixing Enhancement in a Chaotic Micromixer Using Pulsatile Flow. ASME Proceedings, FEDSM2014-21360: 1-9.

Kazemi, S., Nourian, V., Nobari, M.R.H., Movahed, S., 2017. Two Dimensional Numerical Study on Mixing Enhancement in Micro-channel due to Induced Charge Electrophoresis. Chemical Engineering & Processing: Process Intensification, 120: 241-250.

Kim, S., Wang, F., Burns, M.A., Kurabayashi, K., 2009. Temperature-Programmed Natural Convection for Micromixing and Biochemical Reaction in a Single Microfluidic Chamber. Analytical Chemistry, 81 (11): 4510-4516.

Kim, S.J., Yokokawa, R., Lesher-Perez, S.C., Takayama, S., 2015. Multiple Independent Autonomous Hydraulic Oscillators Driven by a Common Gravity Head. Nature Communications, Article Number: 7301

Kopp, M.U., Crabtree H.J., Manz, A., 1997. Developments in Technology and Applications of Microsystems. Current Opinion in Chemical Biology, 1 (3): 410-419.

Kunti, G., Bhattacharya, A., Chakraborty, S., 2017. Analysis of Micromixing of Non-Newtonian Fluids Driven by Alternating Current Electrothermal Flow. Journal of Non-Newtonian Fluid Mechanics, 247: 123-131.

Krishnan, R., Sullivan, B.D., Mifflin, R.L, Esener, S.C., Professor, M.J.H., 2008. Alternating Current Electrokinetic Separation and Detection of DNA Nanoparticles in High-Conductance Solutions. Electrophoresis, 29 (9): 1765-1774.

Krüger, J. Singh, K., O'Neill, A., Jackson, C., Morrison, A., O'Brien, P., 2002. Development of a Microfluidic Device for Fluorescence Activated Cell Sorting. Journal of Micromechanics and Microengineering, 12: 486-494.

Lee, C., Wang, W., Liu, C., Fu, L., 2016. Passive Mixers in Microfluidic Systems: A Review. Chemical Engineering Journal, 288: 146-160.

Lee, C.Y., Chang, C.L., Wang, Y.N., Fu, L.W., 2011. Microfluidic Mixing: A Review. International Journal of Molecular Science, 12(5): 3263-3287.

Levitan, J.A., Devasenathipathy, S., Studer, V., Ben, Y., Thorsen, T., Squires, T.M., Bazant, M.Z., (2005). Experimental Observation of Induced-Charge Electro-osmosis around a Metal Wire in a Microchannel. Colloids and Surfaces A: Physicochemical and Engineering Aspects 267 (1-3): 122–132.

Li D., 2004. Electrokinetic in Microfluidics, Volume 2. Elsevier Academic Press, London, 643.

Li, G., Ge, S., Ni, X., Wang, Q., He, P., Fang, Y., 2010. Multiplexed p53 Mutation Detection by Microchip Electrophoresis with Laser-Induced Fluorescence Detector. Chinese Journal of Chemistry, 28 (5): 797-208.

Li, Z, Kim S, 2017. Pulsatile micromixing using water-head-driven microfluidic oscillators. Chemical Engineering Journal, 313: 1364-1369.

Li, Z., Kim, S.J., 2016. Pulsatile Micromixing Using Water-Head-Driven Microfluidic Oscillators. Chemical Engineering Journal, 313: 1364-1469.

Lim, YC., Kouzani, AZ., Duan, W., 2010, Lab-on-a-Chip: A Component View. Microsystem Technologies, 16 (12): 1995-2015.

Malek, CGK, 2016a. Laser Processing for Bio-microfluidics Applications (Part I). Analytical and Bioanalytical Chemistry 385 (8): 1351-1361.

Malek, CGK, 2016b. Laser Processing for Bio-microfluidics Applications (Part II). Analytical and Bioanalytical Chemistry 385 (8): 1362-1369.

Manz A., Graber N., Widmer HM., 1990. Miniaturized Total Chemical Analysis Systems: A Novel Concept for Chemical Sensing. Sensors and Actuator B: Chemical, 1 (1-6): 244-248.

Mao, W.B., Xu J.L., 2009. Micromixing enhanced by pulsating flows. International Journal of Heat and Mass Transfer, 52 (21-22): 5258-5261.

Mark, D., Haeberle, S., Roth G., von Stetten, F., Zengerle, R., 2010. Microfluidic Lab-on-a-Chip Platforms: Requirements, Characteristics and Applications. Chemical Society Reviews. 39: 1153-1182.

Martinez, AW., Phillips, ST., Whitesides, GM., Carrilho, E., 2012. Diagnostics for the Developing World: Microfluidic Paper-Based Analytical Devices. Analytical Chemistry, 82 (1), 3-10.

Masliyah, J.H., Bhattacharjee S., 2006. Electrokinetic and Colloid Transport Phenomena, Wiley Interscience Publication, New York, 707.

Morgan, H., Green, N.G., 2002. AC Electrokinetics: Colloids and Nanoparticles. Research Studies Press Ltd, Hertfordshire, 324.

Nauman, E.A., Risic, K.J., Keaveny, T.M., Satcher, R.L., 1999. Quantitative Assessment of Steady and Pulsatile Flow Fields in a Parallel Plate Flow Chamber. Annals of Biomedical Engineering, 27 (2): 194-199.

Nejat, A., Kowsary F., Hasanzadeh-Barforoushi A., Ebrahimi S., 2014. Unsteady Pulsating Characteristics of the Fluid Flow through a Sudden Expansion Microvalve. Microfluidics and Nanofluidics, 17 (4): 623-627.

Nguyen, N.T., Wu, Z., 2005. Micromixers – A Review. Journal of Micromechanics and Microengineering, 15: R1-R16.

Özdinç Çarpınlıoğlu, M., Gündoğdu, M.Y., 2001. A Critical Review on Pulsatile Pipe Flow Studies Directing towards Future Research Topics. Flow Measurement and Instrumentation, 12 (3): 163-174.

Pethig, R., Menachery, A., Pells, S., De Sousa, P., 2010. Dielectrophoresis: A Review of Applications for Stem Cell Research. Journal of Biomedicine and Biotechnology, 2010: 1-7.

Pommer, M.S., Zhang, Y., Keerthi, N., Chen, D., Thomson, J.A., Meinhart, C.D., Professor, H.T.S., 2008. Dielectrophoretic Separation of Platelets from Diluted Whole Blood in Microfluidic Channels. Electrophoresis, 29 (6): 1213-1218.

Probstein, R.F., 1994. Physicochemical Hydrodynamics: An Introduction, 2nd Edition, Wiley Interscience Publication, New York, 416.

Psaltis, D, Quake, SR, Yang, C., 2006. Developing Optofluidic Technology through the Fusion of Microfluidics and Optics. Nature: International Journal of Science, 442: 381-386.

Qian, S., Ai, Y., 2012. Electrokinetic Particle Transport in Micro-/Nanofluidics: Direct Numerical Simulation Analysis. CRC Press, USA, 365.

Qian, S., Wang, A., Afonien, J.K., 2006. Electrophoretic Motion of a Spherical Particle in a Converging-Diverging Nanotube. Journal of Colloid and Interface Science, 303 (2): 579-592.

Ramos, A., Morgan, H., Green, N.G., Castellanos, A., 1999. AC Electric-Field-Induced Fluid Flow in Microelectrodes. Journal of Colloid and Interface Science, 217: 420-422.

Rao, R.A., Devanathan, R., 1973. Pulsatile Flow in Tubes of Varying Cross-Sections. Journal of Applied Mathematics and Physics (ZAMP), 24 (2): 203-213.

Ren, Y., Liu, W., Jia, Y., Tao, Y., Shao, J., Ding, Y., Jiang, H., 2013. Induced-Charge Electroosmotic Trapping of Particles. Lab on a Chip, 15 (10): 2181-2191.

Rios, A., Zougagh M., Avila M., 2012. Miniaturization Through Lab-on-a-Chip: Utopia or Reality for Routine Laboratories?: A Review. Analytica Chimica Acta, 740: 1-11.

Rubenstein, D.A., Yin, W., Frame, M.D., 2012. Biofluid Mechanics: An Introduction to Fluid Mechanics, Macrocirculation, and Microcirculation. Academic Press, Waltham, 400.

Sadeghi A., Veisi, H., Saidi, M.H., Mozafari, A.A., 2013. Electroosmotic Flow of Viscoelastic Fluids Through a Slit Microchannel With a Step Change in Wall Temperature. Journal of Heat Transfer, 135 (2): 021706 (1-12).

Sahu, P.J., Golia, A., Sen, A.K., 2013. Investigations into Mixing of Fluids in Microchannels with Lateral Obstructions. Microsystem Technologies. 19 (4): 493-501.

Shamloo, A., Madedelahi, M., Akbari, A., 2016. Numerical Simulation of Centrifugal Serpentine Micromixers and Analyzing Mixing Quality Parameters. Chemical Engineering and Processing: Process Intensification, 104: 243-252.

Shamloo, A., Mirzakhanloo, M., Dabirzadeh, M.R., 2016. Numerical Simulation for Efficient Mixing of Newtonian and Non-Newtonian Fluids in an Electro-osmotic Micro-mixer. Chemical Engineering and Processing: Process Intensification, 107: 11-20.

Shamsoddini, R., Sefid, M., Fatehi, R., 2016. Incompressible SPH Modeling and Analysis of Non-Newtonian Power-law Fluids, Mixing in a Microchannel with an Oscillating Stirrer. Journal of Mechanical Science and Technology, 30 (1): 307-316.

Sharp, K.V., Yazdi, S.H., Davison, S.M., 2011. Localized Flow Control in Microchannels Using Induced-Charge Electroosmosis Near Conductive Obstacles. Microfluidics and Nanofluidics, 10 (6): 1257-1267.

Shimizu, K., Araki, H., Sakata, K., Tonomura W., Hashida, M., Konishi, S., 2015. Microfluidic Devices for Construction of Contractile Skeletal Muscle Microtissues. Journal of Bioscience and Bioengineering, 119 (2): 212-216.

Shin S.M., Kang I.S., Cho Y.K, 2005. Mixing Enhancement by Using Electrokinetic Instability under Time-periodic Electric Field. Journal of Micromechanics and Microengineering, 15 (3): 455-462.

Shiose, A., Nowak, K., Horvath, D.J., Massiello, A.L., Golding, L.A.R., Fukamachi, K., 2010. Speed Modulation of the Continuous-Flow Total Artificial Heart to Simulate a Physiologic Arterial Pressure Waveform. ASAIO Journal, 56 (5): 403-409.

Shyam, S., Datta, A., Das, A.K., 2018. Numerical Analysis of Fluid Flow and Heat Transfer of Flow Between Parallel Plates Having Rectangular Shape Micromixer. Journal of Thermal Science and Engineering Applications, 10: 011003(1-8).

Squires, T.M., Bazant, M.Z., 2004. Induced-Charge Electro-osmosis. Journal of Fluid Mechanics, 509: 217-252.

Squires, T.M., Bazant, M.Z., 2006. Breaking Symmetries in Induced-Charge Electro-osmosis and Electrophoresis, 560: 65-101.

Srivastava S.K., Gençoğlu, A., Minerick, A.R., 2010. DC Insulator Dielectrophoretic Applications in Microdevice Technology: A Review. Analytical and Bioanalytical Chemistry, 399 (1): 301-321.

Stone, HA, Stroock AD, Ajdari A., 2004. Engineering Flows in Small Devices: Microfluidics Toward a Lab-on-a-Chip. Annual Review of Fluid Mechanics, 36: 381-411.

Suehiro, J., Sano, N., Zhou, G., Imakiire, H., Imasaka, K., Hara, M., 2005. Application of Dielectrophoresis to Fabrication of Carbon Nanohorn Gas Sensor. Journal of Electrostatics, 64 (8): 408-415.

Suh, Y.K., Kang S., 2010. A Review on Mixing in Microfluidics. Micromachines, 1 (3): 82-111.

Sze, A., Erickson, D., Ren, L., Li, D., 2003. Zeta-Potential Measurement Using the Smoluchowski Equation and the Slope of the Current–Time Relationship in Electroosmotic Flow. Journal of Colloid and Interfacial Science, 261 (2): 402-410.

Tang, G.H., Li, X.F., He, Y.L., Tao, W.Q., 2009. Electroosmotic Flow of Non-Newtonian Fuid in Microchannels. Journal of Non-Newtonian Fluid Mechanics, 157(1-2): 133-137.

Tanthapanichakoon, W., Aoki, N., Matsuyama, K., Mae, K., 2006. Design of Mixing in Microfluidic Liquid Slugs Based On a New Dimensionless Number for Precise Reaction and Mixing Operations. Chemical Engineering Science, 61 (13): 4220-4232.

Tikekar, M., Singh, S.G., Agrawal, A., 2010. Measurement and Modeling of Pulsatile Flow in Microchannel. Microfluidics and Nanofluidics, 9 (6): 1225-1240.

Toner, M. Irimia, D., 2005. Blood-on-a-Chip. Annual Review of Biomedical Engineering, 7: 77-103.

Trietsch SJ., Hankemeier T., van der Linden HJ., 2011. Lab-on-a-Chip Technologies for Massive Parallel Data Generation in the Life Sciences: A Review. Chemometrics and Intelligent Laboratory Systems, 108 (1): 64-75.

Valencia, P.M., Basto, P.A., Zhang, L., Rhee, M., Langer, R., Farokhzad, O.C., Karnik, R., 2010. Single-Step Assembly of Homogenous Lipid-Polymeric and Lipid-Quantum Dot Nanoparticles Enabled by Microfluidic Rapid Mixing. ACS Nano, 4 (3): 1671-1679.

Van De Pol, F.C.M., 1989. A Pump Based on Micro-Engineering Techniques. Enschede, 208.

Velev, O.D., Gangwal, S., Petsev, D.N., 2009. Particle Localized AC and DC Manipulation and Electrokinetic. Annual Reports Section "C" (Physical Chemistry), 105: 213-246.

Wainright, A., Nguyen, U., Bjornson, T., Boone, T., 2003. Preconcentration and Separation of Double-Stranded DNA Fragments by Electrophoresis in Plastic Microfluidic Devices, 24 (21): 3784-3792.

Wang P., Chen Z., Chang C., 2006. A New Electroosmotic Pump Based On Silica Monoliths. Sensors and Actuator B: Chemical, 113 (1): 500-509.

Wang, B., Xu, J.L., Zhang, W., Li, Y.X., 2011. A New Bubble-Driven Pulse Pressure Actuator for Micromixing Enhancement. Sensors and Actuators A: Physical, 169 (1): 194-205.

Wang, D., Summers, J.L., Gaskell, P.H., 2008. Modelling of Electrokinetically Driven Mixing Flow in Microchannels with Patterned Blocks. Computers & Mathematics with Applications, 55 (7): 1601-1610.

Wu J., Ben Y., Battigelli D., Chang H., 2005. Long-Range AC Electroosmotic Trapping and Detection of Bioparticles. Industrial & Engineering Chemistry Research, 44 (8): 2815-2822.

Wu, D., Qin, J., Lin B., 2007. Electrophoretic separations on microfluidic chips. Journal of Chromatography A, 1184 (1-2): 542-559.

Wu, Y., Ren, Y., Tao, Y., Hou, L., Hu, Q., Jiang, H., 2017. A Novel Micromixer Based On the Alternating Current-Flow Field Effect Transistor. Lab on a Chip, 17 (1): 186-197.

Wu, Z., Li, D., 2007. Mixing and Flow Regulating by Induced-Charge Electrokinetic Flow in a Microchannel with a pair of Conducting Triangle Hurdles. Microfluidics and Nanofluidics, 5 (1): 65-76.

Wu, Z., Li, D., 2008. Micromixing Using Induced-Charge Electrokinetic Flow. Electrochimica Acta, 53 (19): 5827-5835.

Xia, Q., Zhong, S., 2013. Liquid Mixing Enhanced by Pulse Width Modulation in a Y-Shaped Jet Configuration. Fluid Dynamics Research 45 (2): 025504 (20pp)

Xue, Q., Wainright, A., Gangakhedkar, S., Gibbons, I., 2001. Multiplexed Enzyme Assays in Capillary Electrophoretic Single Use Microfluidic Devices. Electrophoresis, 22 (18): 4000-4007.

Yamamoto, M., Yasukawa T., Suzuki, M., Kosuge, S., Shiku, H., Matsue, T., Mizutani, F., 2012. Patterning with Particles using Three-Dimensional Interdigitated Array Electrodes with Negative Dielectrophoresis and Its Application to Simple Immunosensing. Electrochimica Acta, 82: 35-42.

Yang, J.T., Huang, K.J., Lin, Y.C., 2005. Geometric Effects on Fluid mixing in Passive Grooved Micromixers. Lab on a Chip, 5 (10): 1140-1147.

Yılmaz, F., Gündoğdu M.Y., 2008. A Critical Review on Blood Flow in Large Arteries; Relevance to Blood Rheology, Viscosity Models, and Physiologic Conditions. Korea-Australia Rheology Journal, 20 (4): 197-211.

Zhang, C., Khoshmanesh, K., Mitchell, A., Kalantar-zadeh, K., 2010. Dielectrophoresis for manipulation of micro/nano particles in microfluidic systems. Analytical and Bioanalytical Chemistry, 396 (1): 401-420.

Zhang, K., Mi, X.J., Yu, M.Z., 2012. Design of Super-Efficient Mixer Based On Induced Charge Electroosmotic. Thermal Science, 16(5):1534-1538.

Zhao, C., Zholkovskij, E., Masliyah, J.H., Yang, C., 2008. Analysis of electroosmotic flow of power-law fluids in a slit microchannel. Journal of Colloid and Interface Science, 326: 503-510.

Zhou D., Deng C., Cang L., 2004. Electrokinetic Remediation of a Cu Contaminated Red Soil by Conditioning Catholyte pH with Different Enhancing Chemical Reagents. Chemosphere, 56 (3): 265-273.

Zimmerman, W.B., Rees, J.M., Craven, T.J., 2006. Rheometry of Non-Newtonian Electrokinetic Flow in a Microchannel T-Junction. Microfluidics Nanofluidics 2 (6): 481–492.

CURRICULUM VITAE

Mehmet Melih TATLISOZ was born in Kayseri on October 27th, 1992. He received elementary and secondary education at TED Kayseri College. Afterwards, he maintained his education in Sema Yazar Anatolian High School, Kayseri. He completed his undergraduate study in Erciyes University, Department of Biomedical Engineering and graduated in 2015. He settled to Master of Science (MSc) program in the same department upon his graduation. In December 2015, he started to work as a research assistant in Çukurova University, Biomedical Engineering Department and made lateral transfer for MSc studentship. He is currently working in this department under same title.